Realizing Efficient Electroluminescence from Silicon Nanocrystals

A DISSERTATION
SUBMITTED TO THE FACULTY OF THE GRADUATE SCHOOL
OF THE UNIVERSITY OF MINNESOTA
BY

Kai-Yuan Cheng

IN PARTIAL FULFILLMENT OF THE REQUIREMENTS
FOR THE DEGREE OF
DOCTOR OF PHILOSOPHY

Russell J. Holmes, Advisor

November 2013

Acknowledgements

The journey of graduate research at University of Minnesota has truly been an exceptional and unforgettable experience in my life. Endless efforts and sleepless nights spent in the dark room searching for light (from light-emitting devices) for the future have made this journey a rewarding research and learning experience. This dissertation is the result of not only mine but many other people's efforts and could not have been completed without their generous support. Among all the people who have helped me during the past few years, the person who deserves the most of my gratitude is my advisor Prof. Russell J. Holmes. In 2006, he granted me the opportunity to join his research group. Since then, he has sacrificed countless hours and evenings for educating me. All the training and challenges from him gave me the chance to learn how to become a better researcher with critical thinking. The everyday discussions with him always inspired my innovation to attack problems from different angles. His selfless devotion and kind patience in guiding me made this dissertation possible. With his great knowledge in optoelectronics and dedication in teaching, he sets a model of a great advisor.

I would also like to thank Prof. Uwe Kortshagen, Dr. Rebecca J. Anthony, and Ting Chen, who provided great support in synthesizing silicon nanocrystal active materials and giving helpful suggestions in my research. This collaboration has helped me develop better communication skills and in-depth technical knowledge on silicon nanocrystals. In addition, immense acknowledgements are necessary for Prof. C. Daniel Frisbie. With his kind permission, I had the access to get trained and use the facilities in his laboratory. His

Dedication

This dissertation is dedicated to my parents, H.-M. Cheng and S.-C. Wu, for their endless love of supporting me, believing in me, and teaching me the spirit of perseverance and being modest.

Abstract

Colloidal semiconductor nanocrystals (NCs) have received considerable attention for optoelectronic applications due to their high photoluminescence efficiency and broad spectral tunability. The solution processibility of semiconductor NCs permits the integration into hybrid light-emitting devices that use organic semiconductors as charge transport layers. These devices offer the potential for low-cost manufacture through wet-coating processes in the future. While electroluminescence (EL) from group II-VI and III-V NCs has been well studied, emission from group IV NCs including silicon (Si) has not been characterized as extensively.

This work focuses on solving the challenges to realizing efficient EL from hybrid nanocrystal-organic light-emitting devices (NC-OLEDs) containing organic semiconductors and SiNCs that are chemically passivated with ligands. Starting from the macroscopic point of view, this work first aims to understand the relationship between the surface morphology of SiNCs and device performance using a traditional hybrid nanocrystal-organic device design. The inherent bottlenecks of these conventional devices are discussed as they relate specifically to EL from SiNCs. Consequently, new device architecture is proposed, separately optimizing each functional layer within the hybrid device structure, concluding with the establishment of design rules for device engineering. Furthermore, efforts are made to address the significant open question of how surface passivation impacts device performance. Such discussion provides another consideration at NC surface during the hybrid-device design. Finally, an overview for the future research direction will be discussed.

Table of Contents

List of Tables

List of Figures

Chapter 1 Introduction to Light-Emitting Devices and Organic Semiconductors

1.1 Introduction to Light-Emitting Devices

1.1.1 Foreword

With the rapid growth in world population and hence energy demand, achieving high efficiency energy usage in lighting has stood up as one of the most important strategies for energy saving and has been intensively investigated over the past few decades. As is known, in traditional lighting such as incandescent light bulbs or compact fluorescent light bulbs, only around 10% of the electrical energy is converted into light whereas almost 90% of the energy is simply wasted in the form of re-adsorption by the lamp or dissipation as heat.[1-3] The resulting energy loss is therefore tremendous, especially with the continuous expansion of lighting to more and more application aspects, including indoor/outdoor lighting, displays, mobile electronics, etc. Such enormous energy loss from lighting applications can raise serious environmental issues such as greenhouse gas emissions, worsen the current energy shortage by accelerating resource depletion, and thus could impose a significant impact on the world economy. Therefore, additional research is essential in order to fully overcome the energy inefficiency in both lighting and information display systems.

Recently, inorganic and organic solid-state light-emitting devices have emerged as one of the potential approaches to reducing the energy waste. As a junction built with p- and n-type materials, holes and electrons can travel through the corresponding type of

semiconductor with recombination at the junction interface, leading to light emission by electroluminescence (EL).

1.1.2 Background

Since the first observation of EL from a silicon carbide LED by Round et al. in 1907[4, 5], there has been substantial and ground-breaking development in inorganic LEDs. To date, the technology of inorganic LEDs has already explored emission wavelengths from ultra-violet to infrared.[5-7]

In addition to the "hard" semiconductor materials (inorganic), "soft" semiconductor materials (organic) have also received significant attention. Organic semiconductors are often highly conjugated. The highly delocalized electrons within the molecules greatly improve the optical and electronic properties for device fabrication. Since organic semiconductors are bound by weak intermolecular van der Waals interactions, these materials are often mechanically compliant for high throughput manufacture. Also, the excellent solubility of these materials in organic solvents provides the possibility for low-cost device fabrication by solution processing. As such, LEDs made with organic materials could potentially be used as large-area applications.

The first breakthough of organic light-emitting devices (OLEDs) was demonstrated by Tang et al.[8] Since then, research has been carried out for achieving better device performance.[9, 10] Recently, a new type of OLED has received significant attention with semiconductor NCs as the embedded active materials. Semiconductor-NC materials are attractive since the emission wavelength of NCs can be tuned by simply changing the size

due to the quantum confinement effect.[11, 12] These NC materials are often synthesized out of colloidal solution and can be successfully integrated within OLEDs.[13, 14] Such hybrid NC-organic LEDs grant more flexibility in material selection for realizing different color spectra from visible to infared[15, 16], and provide an alternative and more convenient approach for color targeting and large-area manufacturing.

1.2   Scope of This Dissertation

The main focus of this dissertation is to develop a strategy for making efficient hybrid nanocrystal-OLEDs (NC-OLEDs) with silicon nanocrystals (SiNCs). The rest of this chapter will introduce the basics of organic semiconductors and the operation mechanism of OLEDs. Chapter 2 will discuss the theory of quantum confinement and progress in NC-OLEDs, where the motivation of this dissertation will be addressed. The following chapters (Chapter 3 to Chapter 5) will present detailed strategies for efficient SiNC-OLEDs. Chapter 3 will demonstrate the electroluminescence from hybrid-material device made with colloidal SiNCs. Device design and the emission mechanism will be discussed. In addition, potential bottlenecks for device performance will be identified in this chapter. Chapter 4 will introduce the design framework for highly efficient SiNC-OLEDs. The perspective of device engineering in device architecture and charge confinement provides the possibility in realizing highly efficient EL from SiNCs. In addition, efficient EL at different wavelengths will also be demonstrated by using SiNCs with different sizes, achieving the tunability of emission wavelength from the same emitting material. Chapter 5 will examine the micro-scale aspect of material engineering

by understanding the impact of fundamental material properties on the device performance. It is proved that the coverage of the surface ligand on SiNCs could potentially affect the charge transport and confinement during the device operation, which could essentially be a key factor when highly efficient SiNC EL is interested. Chapter 6 will introduce a new device fabrication scheme for the next-generation SiNC LED fabrication, in which the device is made by a dry, all-gas-phase process. This technique has successfully demonstrated that efficient EL can even be realized from single-layer SiNC-LEDs where the SiNC layer is sandwiched between two electrodes. Chapter 7 will conclude this dissertation and propose future research directions for this work.

1.3   Bonding in Organic Solids

Unlike the strong covalent bonding found in inorganic semiconductors, the interaction between organic molecules is mediated by van der Waals interactions. The attraction between electrically neutral molecules can result from: (a) Attraction between a permanent dipole and an induced dipole (Debye interaction); (b) Attraction between two permanent dipoles (Keesom interaction); and (c) Attraction between two induced dipoles (London interaction).[17] Generally, the interaction energy of organic molecules is about 10^{-3} to 10^{-2} eV, much smaller than that of covalent-type interaction in inorganic semiconductors (2-4 eV).[18] This weak bonding affords organic semiconductors advantageous processibility over their inorganic counterparts.

1.4 Organic Semiconductors: Conjugated Systems and Delocalized π Orbitals

Conjugated organic materials, i.e., polymers or small molecules with alternating single and double bonds along the backbone or the ring of the molecule, exhibit different electronic bonding structures than those present in non-conjugated materials, or insulators. In addition to a symmetric electron distribution (σ bond) arising from sp^3 hybridized covalent bonds, conjugated polymers and small molecules also have π bonds, stemming from the overlap of p_z orbitals as a result of continuous sp^2 hybridization of adjacent carbon atoms along the backbone. This overlap leads to the formation of delocalized electron clouds above and below the bonding plane. For example, benzene has a conjugated aromatic structure as shown in Figure 1.1 with six-p_z-orbital bonding, which leads to the well-known delocalized electron density above and below the planar aromatic structure.[19] This delocalization not only stabilizes the electrons in the molecule, but also provides additional space for electron conduction.
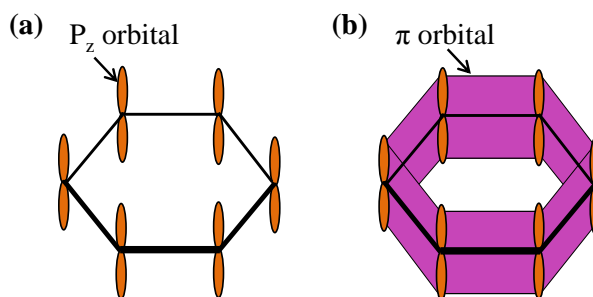
Figure 1.1 The sp^2 hybridization of the p_z orbitals. (a) six p_z orbitals, (b) π orbitals.

1.5   Molecular Orbital Theory: Energy Levels in Organic

Semiconductors

Without a strong covalent bonding interaction between organic molecules, the valance and conduction bands of organic semiconductors do not resemble those of their inorganic counterparts. Molecular orbital theory, based on a linear combination of atomic orbitals, is used to understand the electronic bands in organic semiconductors. As depicted in Figure 1.2, when p orbitals of the carbon atoms overlap in a parallel manner, a set of bonding (σ, π) and anti-bonding orbitals (σ^*, π^*) can form and the overlapped π orbitals of double bonds can result in degeneracy of the molecular orbitals. As the number of the conjugated units in the molecule increases, the π and π^* orbitals of the molecule broaden and form a filled and unfilled band, respectively, labeled as the highest occupied molecular orbital level (HOMO) and the lowest unoccupied molecular orbital
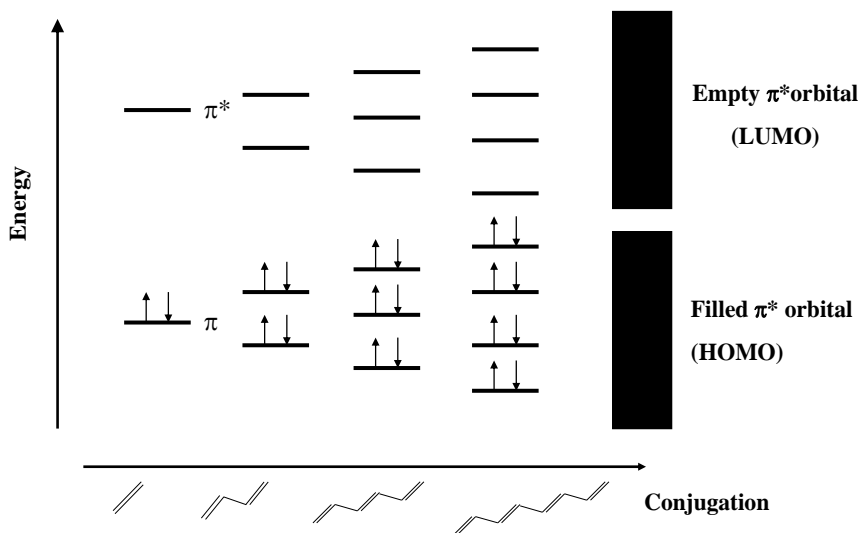
Figure 1.2 Filled and empty molecular orbitals. Note that the HOMO and LUMO refer to the highest occupied molecular orbital level and the lowest occupied molecular orbital level, respectively.

level (LUMO). The HOMO and LUMO are equivalent to the valance and conduction bands in inorganic semiconductors. Typically, the values of HOMO and LUMO for organic small molecule thin films are determined by photoelectron spectroscopy (UPS)[20, 21] and inverse photoelectron spectroscopy (IPES)[22], respectively. The HOMO and LUMO values of polymer molecules are usually measured by cyclic voltammetry (CV).[23]

1.6 Molecular Excited States

When an organic semiconductor molecule is optically excited, an electron is promoted from its ground state (HOMO) to an excited state with a hole left behind in the ground state. The mutual Coulomb attraction between the negatively charged electron and positively charged hole creates a bound electron-hole pair, which is referred to as an exciton. In this case, the excited molecules remain charge neutral and the exciton is usually localized within the molecule.

In organic materials, the excitons are classed as Frenkel excitons.[24] Due to the low dielectric constant of this class of materials (typically ~1 to 5), the strong Coulomb binding interaction usually results in a large exciton binding energy (typically ~ 0.2 to 1.6 eV)[25] and a short distance (< 0.5 nm) between the tightly bound electron-hole charges.[24] On the contrary, excitons generated in inorganic systems are usually at the other extreme. With the high dielectric constant of inorganic materials, the Coulomb interaction between bound electron-hole charges is electrostatically screened, resulting in a small exciton binding energy and a large distance in between the electron-hole pair. The excitons in this limit are called Wannier-Mott excitons, most commonly observed in inorganic crystalline

systems. Wannier-Mott excitons typically have a radius of about 4 to 10 nm, and a binding energy at the scale of meV. For example, in bulk materials, the exciton binding energy is 4.9 meV for GaAs, 5.1 meV for InP, 14.7 meV for Si, 15 meV for CdS, 27 meV for CdSe, etc.[26, 27] Since the binding energy of Frenkel excitons is at least one order of magnitude higher than that of Wannier-Mott excitons, the Frenkel exciton states are more stable at room temperature, whereas the thermal energy (~25 meV) is often enough to dissociate Wannier-Mott excitons.

1.6.1 Singlet and Triplet Excitons

In the molecular ground state, each orbital has an electronic configuration of two paired electrons: one with electron spin up and one with electron spin down. When an exciton is created by optical excitation, one of the unpaired electrons is left in the HOMO level and the other is promoted to an excited state. Typically, the spin configuration before and after the optical excitation follows the spin conservation rule, i.e., the spins of the two electrons are paired (one up and one down). This type of exciton state is referred to as the "singlet". However, if the exciton undergoes further process (intersystem crossing, which will be discussed shortly) or is formed by electrical excitation, each unpaired electron could have an independent electron spin orientation (up or down). This process can be visualized by using the vector model as shown in Figure 1.3. This model treats the electron spin as a rotating vector with an orbital momentum. The individual vectors represent the state of either spin up or spin down. Due to the four possible combinations of spin orientations, the exciton can be divided into two types based on

their spin degeneracy (S): singlet (S=0) and triplet (S=1). The singlet is one state containing two anti-parallel spin vectors, resulting in net spin (S) equal to zero (Figure 1.3(a)), while the triplet consist of three states with a net spin (S) equal to one (Figure 1.3 (b) to (d)). Theoretically, models of spin statistics predict that triplet formation via electrical excitation is three times as likely as singlet formation.[28-30] This ratio has been proved experimentally in organic small molecules.[31, 32] As for polymers, the singlet-to-triplet ratio can range from 1:1 to 1:3.[32-34] In the ground state, most unexcited molecules must have paired spins with opposite orientation occupying the same orbital. Hence, the ground state is of singlet character. Typically, the energy state of the lowest triplet is lower than that of the singlet due to the minimized electron-electron repulsion at the triplet states.[35, 36]

Singlet S=0   Triplet S=1

(b) $|\chi_1\chi_2\rangle = |\uparrow\uparrow\rangle$ χ_1 χ_2

(a) $|\chi_1\chi_2\rangle = \frac{1}{\sqrt{2}}\left(|\uparrow\downarrow\rangle - |\uparrow\downarrow\rangle\right)$ χ_1 χ_2

(c) $|\chi_1\chi_2\rangle = \frac{1}{\sqrt{2}}\left(|\uparrow\downarrow\rangle + |\uparrow\downarrow\rangle\right)$ χ_1 χ_2

(d) $|\chi_1\chi_2\rangle = |\downarrow\downarrow\rangle$ χ_1 χ_2
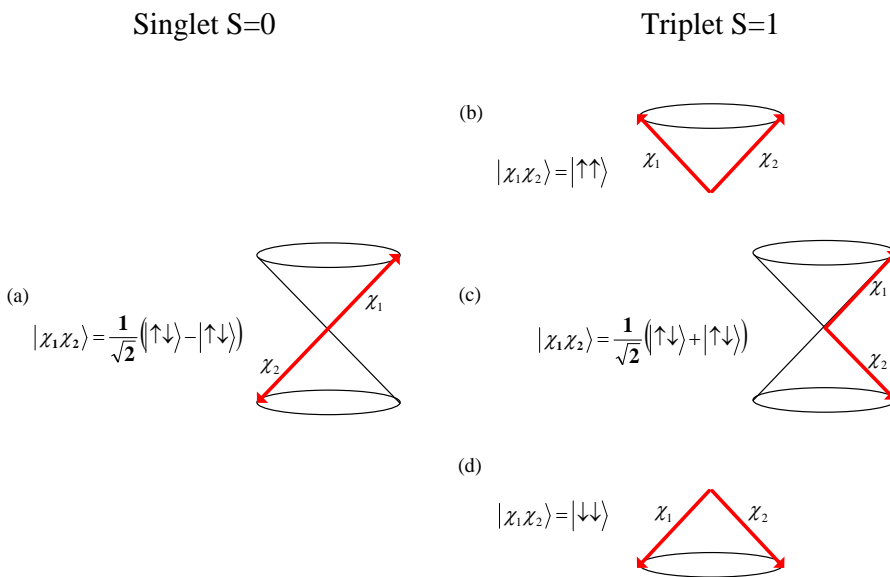
Figure 1.3 Illustration of four possible exciton spin combinations. (a) Singlet S=0; (b), (c), and (d) Triplet S=1. (Image reproduced from Reference 35)

1.6.2 Luminescence

Excitons can relax and recombine by either non-radiative or radiative means. Non-radiative relaxation is usually associated with lattice vibration and phonon emission. Luminescence is a radiative transition of the electrons from the excited states to lower energy states accompanied with emission of photons. The efficiency of luminescence is determined by the rates of both radiative and non-radiative processes, as shown in Equation 1.1, where k_R and k_{NR} denote the rate constants of radiative and non-radiative decay processes, respectively. The intrinsic ability of a material to emit light under optical excitation is known as the photoluminescence (PL) efficiency. Note that this efficiency is also experimentally defined as the rate of photon emission (n_p) divided by the rate of photon absorption (n_a)

$$\eta_{PL} = \frac{k_R}{\left(k_R + k_{NR}\right)} = \frac{n_p}{n_a} \tag{1.1}$$

The luminescence is usually affected by non-radiative processes, which can originate from bimolecular exciton quenching, defect quenching, or phonon (vibrational) relaxation.[35]

There are two types of luminescence, fluorescence and phosphorescence, depending on the nature of the exciton.[37] The difference between the two kinds of luminescence can be illustrated by the energy-level diagram proposed by A. Jablonski (Figure 1.4). After light absorption, the electron can be excited to form a higher singlet energy level such as S_1 or S_2. The relaxation from S_2 to S_1 is called internal conversion. Fluorescence is the emission from excitons the lowest excited singlet state to the ground singlet state with lifetime near 10^{-9} to 10^{-8} seconds. On the contrary, when the singlet is created, it can be

possible converted to triplet state. Such non-radiative transitions from one spin to a different spin orientation between excited states is called intersystem crossing. Phosphorescence is the radiative relaxation of excitons from the triplet excited states (generally the lowest triplet excited state) to the ground singlet state with lifetimes that can be as long as milliseconds to seconds.[37] The typical time scale for the described process is summarized in Table 1.1.[38] Generally, phosphorescence is less common than fluorescence because of the following two reasons. First, the intersystem crossing from singlet to triplet state is quantum mechanically unfavorable. During the state transition, spin flip is required, which does not follow the conservation of spin symmetry. Second, the radiative relaxation from triplet to singlet ground state is also forbidden. Instead, the triplet state can undergo non-radiative routes before phosphorescence occurs, such as triplet-triplet annihilation or triplet-polaron quenching.[39]
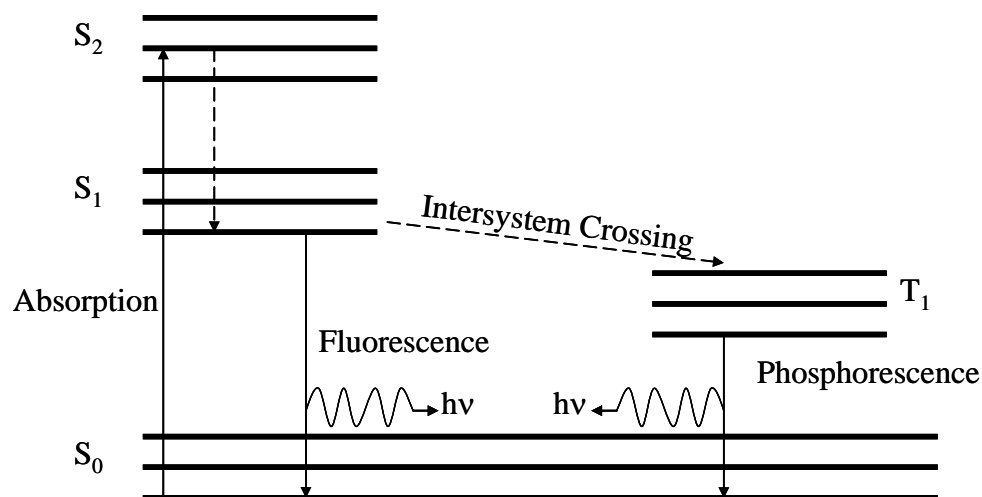
Figure 1.4 Jablonski diagram: illustration of absorption, fluorescence, phosphorescence and intersystem crossing (Image reproduced from Reference 37).

11

Table 1.1 Summary of photophysical processes[38]

Name	Time Scale (sec)
Absorption	10^{-15}
Internal Conversion	10^{-12} to 10^{-6}
Intersystem Crossing (singlet to triplet)	10^{-12} to 10^{-6}
Intersystem Crossing (triplet to singlet)	10^{-9} to 10^{-1}
Vibrational relaxation	10^{-13} to 10^{-12}
Fluorescence	10^{-9} to 10^{-7}
Phosphorescence	10^{-6} to 10^{-3}

1.6.3 Phosphorescence in Organic Semiconductors: Spin-Orbital Coupling

Although phosphorescence is a forbidden relaxation process with different spin symmetries between the excited state (triplet) and ground state (singlet), the complete process, including intersystem crossing from singlet to triplet and triplet relaxation, can be allowed by introducing the interaction between the electron orbital motion and the corresponding electron spin rotation. Such interaction is referred to as the spin-orbit coupling interaction, which induces a magnetic torque within molecules and could rephrase or flip the electron spin during the process. Typically, such effect is enhanced as the charge of the nucleus Z increases, and is usually seen in heavy metal (d^6) complex which contains third- or second-row elements, such as iridium (III), platinum (II), osmium (II), or ruthenium (II).[40, 41] The change in the orbital momentum (induced magnetic torque) could balance the change in the spin momentum, resulting in conserved total momentum. Therefore, this process mixes the nature of singlets and triplets, removes the spin-forbidden nature in intersystem crossing, and thus allows efficient

phosphorescence.[9, 10, 40, 42] As a result, the devices utilizing the phosphorescent materials have achieved very high efficiency in performance.

1.6.4 Energy Transfer in Organic Semiconductors

In organic semiconductors, energy can be transferred either radiatively or non-radiatively. For the radiative mechanism, energy can be transferred into a two-step process. The excited molecule (D*) can relax from the higher-energy state to the ground state through the emission of photons. The emitted photons can then be absorbed by an acceptor molecule (A) which therefore becomes excited:

$$D^* \rightarrow D + h\nu \tag{1.2}$$

$$A + h\nu \rightarrow A^* \tag{1.3}$$

This process is often called cascade or trivial energy transfer, and is useful for energy transfer over large distances (>10 nm). A strong overlap between the donor emission and the acceptor absorption spectrum is required for this process to occur.

Energy may also be transferred via non-radiative processes. One such process, Förster or resonant energy transfer,[24, 35, 43, 44] also depends on the overlap between absorption and emission spectra. This process is based on the Coulombic interaction, i.e. the dipole-dipole coupling mechanism, which is shown in Figure 1.5.[35] The orbital oscillation of the electron 1 induces a similar orbital oscillation of election 2. This may cause the inductive excitation of electron 2 with relaxation of electron 1, i.e., energy transfer may occur:

$$D^* + A \rightarrow D + A^*.$$

13
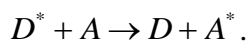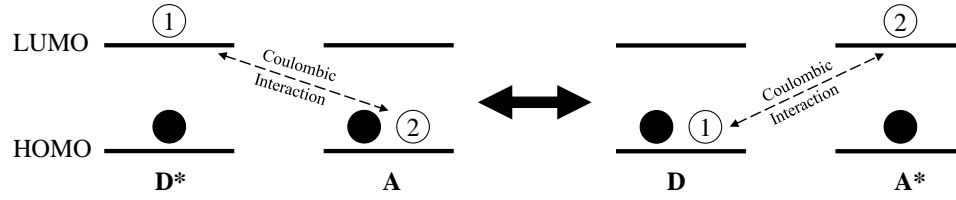
Figure 1.5 Förster energy transfer: Note that the solid circles refer to the passive electrons whose interactions with other electrons are assumed to be roughly the constant during the process of energy transfer. The HO and LU mean the highest occupied electron state and lowest un-occupied electron state (Image reproduced from Reference 35)

In other words, Förster energy transfer is the absorptive transition of energy between electron 1 and 2 without the occurrence of photon emission. The rate of energy transfer by dipole-dipole coupling can be expressed as[24]:

$$K_{D \to A} = \frac{1}{\tau_D} \frac{1}{R^6} \left(\frac{3}{4\pi} \int \frac{c^4}{\omega^4 n_0^4} F_D(\omega) \sigma_A(\omega) d\omega \right),$$ (1.4)

where R is the mean separation between donor and acceptor molecules, F_D is the normalized fluorescence emission spectrum of the donor, σ_A is the normalized acceptor absorption cross section, n_0 is the index of the refraction of the surrounding medium, c is the speed of light, τ_D is the natural lifetime of the donor in the absence of quenchers, and integration is over all the angular frequencies (ω). Note that in this process, the donors have to be emissive to serve as donors in energy transfer. Equation 1.4 can be written as[2424]:

$$K_{D \to A} = \frac{1}{\tau_D} \left(\frac{R_0}{R} \right)^6,$$ (1.5)

where R_0 is the critical separation of donor and acceptor at which energy transfer from D* to A (or Förster radius) and emission from D* have equal probability. If R>R_0, the

14

deactivation of D* (emission) dominates. If $R < R_0$, energy transfer dominates. Typical values of R_0 in organic semiconductors are from 50 to 100 Å.[43]

Another non-radiative energy transfer mechanism is by electron exchange at short range between two molecules. This process can be treated as a collision mechanism because the electron clouds of the donor and acceptor need to overlap significantly in space, and interpenetrate each other for efficient transfer.[35] The exchange can happen simultaneously between a donor and acceptor, or in several steps via a radical ion pair, or even through the formation of chemical bonding in an intermediate species. The visualization of the exchange mechanism is shown in Figure 1.5.

Dexter has shown the rate of the transfer as[24]:

$$K_{D \to A} = \frac{2\pi}{\hbar} |\beta_{DA}|^2 \int F_D(E) F_A(E) dE , \qquad (1.6)$$

where β_{DA} is the exchange energy interaction between donors and acceptors, E is the energy, $F_D(E)$ and $F_A(E)$ are the normalized photoluminescence spectrum of the donor and the absorption spectrum of the acceptor, respectively. If the hidden separation and concentration dependence in β_{DA} are taken into consideration, then the above rate equation can be approximately rewritten into the form as follows[35, 45]:

$$\beta_{DA} = K \exp(-2R_{DA}/L), \qquad (1.7)$$

where K is the specific orbital interaction, R_{DA} is the donor-acceptor separation, and L is the van der Waals radius. As shown in this equation, for electron exchange, the rate of transfer drops exponentially as R_{DA} increases to more than one or two molecules, typically 5 to 10 Å.
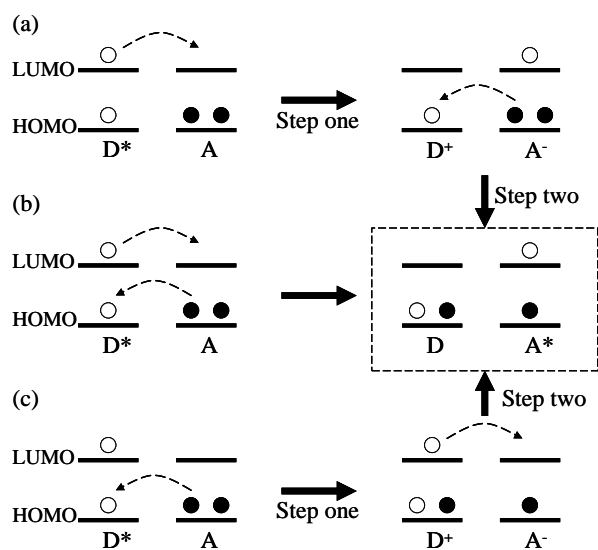
Figure 1.6 Dexter energy transfer: D and A refer to donor and acceptor molecules; HOMO and LUMO mean the highest occupied electron state and lowest unoccupied electron state. (a) HOMO to HOMO electron exchange; (b) converted (simultaneous) electron exchange; (c) LUMO to LUMO electron exchange. Note that open circles refer to the electrons from the donor molecule D. The solid circles refer to the electrons from the acceptor molecule A (Image reproduced from Reference 35).

1.7   Charge Transport in Organic Semiconductors

Charge transport in semiconductors is usually characterized by the magnitude and the temperature dependence of the mobility. Mathematically, the mobility is defined as a proportional coefficient which correlates the drift velocity of charges to the applied electric field, as shown in Equation 1.8.

$$v_d = \mu E \tag{1.8}$$

where v_d is the drift velocity of the carriers, μ is the mobility in unit of cm^2/V-s, and E is the applied electric field. In inorganic semiconductors, the mobility is commonly measured by Hall effect or field-effect.[46] Typically, in crystalline inorganic semiconductors such as Si and GaAs, the electron mobility is commonly observed on the order of 10^3 to 10^4 cm^2/V-s.[46] In organic semiconductors, on the other hand, the mobility

16

is usually measured by various techniques, including time-of-flight[47-50], charge dissipation[51], transient current[52], and device configuration[49, 50]. The device configuration method involves either a diode or a field effect transistor (FET)[49, 53-55], where the former is usually adopted for characterization of the bulk material mobility using the space-charge limited current model[26, 56, 57]. The FET is typically employed for determining the charge behavior in transport within a very narrow channel at the interface between organic semiconductor and the dielectric.[53, 54] Typical bulk mobility from time-of-flight method is on the order of 10^{-8} to 10^{-4} cm^2/V-s.[58, 59] However, in organic single-crystal systems, electron mobility (measured by FET) larger than 1cm^2/V-s and hole mobility higher than 10 cm^2/V-s can be observed.[60]

Charge transport in semiconductors is generally described by two well-known models, i.e., the band model and the hopping model. The band-like model applies when charge carriers move as a highly delocalized plane wave in a band-like structure, created by the periodic lattice potential under Bloch conditions.[24, 61] On the contrary, the hopping model prevails when the charge carriers are highly localized on molecules or defects. In this case, the charges are no longer considered as a free-moving plane wave and are instead activated by thermal energy to hop from one site to another.[24, 49, 50] Generally, the charge transport mechanism in organic semiconductors is considered as a case in between these two extremes.[24]

The band theory is usually used for explaining the charge transport in crystalline systems, including most inorganic semiconductors. In band theory, the energy band for charge carrier transport is formed through the periodic lattice interaction. By solving the

Schrödinger equation for a periodic crystal potential established by the cores, a Bloch wavefunction is obtained showing high level of delocalization of the carriers in crystalline systems. The carriers move in the material with wide bands and exhibit the transport behavior characterized by the temperature dependence of mobility as[24]:

$$\mu \propto T^{-n}, n > 1 \tag{1.9}$$

However, in organic semiconductors, since the molecules are bound together by much weaker van der Waals interaction as opposed to the strong covalent coupling in their inorganic counterparts, this class of materials typically exist in forms of amorphous or polycrystalline solids. As a consequence, the Bloch theorem breaks down in this case as the overlap of the wavefunctions between neighboring molecules is significantly smaller, giving rise to smaller carrier mean free path than the lattice constant; in other words, the charge carriers are highly localized due to the disrupted lattice potential distribution. The hopping model, therefore, manifests more validity in describing the charge transport behavior in most organic semiconductor systems.

The hopping model is typically employed to describe disordered systems which have the mean free path of the charge carriers comparable to the lattice constant. The material system usually has a random potential distribution, such as aforementioned organic semiconductors, where the carrier is localized within an energy well, awaiting for reception of sufficient thermal activation energy to overcome the potential well to hop from one potential well to another. The energy well here is usually created by a defect or by the polarization of a lattice site where the charge carrier resides for a certain amount of time. In the latter case, the carrier and its associated lattice deformation are defined as a

polaron. In hopping theory, the thermal energy to activate the carrier hopping is usually provided by the phonon vibration of the system, i.e., the hopping mechanism is phonon-assisted. The dependence of mobility on temperature in this case is given by[24]:

$$\mu \propto \exp(-E_A / k_B T) \tag{1.10}$$

where E_A is the activation energy, k_B is the Boltzmann's constant, and T is the temperature. This dependence is associated with the probability of carriers to hop between two sites and follows the exponential relationship from Arrhenius law.

1.8   Recent Progress in Organic Light-Emitting Devices

Electroluminescence (EL) in organic crystals (anthracene) was first observed by Pope et al. and Helfrich et al.[62, 63]   The EL from 10-20 μm thick anthracene crystal was first found at voltages exceeding about 400 V.[62] In several following works, the driving voltage was reduced but EL was still able to be characterized with external quantum efficiency of about 0.05%.[63-67] In 1987, Tang first reported a vacuum sublimed thin-film device with a high external quantum efficiency up to about 1% and a low driving voltage of below 10 V.[8] In 1990, Burroughes et al. reported the first polymer OLED fabricated by spin-casting the conjugated polymer PPV [poly(phenylenevinylene)].[68]

Although the EL efficiency is improved by doping the host polymer with highly fluorescent molecules[69], the internal quantum efficiency of traditional fluorescent OLEDs is limited by exciton spin statistics. In most fluorescent materials, only 25% of the excitons (singlets) formed under electrical excitation can emit light while the rest (triplets) undergo non-radiative recombination.[36, 70] However, with the development of

19

efficient phosphorescence from organic semiconductors containing heavy metal elements[9, 9], the internal quantum efficiency can approach 100% by doping phosphorescent dyes into a wide band-gap host material, leading to almost 20% external quantum efficiency.[10] The emission mechanism in this host-guest system will be explained in the following sections.

1.9 Operation Mechanism in OLEDs and External Quantum Efficiency

In OLEDs, the device structures typically are planar structures with the emissive layer sandwiched in between the electrodes or charge transport layers (Figure 1.7 (a) and (b)). The emitter materials often have either hole-transporting or electron-transporting charge transport characteristics (Figure 1.7 (c) and (d)). The EL occurs through the following succession of events: the injection of electrons and holes from cathode and anode, respectively, followed by charge transport through the charge transport layers, formation of excitons at the emissive layer, and light emission as a result of electron-hole recombination (Figure 1.7 (e) and (f)).

In OLEDs, the external quantum efficiency (EQE) can be defined as the number of photons emitted by the device along the forward viewing direction per electron injected into the device. In terms of other materials and device parameters, the EQE can be defined as[36]:

$$EQE = \gamma \times \chi \times \eta_{PL} \times \eta_{OC} \tag{1.11}$$

20
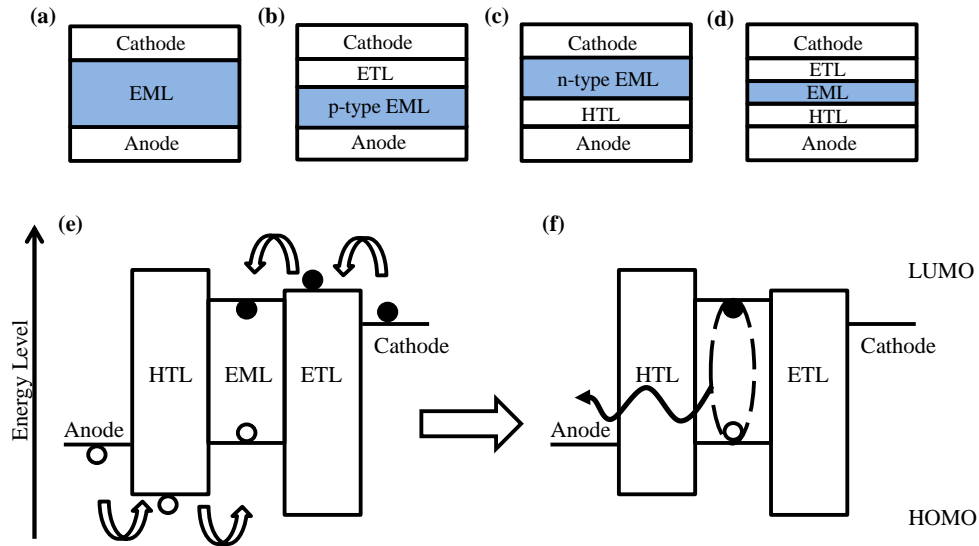
Figure 1.7 (a)-(d) Illustration of the structure of planar structure of OLEDs and (e)-(f) schematic of their operation mechanism.

The quantity γ is the coefficient of charge balance, which represents the fraction of injected carriers that form excitons in the emissive layer.[36, 71] Due to the barrier for charge injection from metal to organic semiconductor and the different carrier mobilities for electrons and holes in the charge transport layers, the charge population may not be balanced in the emissive region, leading to the possibility of leakage current with a reduced exciton formation. The second factor, χ, is called the spin fraction. Simple spin statistics suggest that the ratio of singlets to triplets is 1:3.[31, 32] Singlet excitons may undergo radiative relaxation, while this process is usually forbidden for triplet excitons. Therefore, in a typical OLED, 75% of the excitons will be lost in non-radiative processes. However, even during the singlet exciton recombination, not all excitons decay radiatively, due to the presence of competing non-radiative paths for exciton relaxation. This is accounted for in the photoluminescence efficiency (η_{PL}) of the material and also the exciton quenching mechanisms in the structure. Finally, η_{OC} is the outcoupling

efficiency that accounts for optical losses that may limit the fraction of emitted excitons that actually escape into the forward viewing direction.[71, 72] Figure 1.8 summarizes the EL emission process and the sequence of efficiency calculation.[22, 71] These four factors state the possible losses of the external quantum efficiency in devices and provide basic directions of minimizing the losses for further performance improvement.
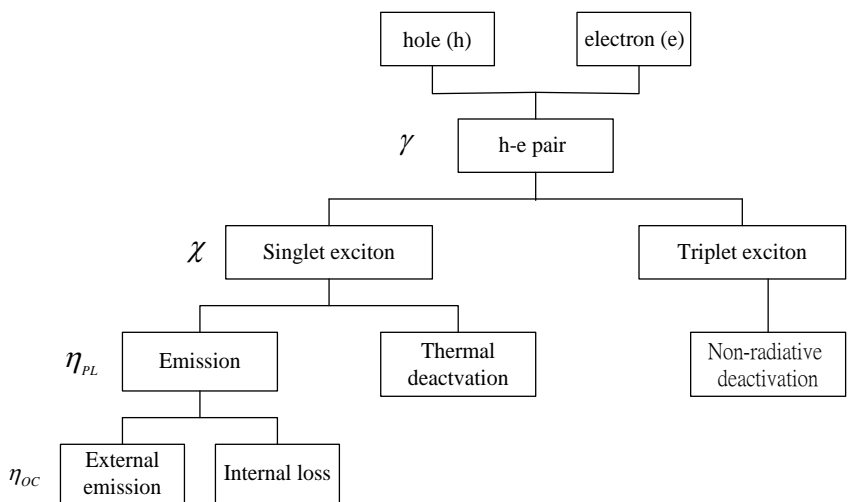
Figure 1.8 Various processes available for exciton relaxation. (Image reproduced from Reference 22 and 71)

1.9.1 Host-Guest System

In OLEDs with a host-guest emissive layer, exciton energy transfer from host to guest can be via either Förster or Dexter processes[71], both allowing the singlet-to-singlet transitions (Figure 1.9). For fluorescent guests, the doped guests can undergo the relaxation from excited state S_1 to the ground state S_0, leading to fluorescence. As for phosphorescent guests, the intersystem crossing happens within the guest materials, which converts the energy state of the guest from singlet to triplet. In addition, the triplet states in guest molecules can also be achieved by the Dexter transfer from the triplet

excited states of the host materials (Figure 1.10). In addition to energy transfer, there might be a possibility of carrier trapping, which also forms excitons on the guest materials. After the relaxation from triplet excited state T_1 to the ground state S_0, guest phosphorescence could be obtained.
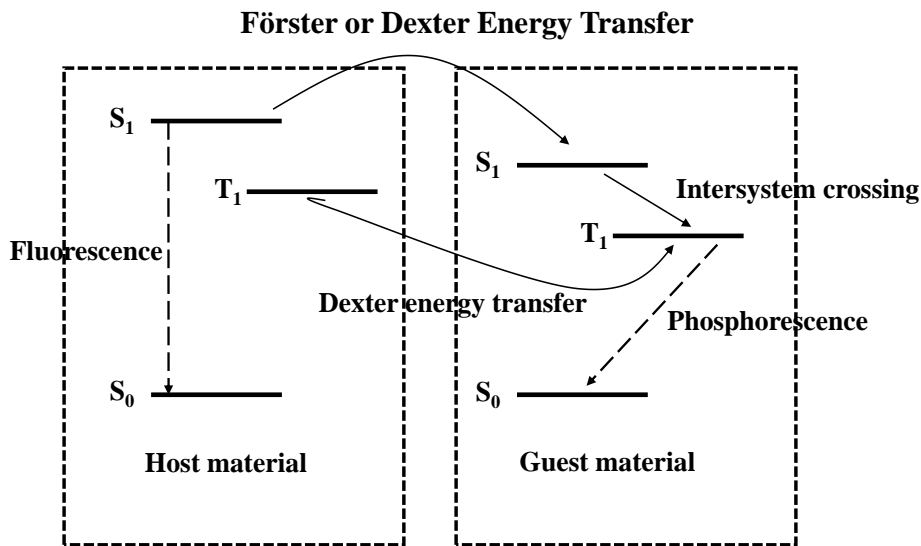
Figure 1.9 Fluorescence, phosphorescence and energy transfer within a host-guest system (Image reproduced from Reference 71).
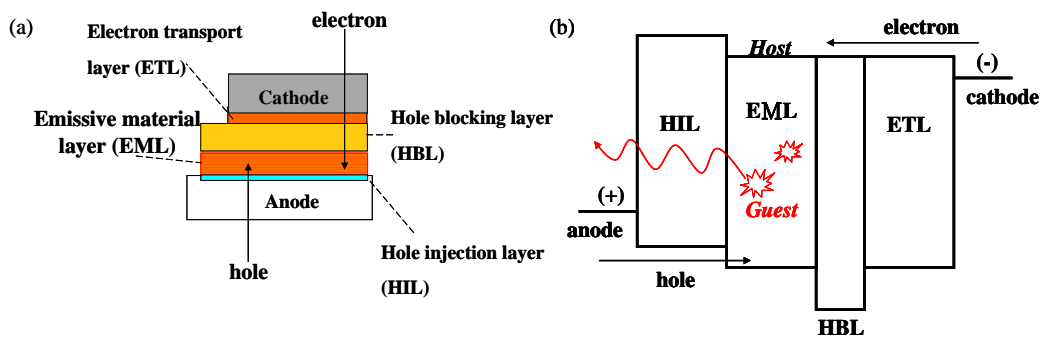
Figure 1.10 (a) Illustration of the structure of host-guest OLEDs and (b) Schematic of their operation mechanism (Image (b) reproduced from Reference 22).

1.9.2 State-of-the-Art OLEDs

While the conventional OLED technology uses either fluorescent or phosphorescent RGB (red, green, blue) dopants in multi-layer structures for most applications, a novel single-layer device structure with a graded heterojunction has been recently proposed. Such device structure eliminates the tedious multi-layer fabrication but still maintains good exciton and charge confinement within one-single layer.[73, 74] White light-emitting OLEDs have also been realized either by including separate RGB emission layers within the device, multi-layer with host-guest structure, or single layer with blended dopants.[75-79] Recently, advanced OLED systems made with II-VI, III-V, or IV-VI inorganic semiconductor emitters have drawn significant attention. Such device architecture offers another potential approach to combining the optical properties of inorganic semiconductors with the electronic properties of organic semiconductors. Due to the advantage in wavelength tunability of nano-scale inorganic semiconductors, emission wavelength engineering from a single material becomes achievable. Multiple EL from such systems have already been demonstrated[11] and will be introduced in next chapter.

Chapter 2 Nanocrystals and Hybrid Light-Emitting Devices

The previous chapter introduced the basic physics of organic semiconductors and organic light-emitting devices (OLEDs). This chapter will cover the fundamental theory of colloidal semiconductor nanocrystals (or quantum dots) and their application in hybrid OLEDs.

2.1 Nanocrystal (Quantum Dot)

In a semiconductor nanocrystal (quantum dot) electrons and holes are confined by a potential barrier in all directions. Its optoelectric properties depend strongly on particle size and deviate from those of the bulk material (Figure 2.1 (a)).[80] Both the absorption energy and emission energy blue shift with a decreasing particle size (Figure 2.1 (b)).[81] This size dependence provides an opportunity to tune the emission of the particles by controlling their diameter, permitting various applications[11, 82-84], including in light-emitting devices[11-13, 85], solar cells[11, 86-88], and biological labels.[89-95]

2.2 Quantum Confinement in Nanocrystals

The size dependence effect of a semiconductor occurs when material dimensions become smaller than the excitonic Bohr radius of the bulk materials, defined as[96]:

$$a_B = \varepsilon \frac{m}{m^*} a_o,$$
(2.1)

where ε is the dielectric constant of the nanocrystal m* is the effective mass of the NC, m is the electron rest mass, a_o is the Bohr radius of the hydrogen. For example, the calculated value for cadmium selenide (CdSe) is ~ 60 Å[96], and is ~50 Å for silicon.[97, 98]

When the particle size is below this natural length scale of electron-hole pair a_B, the exciton will experience confinement by the physical boundaries. This quantum sizing feature also forces the energy bands to split into discrete levels, leading to a quantized density of states in both bands (Figure 2.2).[99]

2.3   Quantum Mechanical Model of Quantum Confinement

The quantum confinement effect can be qualitatively explained by a simplified example of the classic "particle in a box" problem of quantum mechanics.[100]

2.3.1   Quantum Confinement in Nanocrystals with a Single Charge

According to the effective-mass approximation proposed by Brus[101, 102], the
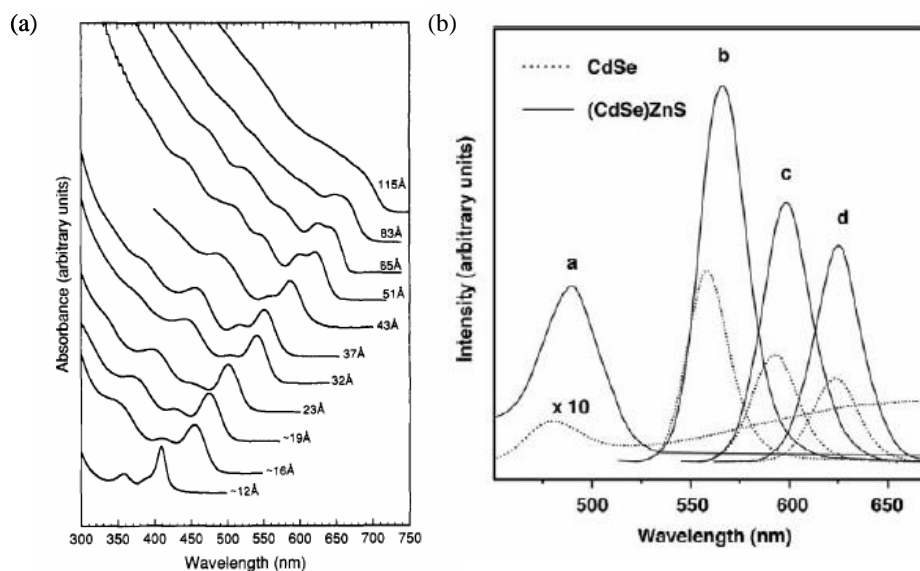
Figure 2.1 The size effect on absorption and photoluminescence of cadmium selenide (CdSe) quantum dots. (a) Room-temperature absorption of the CdSe with the size range ~12 to 115 Å in hexane ; (b) Photoluminescence spectra of bare (dash curves) and Zinc sulfide (ZnS) coated CdSe quantum dots (solid curves). The curve a refers to particle with diameter 23 Å; curve b: 42 Å; curve c: 48 Å; curve d: 55 Å *Data Reprinted with permission from Synthesis and characterization of nearly monodisperse CdE (E = sulfur, selenium, tellurium) semiconductor nanocrystallites, Copyright (1993) American Chemical Society; (CdSe)ZnS Core−Shell Quantum Dots: Synthesis and Characterization of a Size Series of Highly Luminescent Nanocrystallites, Copyright (1997) American Chemical Society
.

26
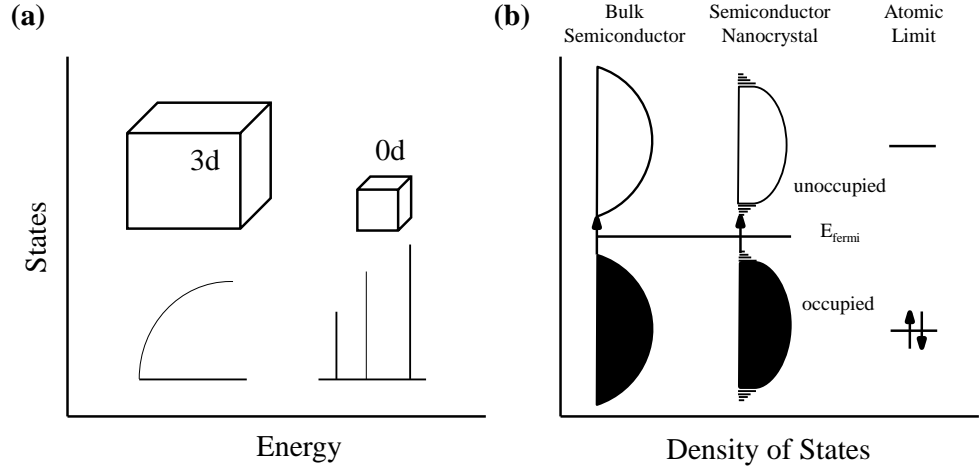
Figure 2.2 Density of states of a semiconductor: (a) Comparison of idealized density of states for one band of a semiconductor material in 3 dimensions (3d) and in 0 dimensions (0d), with 3d bulk materials showing a continuous density of states and 0d case show a molecular like (or discrete) density of states; (b) The change of density of states of a semiconductor from bulk to nanoparticle, and then to the atomic limit. Note that the energy band gap between HOMO and LUMO increases with the decrease of the size of the material, which can be explained by considering analogy to the particle-in-a-box of quantum mechanics (Image reproduced from Reference 99).

Hamiltonian of a single-charge spherical nanoparticle with infinite outside potential can be written as following:

$$H = -\frac{h^2}{8\pi^2 m_c}\nabla_c^2 + \hat{V}; \; \hat{V} = 0 \text{ if } r \leq R \text{ or } \hat{V} = \infty \text{ if } r \geq R, \tag{2.2}$$

where m_c is the effective mass of the point charge, r is the distance from the center of the particle, and R is the radius of the nanoparticle. The Schrödinger equation gives the wavefunction and energy in a spherical system as:

$$\psi_n(r) = \frac{1}{r\sqrt{2\pi R}} Sin\left(\frac{n\pi\, r}{R}\right) \tag{2.3}$$

$$E_n = \frac{h^2 n^2}{8m_c R^2}; \; n = 1,2,3,..... \tag{2.4}$$

Equation 2.3 describes the behavior of an electron in a potential box and also qualitatively describes the shift in the absorption spectra with size.

27

2.3.2 Quantum Confinement in Nanocrystal with an Exciton

Since the excited state of nanocrystals is actually exciton, three interactions should be included in the potential term when constructing the Hamiltonian, namely, the kinetic energy of the exciton, the Coulomb attractive interaction in this electron-hole bound state, and the polarization interaction at crystalline surface.[102]

With the effective-mass approximation, the Hamiltonian can be written as following:

$$H = -\frac{h^2}{8\pi^2 m_e}\nabla_e^2 - \frac{h^2}{8\pi^2 m_h}\nabla_h^2 + \hat{V}(\hat{S}_e, \hat{S}_h); \tag{2.5}$$

$$\hat{V} = \hat{V}_{coul} + \hat{V}_{pol}, \tag{2.6}$$

where m_e and m_h are the effective mass of electron and hole, with the positions $\hat{S}_e$ and $\hat{S}_h$, respectively (Figure 3.3).
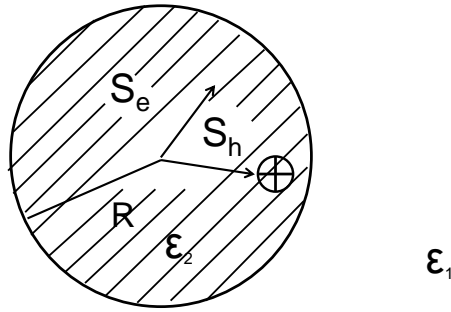
Figure 2.3 The Schematic expression of a spherical nanoparticle with dielectric constant ε_2 embedded in a medium material with infinite boundary and dielectric constant ε_1 (Image reproduced from Reference 102).

Moreover, Coulomb interaction in the potential term can be expressed as:

$$\hat{V}_{coul} = -\frac{e^2}{\varepsilon_2 \left|\hat{S}_e - \hat{S}_h\right|}, \tag{2.7}$$

where ε_2 is the dielectric constant of the semiconductor material.

Also, the polarization term can be written as:

$$\hat{V}_{pol} = \frac{e^2}{2} \sum_{n=1}^{\infty} \alpha_n \frac{((\hat{S}_e)^{2n} + (\hat{S}_h)^{2n})}{R^{2n+1}} , \tag{2.8}$$

where $\alpha_n = \frac{(\varepsilon - 1)(n + 1)}{\varepsilon_2(\varepsilon n + n + 1)}$; $\varepsilon = \frac{\varepsilon_2}{\varepsilon_1}$, ε_1 is the dielectric constant of the medium

surrounding the nanoparticle.

Therefore, the Schrödinger equation $H\Psi_{exc} = E\Psi_{exc}$ can be shown as:

$$[-\frac{h^2}{8\pi^2 m_e} \nabla_e^2 - \frac{h^2}{8\pi^2 m_h} \nabla_h^2 + \hat{V}(\hat{S}_e, \hat{S}_h)]\Psi_{exc} = E_{ex}\Psi_{exc} \tag{2.9}$$

By assuming uncorrelated solution of wave function shown as:

$$\Psi_{exc}(\hat{S}_e, \hat{S}_h) = \Psi_1(\hat{S}_e)\Psi_1(\hat{S}_h), \tag{2.10}$$

and applying the wave function from Equation 3.3 in the previous case for $\Psi_1(\hat{S}_e)$

and $\Psi_1(\hat{S}_h)$, the calculated energy of the lowest excited exciton (the energy shift with

respect to the bulk band gap) is:

$$E_{ex} = \frac{h^2}{8R^2}\left(\frac{1}{m_e} + \frac{1}{m_h}\right) - \frac{1.8e^2}{\varepsilon_2 R} + \frac{e^2}{R} \sum_{n=1}^{\infty} \alpha_n \overline{\left(\frac{S}{R}\right)^{2n}} , \tag{2.11}$$

where the bar in the third term denotes the average of the wavefunction Ψ_{exc}. At small R,

the first term in the solution dominates, which means the sum of kinetic energy of

electron and hole in the system can be roughly approximated as the internal exciton

energy. As a result, this energy is an additional energy with respect to the bulk band gap

energy for creating exciton in the semiconductor nanoparticle. Thus, the calculated

energy band gap (or transition energy E_{tr}) is given by:

$$E_{tr} = E_g + E_{ex}$$ (2.12)

From Equation 2.12, the smaller the quantum size, the larger the band gap between the

HOMO and LUMO, as shown in Figure 2.2 (b) when the size of the nanoparticle has

been decreased toward the atomic limit. The calculated band gap energy for several

semiconductor quantum dots are plotted in Figure 2.4 (a) and are compared with the

experimental data in Figure 2.4 (b). A good agreement between the calculated energy and

the experimental data is found for particles with sizes bigger than 8 nm.[102, 103]
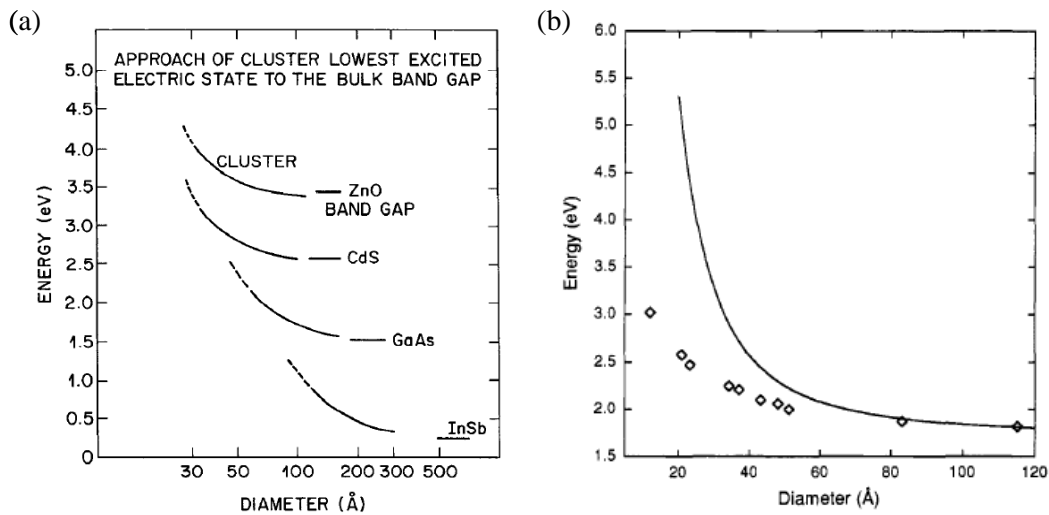
Figure 2.4 (a) Calculated energy of the lowest excited exciton state as a function of diameter of several semiconductor materials by using the effective mass model with Equation 2.11 and 2.12. The short horizontal curve is the energy band gap of bulk materials; (b) Comparison of the predicted theoretical value of the HOMO and LUMO transition energy (effective band-gap energy) from effective mass model (solid line) and the diamonds are the experimental data measured by correlating absorption with TEM analysis *Data reprinted with permission from Electron-electron and electron-hole interactions in small semiconductor crystallites: The size dependence of the lowest excited electronic state, Copyright (1984) American Institute of Physics; The Quantum- Mechanics of Larger Semiconductor Clusters (Quantum Dots), Copyright (1990) Annual review of physical chemistry

With further modification, this calculation is shown to be in a good agreement with the experimental data for several semiconductor materials, such as CdSe, CdS (cadmium sulfide), CdTe (cadmium telluride), and InP (indium phosphide).[104]

2.4   Emission Mechanisms in Indirect and Direct Band-gap Materials

For direct band-gap semiconductor materials, the effective-mass approximation can successfully give a quantitative explanation of the size dependence of the band gap and thus the blue shift of the radiative recombination with decreased nanoparticle diameter. For example, II-VI semiconductor nanoparticles, especially CdSe, provides a good demonstration of this quantum-confinement phenomenon (Figure 3.2 (b)). On the other hand, in indirect band-gap semiconductor materials, the bulk materials normally have weak luminescence while the luminescence in quantum dots can be enhanced and is also tunable by quantum confinement effect.[105, 106]

In indirect semiconductors, a phonon is typically required to fulfill the momentum balance in radiative recombination in bulk materials, such as silicon. In a nanoparticle of indirect semiconductor, however, since the physical size of the material is small, overlap between the tails of wavefunction is likely to occur, responsible for the increase of the radiative recombination rate in the nanocrystals.[107] A further modification of the effective-mass approximation[108] demonstrates that the silicon nanocrystals (SiNCs) have quantum confinement effect, implying the tunable energy window for radiative emission of this material.

2.5   Introduction to Hybrid Nanocrystal-Organic-Light-Emitting

Devices

The emission wavelength of inorganic semiconductor nanocrystals can be easily tuned

by size, while organic phosphorescent materials usually require specific and difficult for

engineering emission wavelength from each different chemical compound.[11, 81, 109, 110]

Similar to OLEDs, by utilizing either energy transfer[9, 36, 111] or charge trapping

mechanisms[112, 113], these nanocrystal materials can serve as emissive materials much like

organic semiconductors. The resultant device is referred to as a hybrid nanocrystal-

organic light-emitting device (NC-OLED). A comparison of the energy band gap, i.e., the

allowed range of tunable emission energy, of various nanocrystals is summarized in

Figure 2.5.[109]
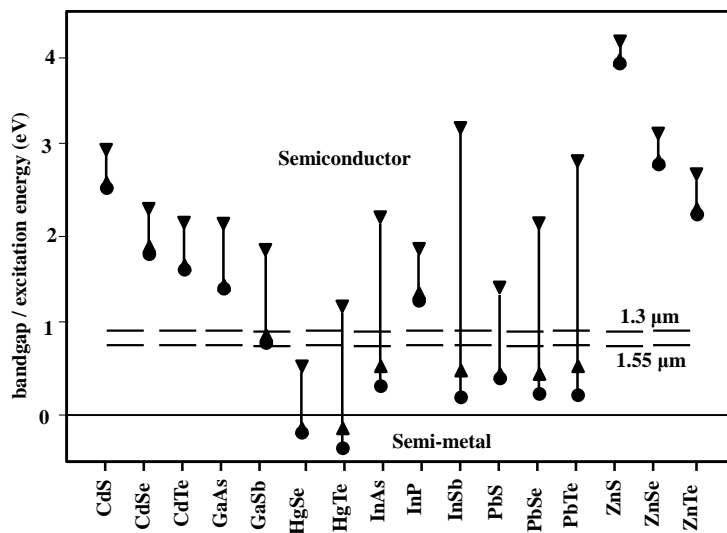
Figure 2.5 Emission tunability of quantum dots: Calculated band-gap energy using a simple particle-in-a-box model. Circles show the band-gap energy of bulk materials. Downward-pointing triangles show energies at 3 nm particles diameters, while the upward-pointing triangles show energies for dots at 10 nm. The energies corresponding to 1.3 □m and 1.5 □m are shown as reference. (Data reproduced from Reference 109)

The NC-OLED is attractive for the development of full-color flat-panel displays and lighting application, since different emission colors in hybrid OLEDs can be achieved by only using a single material. In addition to the ease of wavelength tuning, these inorganic semiconductor nanocrystals also show great compatibility with solution processing owing to the attached surface ligands, which permits devices to be fabricated using high-throughput printing and coating based techniques. [11, 114-121]

The first hybrid OLEDs were created during 1990s with II-VI semiconductor nanoparticles of CdSe, with a conjugated polymer, such as poly-(para-phenylenevinylene) (PPV) or poly-(9-vinylcarbozole) (PVK).[13, 122] These works initiated a tremendous amount of studies with CdSe during these decades.[11, 14-16, 85, 114-129] The external quantum efficiency of devices first observed was only reported as 0.001%.[13] To date, attention has been paid almost exclusively to studies of group II-VI, III-V, and IV-VI semiconductor nanocrystals. [11, 14-16, 85, 114-129] In 2009, light-emitting devices based on CdSe/ZnS core-shell nanocrystals have been demonstrated with a high η_{EQE} of ~2.7% for EL at a wavelength of λ~600 nm.[15] Several works on enhancement of the device performance have been proposed. Table 2.1 summarized the up-to-date emissive materials used and corresponding device efficiency from literatures.[11] Meanwhile, architectures comprising inorganic transport layers have also been proposed in order to introduce device design and attempt of solving the lifetime issue of organic semiconductors. However, their performance remains lower than in corresponding hybrid structures.[130-134]

Table 2.1 Summary of the progress of nanocrystal electroluminescence.

Nanocrystals	Reported Wavelength (nm)	Reported External Quantum Efficiency	Turn-on Voltage (V)	Year
CdSe	580-620	0.001-0.01%	~4	1994
CdSe	530-650	0.0005%	-	1995
CdSe/CdS	613	0.22%	4	1997
CdSe/ZnS	562	0.52%	Estimated ~4	2002
CdSe/ZnS	540-635	>2%	-	2005
ZnCdS	460	0.4%	Estimated ~2.9	2009
ZnSe/CdSe/ZnS	545	2.6%	Estimated ~2.6	2009
ZnCdSe	650	1%	Estimated ~ 2.3	2009
CdSe/ZnS	600	2.7%	Estimated ~2.5	2009

In addition to visible emission for displays[117] and lighting[125], nanocrystals can also be applied to the near infrared region of the spectrum for potential applications in ethernet data links, remote control, and communications.[7, 114] In addition, the infrared spectrum within 700-1100 nm possesses low absorbance and scatter in living tissues, which allows the potential of integration of active emitter materials for tissue imaging or bio-medical device purpose.[91, 92, 94]

Usually, the near-infrared is defined as the wavelength range between ~750 to ~1500 nm. Although CdSe (cadmium selenide) is well studied for the visible emission, it cannot fulfill the emission in this region due to the limit of its tunable band gap. Therefore, several quantum dot nanocrystals are reported as substitutes for CdSe, such as PbS (lead sulfide), PbSe (lead selenide), and InAs (indium arsenide). These NCs emit over a

wavelength range of λ=1000-1600 nm, with external quantum efficiencies (η_{EQE}) ranging from 0.001% to 2%.[85, 120, 121, 123, 124, 127, 135, 136] The first paper on near infrared (NIR) hybrid NC-OLEDs was based on the composites of core-shell InAs/ZnSe (indium arsenide/zinc selenide) nanocrystals with polymer host, and remarkably high external quantum efficiency (EQE) of 0.5% at 15 V was demonstrated.[85] With the continuous development over decade[137, 138], the highest EQE reported so far has reached 2% at 1.2 V in devices using PbS.[121] Recent studies on PbSe, PbS, and HgTe (mercury telluride) nanocrystals are summarized in Table 2.2.

Table 2.2 Summary of reported near-infrared-nanocrystal electroluminescence.

Nanocrystals	Reported Wavelength (nm)	Reported External Quantum Efficiency	Turn-on Voltage (V)	Year
Core-shell InAs/ZnSe	1300	0.5%	15	2002
PbS	1400	-	3	2003
PbSe	1495	0.001%	10	2003
HgTe	1300	0.001%	-	2004
HgTe	~1600	0.02% (at 2.5 V)	-	2005
CdSe/CdS	890	0.02%	7	2007
PbS	1200	1.15%	1	2008
PbSe	1280	0.83%	3	2009
PbS	1050	0.7%	2	2012
PbS	1054	2.0%	1.2	2012

2.6 Luminescence from Silicon

Bulk silicon is well-known as an inefficient emitting material due to its indirect-band gap.[107, 139] In 1990, the first reported red luminescence from Si was obtained in porous silicon as a result of the quantum confinement effect.[140] The photoluminescence efficiency of the discovered silicon emission was ~ 1%, which is five orders of magnitudes higher than that of bulk silicon.[140, 141] As a result, research interest in silicon luminescence drastically grew during the 1990s.[142-146] The most popular research focused on silicon materials at the nanoscale, especially the zero- dimensional SiNCs.[107, 139] By engineering the size of nanocrystals, the possible emission from ultra-violet to near-infrared wavelength has demonstrated achievable. In addition, the PL efficiency has undergone rapid improvement over decades, from 1% to more than 60%.[147] Such enhancement in PL provides a solid foundation for silicon materials serving as an efficient emitter as alternative to II-VI NCs and organic phosphorescent materials, providing them a great opportunity for optoelectronic applications in semiconductor industry.

Typically, SiNCs can be synthesized through different routes, categorized by the phase of the reactions: liquid or gas phase. The traditional synthesis of SiNCs is through electrical etching of bulk silicon in the mixture of HF and H_2O_2[148, 149], while another type of synthesis of SiNCs is by chemical reduction of silicon based materials.[150] Luminescent SiNCs could be easily prepared by sonicating Si powders within the mixture of HF and HNO_3.[151] The solution synthesis of SiNC was first introduced by Heath in 1996.[152, 153] Among these liquid-phase methods, the adoption of inverse micelle for SiNC growth

matrix serves as a better route in particle size control.[146] Recently, novel gas-phase synthesis of SiNCs has been developed through thermal decomposition of organosilanes and a gas-phase plasma process. Such gas-reaction also provides another effective way for small SiNC growth with luminescence tunability.[154-158] Usually, the synthesized SiNCs from both methods are passivated by oxide shell or organic ligands in order to prevent the further oxidation or aggregation of SiNCs.[147, 159, 160] The latter passivation method can successfully enhance the material photoluminescence efficiency to as high as > 60%.[147] In addition to the PL increase, the organic ligand can also increase the solubility of SiNCs in organic solution, allowing the realization of "silicon ink" for solution process, such as printing or coating, in device fabrications.[161]

2.7 Motivation: Silicon Nanocrystal-OLEDs

Silicon nanocrystals exhibit a great potential in both research and applications among semiconducting materials. Although the synthesis of II-VI semiconductors, such as CdSe quantum dots, has been widely studied[162], their potential toxicity, lack of natural abundance, and incompatibility with the silicon microelectronics industry are three main drawbacks of these materials. In contrast, silicon (at least in the bulk), is generally believed to be less toxic to the human body than the II-VI counterparts, such as CdSe. Also, silicon is of high natural abundance, a significant advantage over other rare earth semiconductors. Furthermore, in terms of the microelectronic fabrication, SiNCs are compatible with processes currently used in industry, fascilitating the integration of silicon-based OLEDs with existing device manufacture.[141] Thus, SiNCs have been

intensively investigated over the past decade as an attractive candidate for application in optoelectronics. The first hybrid SiNC-OLEDs were demonstrated by Delgado.[81] This work focused on the use of oxygen passivated-SiNCs cooperating with PVK, which gave a blue emission at wavelength of 450 nm. In 2007, Ligman's work showed a further study of this hybrid structure with SiNCs emitting at 640 nm.[163]

However, it must be emphasized that with the aforementioned impressive improvement of SiNC-OLEDs, problems still persist which largely hinder their further applications. First and foremost, the operation mechanism of this type of devices is not clearly understood. A debate over two different emission mechanisms has never ceased, namely, the direct injection mechanism and energy transfer mechanism. In part due to an incomplete understanding of the device physics, no systematic studies on device efficiency has been reported. Moreover, the previously reported EL is often measured in the presence of parasitic emission from the organic charge transport layers included in the device architecture with very few examples demonstrating the device with pure emission from the active materials. Further issue associated with silicon NC-OLEDs that hampers their commercialization is a lack of fabrication technique that is highly compatible with solution processing and thus possible to achieve high-through-put mass production.

This research presented three studies to realize the highly efficient electroluminescence from colloidal SiNCs. The first part investigated relation of surface morphology to device performance. The second part introduced the study of device structure and the optimized device archetechure for achieving the highly efficient EL from SiNCs. The third part engaged the research and open discussion on the impact of

surface ligands on the performance SiNC-OLEDs. This work sheds lights on the fundamental device physics and provides the guidelines for realizing efficient electroluminescence in hybrid SiNC-OLEDs.

Chapter 3 Near-infrared Electroluminescence from Silicon Nanocrystals

(This work was previously published in: "Cheng, K., Anthony, R., Kortshagen, U. R. & Holmes, R. J. Hybrid Silicon Nanocrystal-Organic Light-Emitting Devices for Infrared Electroluminescence. *Nano Lett.* **10**, 1154-1157 (2010)". Copyright 2010 American Chemical Society)

3.1 Overview

The development of high-yield synthesis routes that utilize non-thermal plasma[164] has led to SiNCs with PL quantum yields as high as 67% at 789 nm.[147, 161] This makes SiNCs as a potential candidate for efficient EL in near infrared. As mentioned in Chapter 2, the performance of SiNC-OLEDs has not been fully characterized and operation mechanism of SiNC-OLED was still unclear. Therefore, in this chapter, we established a prototype SiNC-OLED system and demonstrated the device external quantum efficiency of 0.6% at a wavelength of 868 nm. In addition, the morphological surface study at the interface between SiNCs and bottom transport organic material suggests that complete coverage of the SiNCs on the conjugated polymer hole-transporting layer is required to observe efficient EL. Finally, an operational mechanism was proposed for the hybrid SiNC-OLED sysetm. This chapter describes the first demonstration of efficient EL, originated from SiNCs, a result that is further enhanced in Chapter 4.

3.2 Device Design and Material Selection

Two types of devices have been used in hybrid NC-OLEDs, the host-guest emissive

layer architecture[129, 165] and the neat NC emissive layer architecture[14, 15, 125], as illustrated in Figure 3.1. The host-guest system is often fabricated by mixing a wide energy gap transport organic semiconductor (host) with the nanocrystals (guest). The neat NC emissive layer architecture does not mix the organic transport layers and the emissive inorganic NCs. The host-guest system is usually adopted when there is exciton energy transfer from the host to the guest: when the majority of excitons are excited on the host molecules, the excitons will be converted into the energy states of the guest materials through dipole-dipole interaction. As such, this energy delivery from host to guest allows most excitons to recombine within the nanocrystals. However, recent research tends to use neat NC emissive layer architecture in the device design to generate excitons either by energy transfer from the adjacent organic semiconductors to nanocrystals[15] or by direct charge injection into the nanocrystals.[161]
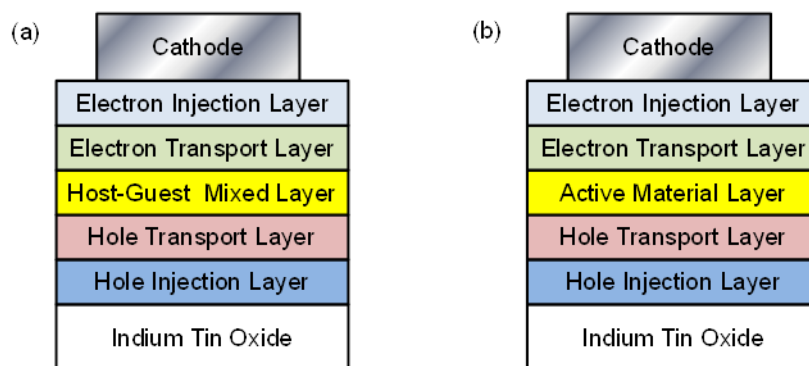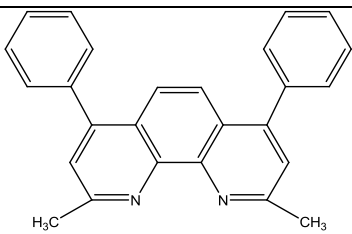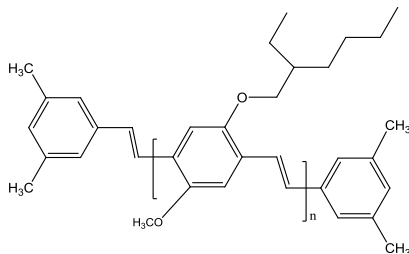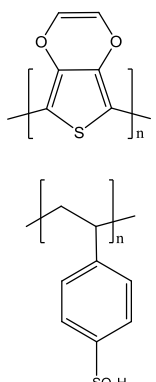
Figure 3.1 Device architectures for hybrid NC-OLEDs: (a) host-guest mixture and (b) and neat NC emissive layer.

The following sections of this chapter will illustrate the first demonstration of hybrid NC-OLEDs using colloidal SiNCs synthesized by a nonthermal plasma process. The conductive polymer poly(3,4-ethylenedioxythiophene):poly(styrenesulfonate)

(PEDOT:PSS) is selected for hole-injection layer in order to facilitate the hole injection process and also planarize the substrate surface. The hole-transporting polymer poly[2-methoxy-5-(2-ethylhexyl-oxy)1,4-phylene-vinylene] (MEH-PPV) is chosen due to the ease of processing and good hole conductivity. Organic molecule, bathocuproine (BCP), serves as electron transporting layer with deep HOMO level which can confine the hole charges within the SiNC layers. Table 3.1 summarizes the name and structure of the organic semiconductor polymers and small molecules used in this chapter.

Table 3.1 Summary of the name, structure and application of the organic semiconductors used in this chapter

Name	Structure	Full name	Application
BCP		Bathocuproine	Hole blocking layer in hybrid NC-OLEDs
MEH-PPV		Poly[2-methoxy-5-(2-ethylhexyl-oxy)-1,4-phylene-vinylene]	Host for SiNCs in hybrid NC-OLEDs
PEDOT:PSS		poly(3,4-ethylenedioxythiophene):poly(styrenesulfonate)	Hole injection layer for hybrid NC-OLEDs

3.3 Experimental Methods

In this work, NC-OLEDs are investigated using SiNCs synthesized by a non-thermal plasma process, followed by passivation in solution with an organic ligand of 1-dodecene.[164] In the reaction, silane in helium (5:95) and argon gases at 12-14 and 25-30 sccm respectively, are injected into a 9.5 mm O.D. pyrex tube and are dissociated using 85-100 W of rf input power at a reactor pressure of 1.4 Torr. Nanocrystals are formed in the plasma and are collected at the exhaust of the reactor on a stainless steel mesh. Figure 3.2 (a) shows a transmission electron micrograph of the as-produced SiNCs, with an average particle diameter of ~5 nm. The standard deviation of the SiNC size distribution is typically ~10-15% of the average particle size.[164] The inset of Figure 3.2 (a) shows the corresponding electron diffraction pattern exhibiting the (111), (220) and (311) diffraction rings of diamond-structured silicon, which demonstrates that the SiNCs are in fact crystalline. Figure 3.2 (b) shows the thin film absorption and PL of the SiNCs on glass, and the thin film PL of the hole-transporting polymer poly[2-methoxy-5-(2-ethylhexyl-oxy)1,4-phylene-vinylene] (MEH-PPV) on glass. The SiNC thin film is excited at λ=405 nm, and the resulting PL is peaked in the infrared at λ~853 nm. The solution quantum yield of the SiNCs used in this work is (46±6)%. The peak emission wavelength observed in PL is consistent with a particle diameter of ~5 nm, confirming that quantum confinement is observed in these SiNCs.[166]
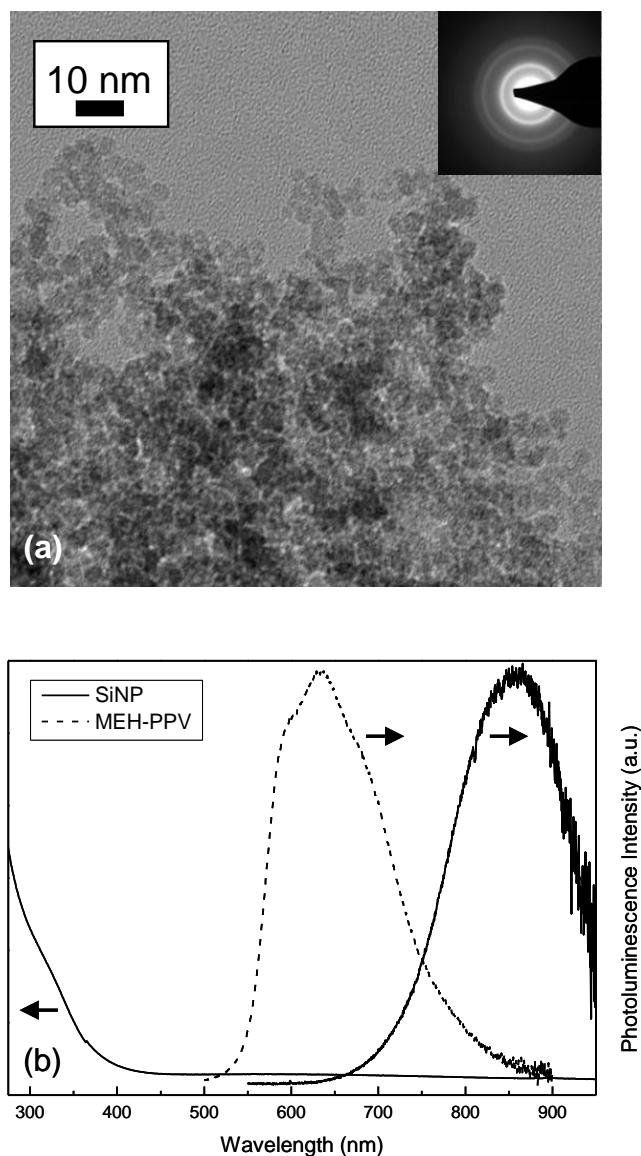
Figure 3.2 (a) Transmission electron micrograph of silicon nanocrystals (SiNCs) synthesized by a non-thermal plasma process. Inset: The corresponding electron diffraction pattern showing the (111), (220), and (311) diffraction rings of diamond-structured silicon. (b) Absorption and emission spectra for a SiNC thin film on glass. Also shown is the thin film photoluminescence of MEH-PPV on glass. In both cases the photoluminescence was collected under excitation at a wavelength of 405 nm.

Surface passivation of the SiNCs is performed by dispersing the particles in a mixture of mesitylene and 1-dodecene and boiling at 205°C for 2-3 hours under reflux conditions. The result is an ensemble of SiNCs which are surface-terminated with Si-C covalent

bonds. The chemically bonded passivation increases SiNC solubility in non-polar and organic solvents leading to stable colloids of individual, non-agglomerated SiNCs. The functionalization also reduces the tendency of SiNCs to oxidize. The resulting ligand length is estimated to be ~1.5 nm. Passivation leads to high PL quantum yields, and the quantum yield is drastically reduced in the absence of the passivating ligand.[147]

The device design in this work is based on neat NC emissive layer architecture, in which the emitting materials are located in between two organic charge transport materials (Figure 3.3). Devices were fabricated on indium-tin-oxide (ITO) coated glass substrates with a sheet resistance of 15 Ω/□. Substrates were degreased with solvents, followed by exposure to UV-ozone ambient. The device structure consists of a 43-nm-thick hole-injecting layer of PEDOT:PSS, followed by a 45-nm-thick hole-transporting layer of MEH-PPV. The 43-nm-thick layer of PEDOT:PSS was spun-cast at 3000 rpm for 30s, and was baked for 1.5 hours at 150°C. The MEH-PPV layer was spun-cast from a solution of chloroform (5 mg/mL) at 8000 rpm for 90s. The emissive layer of SiNCs was spun cast (2000 rpm, 90s) onto the MEH-PPV film from a solution of chloroform containing varying concentrations of 1-dodecene passivated SiNCs. The layers of MEH-PPV and SiNCs were each separately baked at 150°C for 1 hour. Also, device with mixture of MEH-PPV and different concentration of SiNC were spun-cast (3000rpm, 90sec) on PEDOT and baked for 1hr at 150 °C. A 30-nm-thick electron transporting layer of bathocuproine (BCP) was thermally evaporated onto the structure (<10⁻⁷ Torr), followed by a cathode consisting of a 0.5-nm-thick layer of LiF and a 50-nm-thick layer

45

of Al. All solution processed layers were spun-cast and baked in a N_2 glovebox. The thicknesses of the spun-cast layers were measured by atomic force microscopy (AFM).
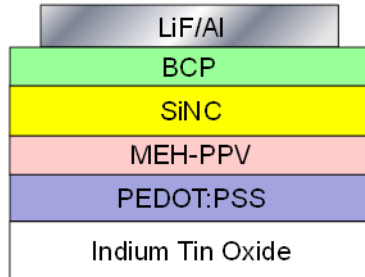
Figure 3.3 Device design for silicon nanocrystal organic light emitting device.

All measurements of optical response are unfiltered, and are made in the forward-emitted direction: The optical power was measured as the response to the increased voltage applied during the current-voltage characterization and the EL spectra were collected at the corresponding applied current. The geometry for the measurements of forward-emitted, device external quantum efficiency (η_{EQE}) is shown in Figure 3.4. Denoted in Figure 3.4 are the light-emitting device, a diaphragm which serves as a spacer, and a large-area photodetector (Hamamatsu, S3584-08). The relevant lateral dimensions are d_1=13 mm, d_2=1 mm, d_3=6 mm, and d_4=28 mm, which are the edge length of the device substrate, the diameter of a single light-emitting device, the size of the aperture in the diaphragm, and the edge length of the square large-area photodetector, respectively. Similarly, the relevant vertical dimensions are t_1=200 nm, t_2=1.1 mm, and t_3=0.2 mm, corresponding to the thickness of each component as shown in the figure. During device operation, forward-emitted photons are collected through the aperture in the diaphragm and measured as optical power by the large-area photodetector. The presence of the diaphragm prevents the collection of waveguided light emitted through

the edge of the device substrate. As is standard practice for devices with a broad emission spectrum, the responsively of the photodetector is taken as the average value of the electroluminescence wavelength weighted by the full emission spectrum of the device.
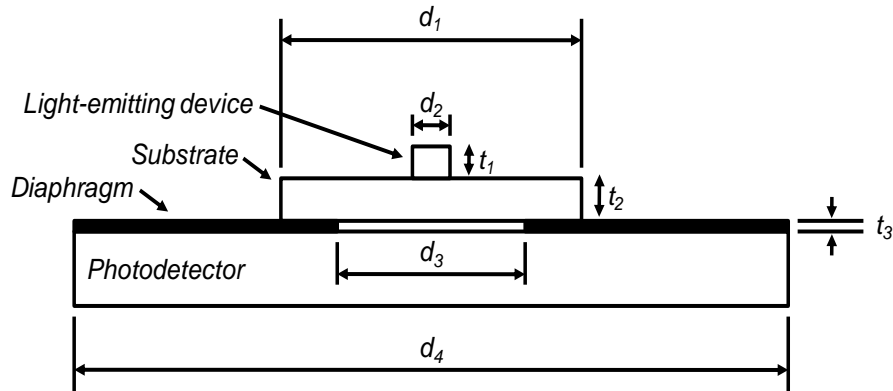
Figure 3.4 Arrangement for the measurement of light-emitting device opitcal power output and external quantum efficiency.

3.4 Emission Mechanism

The excitation of the nanocrystals in an NC-OLED can occur either by energy transfer from the neighboring polymer layer, or by charge carrier trapping and direct exciton formation.[14, 15, 85, 167] Energy transfer requires significant overlap between the fluorescence spectrum of the polymer (exciton donor) and the absorption spectrum of the nanocrystal (exciton acceptor).[24, 125, 168] In this work, non-radiative energy transfer is likely not responsible for the efficient EL since there is negligible overlap between the SiNC absorption spectrum and the normalized fluorescence of MEH-PPV (Figure 3.2 (b)). The lack of the necessary overlap suggests that the any observed EL is instead the result of carrier trapping directly on the nanocrystals.

3.5 Device Performance

3.5.1 Neat NC Emissive Layer Device Performance

Peak device performance was realized with an emissive layer spun-cast from a solution containing 20 mg/mL SiNCs. Figure 3.5 (a) shows the forward-emitted η_{EQE} measured as a function of the drive current density. A peak η_{EQE} of 0.6% is realized at a current density of 7 μA/cm^2.[169] The current-voltage and optical power-voltage characteristics for this device are shown in the Figure 3.5 (b). A maximum optical power output of ~85 μW/cm^2 is realized at a current density of ~400 mA/cm^2.
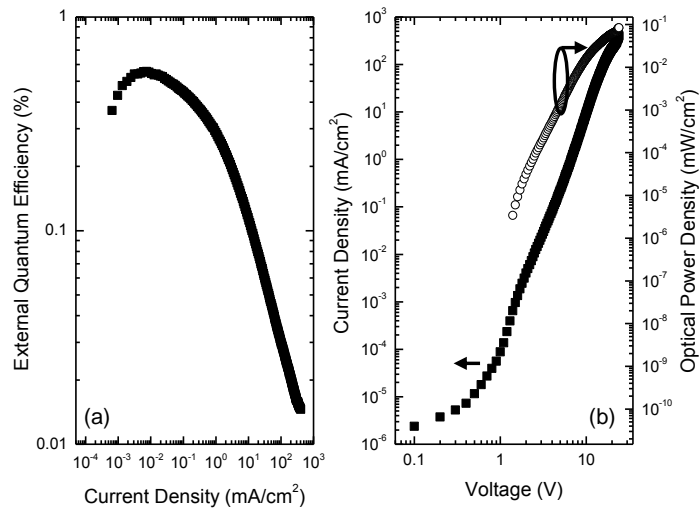
Figure 3.5 (a) External quantum efficiency for a nanocrystal-organic light-emitting device with an emissive layer spun-cast from a solution containing 20 mg/mL silicon nanocrystals. (b) Current-voltage (closed symbols) and optical power-voltage (open symbols) characteristics for the device in (a).

Figure 3.6 (a) shows EL spectra collected as a function of drive current density as well as a proposed energy level diagram (inset) under zero applied bias for the device of Figure 3.6 (a). The energy levels of PEDOT:PSS, MEH-PPV, and BCP were taken from literature.[170-172] The valence (VB) and conduction (CB) band energies for the SiNCs were

estimated by correcting those of bulk silicon for the quantum confinement effect. With

SiNC EL observed at $\lambda \sim 868$ nm (1.43 eV), the confinement energy is estimated to be

~0.3 eV. Of the total confinement energy, 0.2 eV is assigned to the VB, and 0.1 eV is

(a)

(b)
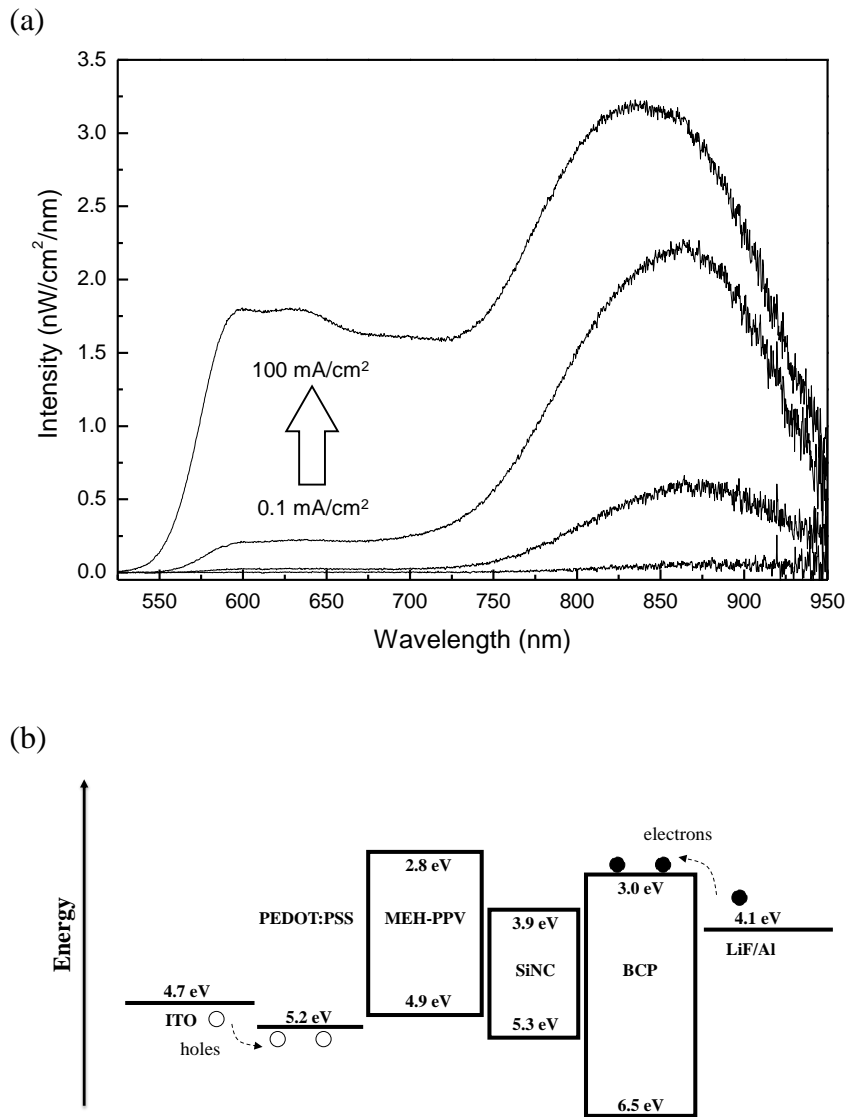
Figure 3.6 (a) Electroluminescence spectra for the device in Figure 3.5 at current densities of 0.1 mA/cm^{2}, 1 mA/cm^{2}, 10 mA/cm^{2}, and 100 mA/cm^{2}. (b) The proposed energy level diagram for the device under applied zero bias.

assigned to the CB, giving the energy levels shown in Figure 3.6.[173] For the proposed

device structure, both electrons and holes can be injected from the transport layers into

the SiNC layer.[174] Energy barriers at the MEH-PPV/SiNC and SiNC/BCP interfaces

confine injected electrons and holes to the SiNCs, respectively. Electroluminescence

spectra show SiNC emission at $\lambda \sim 868$ nm, red-shifted from the peak observed in thin

film PL. This difference in emission wavelength is likely the result of SiNC exposure to

air prior to the PL measurement. At low current densities, the SiNC emission peak is

observed at $\lambda \sim 868$ nm, with SiNC emission dominating the EL. Only at elevated current

densities (100 mA/cm^2) is the EL from MEH-PPV ($\lambda = 600$ nm) comparable to that

originating from the SiNCs. Electroluminescence from MEH-PPV is likely the result of

poor charge confinement and electron-hole charge balance under high excitation, which

may widen or shift the exciton recombination zone toward the MEH-PPV layer. The

observed emission from MEH-PPV is consistent with the thin film PL (Figure 3.2 (b)),

and with previous reports of EL using similar processing conditions.[175, 176]

3.5.2 Mixed-Layer Device Performance

For comparison to devices of neat NC emissive layer architecture, devices were also

constructed with MEH-PPV-SiNC mixture (host-guest device archetecture). Figure 3.7

(a) illustrates the device EL with the mixture of MEH-PPV (5 mg/mL) and SiNCs (20

mg/mL). The EL intensity decreases when the applied current density is >2 mA/cm^2. The

corresponding device shows poor performance in current density-voltage response and a

large turn-on voltage of 10.4 V as shown in Figure 3.7 (b) and (c). Here, the turn-on

voltage is defined as the voltage leading to an optical power density of 5 nW/cm^2. Compared to the neat NC emissive layer architecture, the mixed structure generally shows much lower efficiencies with a maximum external quantum efficiency only achieving ~ 0.03% at 1.1 mA/cm^2. Such poor device performance could be rationalized by two reasons. First, the mixture layer thickness was not optimized. Second, less charge could be injected into SiNCs embedded in the mixture layer due to the direct current path between BCP and MEH-PPV, which is supported by the observation of MEH-PPV emission in the following EL performance test (Figure 3.8). In addition, poor device yield is observed, which is likely due to the surface non-uniformity of the mixture-layer.

The EL performance of mixed-layer devices was studied as a function of the weight concentration ratio of SiNCs to MEH-PPV, including 4:1, 2:1, 1:1, and 1:5. In this study, the MEH-PPV weight concentration is fixed as 5 mg/mL for consistency and only the concentration of SiNC solution is varied. In all the cases, the EL from the mixed-layer structure shows lower intensity than neat NC emissive layer architecture devices under the same applied current density. Notably, emission from MEH-PPV usually appears in the EL spectrum even under low applied current density (Figure 3.8). This could originate from the following two reasons. First, since both MEH-PPV and SiNCs are adjacent to the ETL (BCP) layer, electron injection into both MEH-PPV and SiNCs could happen simultaneously, followed by direct electron-hole recombination at both materials. This could be further manifested by the extreme case when the devices are made with solution of low SiNC concentration (such as 1mg/mL), in which the host molecule MEH-PPV dominates the EL spectrum (at 600nm). However, as the concentration of SiNCs

increases, the emission from SiNCs could be favorable or even dominant if the number of

SiNCs largely outweighs that of MEH-PPV.
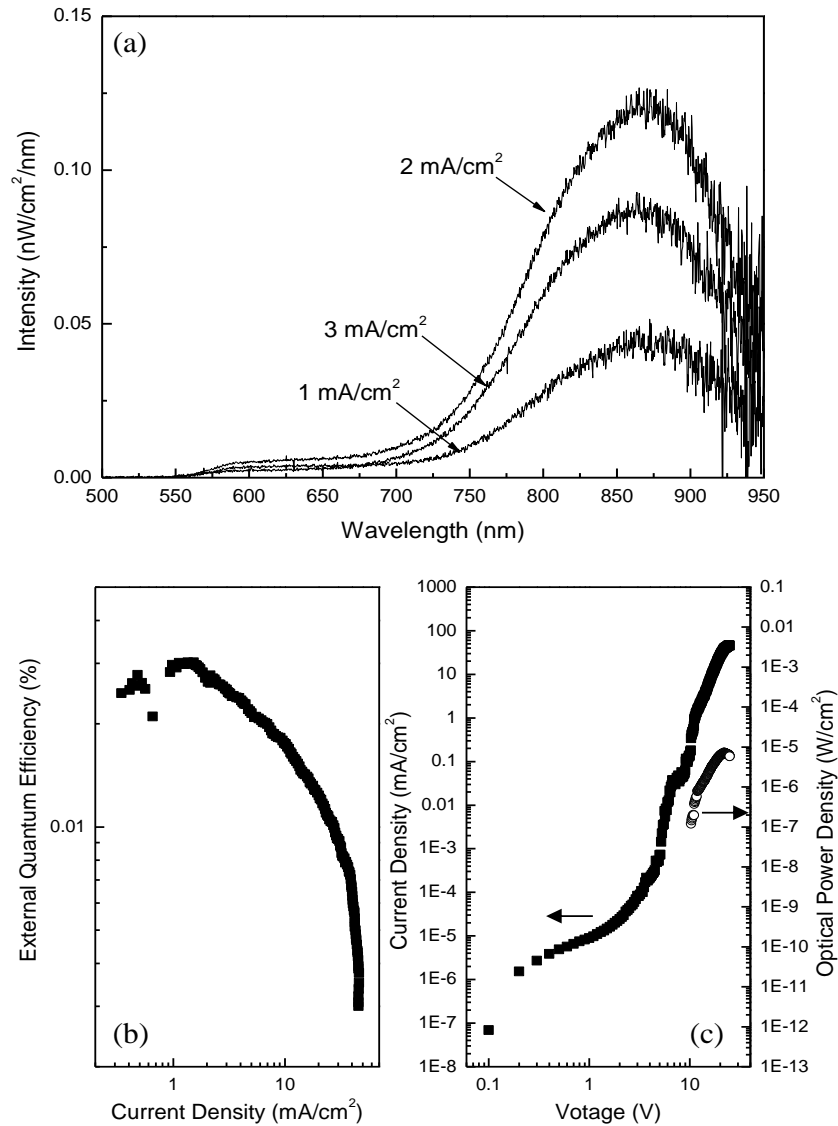
Figure 3.7 (a) Electroluminescence of mixture device with 20 mg/mL SiNC and 5 mg/mL MEH-PPV as a function of applied current density, (b) External quantum efficiency and (c) current-voltage (closed symbols) and optical power-voltage (open symbols) characteristics for the device in (a).
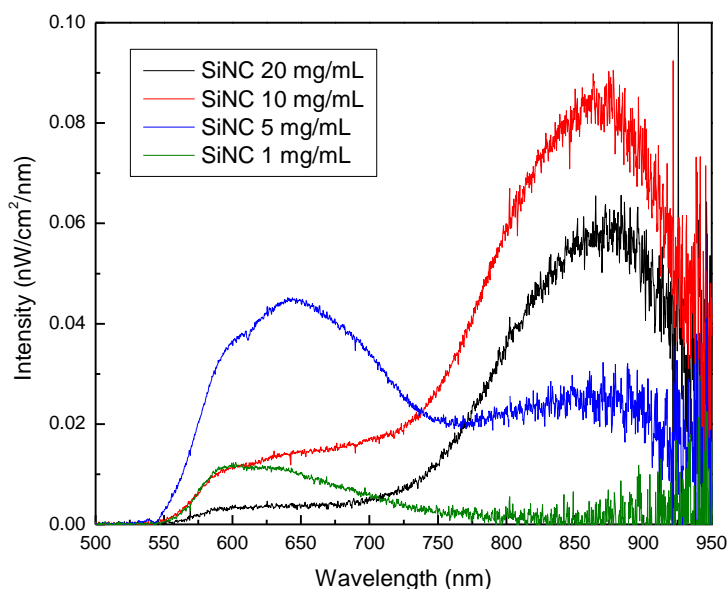
Figure 3.8 Electroluminescence of mixture devices made with solution containing different SiNC (guest) concentration (20, 10, 5, and 1 mg/mL). The MEH-PPV (host) concentration is fixed as 5 mg/mL. The applied current density is 1 mA/cm^2 for the case of 20, 10, and 1 mg/mL; 5 mA/cm^2 for the case of 5 mg/mL.

3.6 Device Optimization

Since neat NC emissive layer architecture shows better device efficiency, the performance of devices adopting this structure was further investigated as a function of SiNC solution concentration, ranging from 1 mg/mL to 20 mg/mL. Obvious changes are observed in both the current-voltage response (Figure 3.9 (a)) as well as device EL (Figure 3.9 (b)). As the SiNC solution concentration is increased, a corresponding decrease in current and increase in drive voltage is observed, suggesting that the devices become more resistive upon the addition of the SiNCs. Figure 3.9 (b) shows NC-OLED EL spectra as a function of SiNC concentration at a current density of 10 mA/cm^2. As the

concentration is increased, emission from the SiNCs increases and emission from the MEH-PPV is suppressed. In particular, for films spun-cast from a solution of 1 mg/mL, emission from MEH-PPV dominates the spectrum, while for films spun-cast from a solution of 20 mg/mL, emission from the SiNCs dominates the spectrum. This variation may originate from a non-uniform coverage of SiNCs on the polymer film[128, 174], leading to a leaking of electrons into the MEH-PPV layer, or might reflect a non-uniformity in the SiNC layer thickness, leading to a varying degree of charge and exciton confinement in the emissive layer.
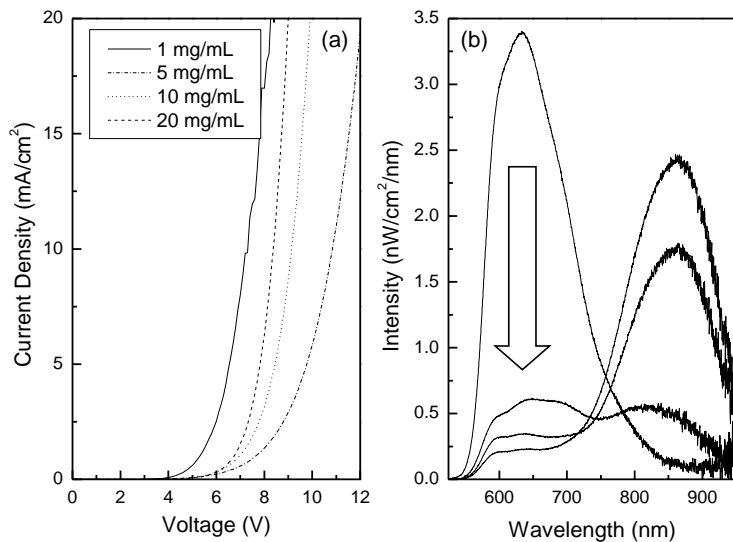
Figure 3.9 (a) Current-voltage characteristics for nanocrystal-organic light-emitting devices having emissive layers spun-cast from solutions with varying silicon nanocrystal concentration. (b) Electroluminescence spectra for the devices in (a) at an applied current density of 10 mA/cm^2. The arrow denotes the direction of increasing concentration.

3.7 Role of Coverage and Thickness of SiNC Layer in Device Performance

In order to clarify the role of surface coverage and emissive layer thickness in determining the concentration dependence observed in Figure 3.9, Atomic Force Microscopy (AFM) was used to investigate the surface morphology of the SiNCs deposited on top of MEH-PPV films. The radius of curvature of the AFM tip is <10 nm.[177] The structure investigated by AFM is identical to that described in Figure 3.9 with the omission of the BCP and cathode layers. Figure 3.10 shows tapping-mode AFM phase images of the films as a function of SiNC solution concentration. In Figure 3.10 (a), the film made from a solution of 1 mg/mL SiNCs shows incomplete surface coverage of SiNCs, with the bright regions corresponding to the SiNCs, and the dark regions corresponding to the MEH-PPV. In a device, this incomplete coverage of SiNCs could provide a path for electron injection from BCP to MEH-PPV, leading to exciton formation directly on the MEH-PPV layer. This scenario is consistent with observations of significant polymer emission in devices constructed using 1 mg/mL SiNC solutions. Films cast from a solution of 5 mg/mL (Figure 3.10 (b)) show improved SiNC coverage (bright regions), which could help block charge carriers and excitons from reaching the hole-transporting layer, suppressing EL from MEH-PPV and enhancing emission from the SiNCs. At higher concentrations the coverage does not change significantly (Figure 3.10 (c) and (d)), indicating that SiNC coverage may no longer drastically impact device performance. Instead, the thickness of the SiNC layer likely determines the fraction of charge carriers trapped in the emissive layer and the magnitude of the driving voltage.

The SiNC film thickness was also measured using AFM by creating a step in the film and measuring the height of the step. The thickness of the spun-cast SiNC layer increases from ~7 nm to ~80 nm, for increasing SiNC solution concentration from 1 mg/mL to 20 mg/mL, as indicated in Figure 3.10. This is consistent with the observed increase in device driving voltage at high concentration (Figure 3.9 (a)).
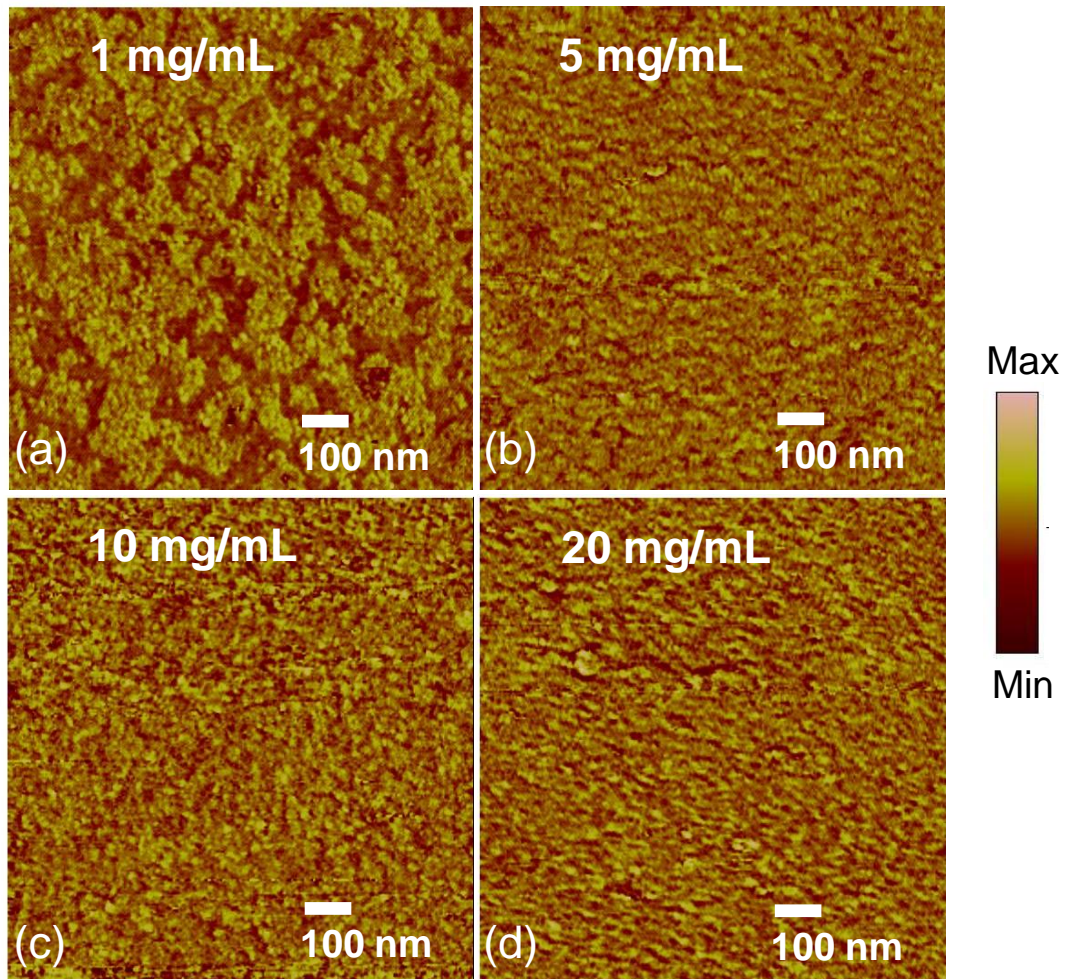
Figure 3.10 (a)-(d) Atomic force microscopy (AFM) phase images of silicon nanocrystal (SiNC) films spun-cast onto MEH-PPV from solutions with varying concentrations of SiNCs.

3.8 Discussion and Summary

Hybrid NC-OLEDs using crystalline SiNCs synthesized by a non-thermal plasma process have been demonstrated with EL at a wavelength of 868 nm. A high peak external quantum efficiency of ~0.6% is obtained in the forward-emitted direction, with the EL originating primarily from the SiNCs up to a current density of 10 mA/cm^2. Excitation of the SiNCs is by direct charge trapping and exciton formation. A strong dependence of EL performance on SiNC layer coverage and thickness has been investigated for better charge confinement within SiNC materials and improved device efficiency.

Although the demonstration of near-infrared EL from SiNCs is promising for the potential application of group IV material in hybrid NC-OLEDs, the important key for realizing the next-generation hybrid NC-OLEDs lies in comparable high device performance with OLED technology. The poor performance of less than 1% in the device containing MEH-PPV/SiNCs could be from the re-dissolving of HTL into SiNCs, which possibly introduces electron injection into MEH-PPV layer. This could lead to widen or shift the exciton recombination zone from SiNCs toward MEH-PPV layer charge, and less charge confinement within SiNCs. In addition, the relatively lower LUMO level of MEH-PPV could allow electrons to overcome the energy barrier between the conduction band edge of SiNCs (1.1 eV) and the LUMO of MEH-PPV (2.8 eV), under higher applied current density, followed by exciton formation and recombination within MEH-PPV. The device efficiency could be further enhanced by selecting better hole transport layer to eliminate the re-dissolving issue between layer interfaces, and by creating higher

energy barrier for charge and exciton confinement within SiNC materials. Such improvement will be discussed in the following chapter.

Chapter 4 Highly Efficient Silicon Nanocrystal Light-Emitting Devices

(This work was previously published in: "Cheng, K., Anthony, R., Kortshagen, U. R. & Holmes, R. J. High-Efficiency Silicon Nanocrystal Light-Emitting Devices. *Nano Lett.* **11**, 1952-1956 (2011)". Copyright 2011 American Chemical Society)

4.1 Overview

In Chapter 3, EL from SiNCs was studied by hybrid NC-OLEDs with neat NC emissive layer architecture design. Such device architecture opened an opportunity for understanding device emission mechanism and identifying the potential bottleneck for further improvement of the device efficiency. In this chapter, a breakthrough is achieved for highly efficient SiNC electroluminescence with more carefully-designed neat NC emissive layer architecture. In such structurally optimized nanocrystal-organic light emitting devices (NC-OLEDs), peak external quantum efficiencies of up to 8.6% are realized, with emission originating solely from the SiNCs. The high efficiencies reported here demonstrate for the first time that, with an appropriate choice of device architecture, it is possible to achieve highly efficient electroluminescence from nanocrystals of an indirect band-gap semiconductor.

4.2 Device Design and Materials Selection

In Chapter 3, a prototype SiNC-OLED was demonstrated with a neat NC emissive layer architecture. One limitation of the in Chapter 3 on these devices has been the use of

59

non-orthogonal solvents for the nanocrystals and polymer transport layers, which leads to the re-dissolving of bottom polymer layer (HTL). The previously observed low efficiencies for silicon NC-OLEDs could also reflect inefficient charge carrier injection and confinement in the SiNC layer.[126, 178]

In order to achieve high efficiency, the devices discussed in this chapter were constructed with a new HTL material. The device still adopts a neat NC emissive layer architecture due to its better charge confinement as reported in chapter 3. The device structure is shown in Figure 4.1. It is important to note that in this work, a polymer poly(N,N'-bis(4-butylphenyl)-N,N'-bis(phenyl)benzidine (poly-TPD) is selected as the hole transport layer (HTL) due to its large energy gap and ability to be cross-linked. This layer replaces the MEH-PPV HTL which locates in between the emissive layer (SiNC) and the hole injection layer (PEDOT:PSS) of devices as discussed in Chapter 3. (Figure 4.1) The crosslinkable polymer successfully eliminates the parasitic EL from the HTL by preventing the re-dissolving of HTL into the top SiNC layer during the solution processing. In addition, in order to achieve better charge confinement within SiNCs, various electron transport materials with wide energy band-gap were chosen for the electron transport layer (ETL), which locates between the SiNC layer and the cathode layer. The use of optimized, wide energy gap HTL and ETL materials creates a double heterostructure that ensures the confinement of both charge carriers and excitons to the nanocrystal emissive layer. Consequently, a drastic improvement in the NC-OLED efficiency is achieved. By adopting this system, we demonstrate η_{EQE} values that to our knowledge are much larger than any previously reported NC-OLED systems. High

efficiency is observed for SiNCs of varying sizes at EL wavelengths ranging from the red to the infrared. Moreover, while in most previous studies the organic transport layers are chosen to have the largest possible charge carrier mobility, we demonstrate here that although the mobility is important for low voltage operation, it is more critical to engineer a device architecture that permits effective charge and exciton confinement in the nanocrystal layer.
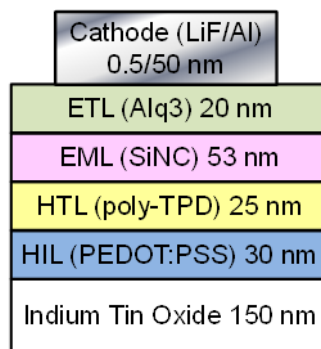
Figure 4.1 Neat NC emissive layer architecture design used in this chapter. The device contains indium tin oxide (ITO) as an anode. The hole-injection, hole-transport, and emissive-mater layers were fabricated through solution processing. The electron transport layer and device cathode were deposited by thermal evaporation.

4.3 Experimental Methods

The SiNCs used in this study are synthesized using a non-thermal plasma route.[164] In order to realize different emission wavelengthes, the nanocrystals with diameters of 5 nm and 3 nm are selected. The size effect on quantum confinement can lead to corresponding peak emission wavelengths of 853 nm and 777 nm (Figure 4.2). After the SiNC synthesis, the nanocrystal surfaces are functionalized with ligands of 1-dodecene, as it is reported that the passivation ligand could reduce the surface quenching state and thus

permits higher material photoluminescence performance. In this study, SiNCs after passivation demonstrated ensemble η_{PL} values of 45% and 43%, for 5-nm and 3-nm SiNCs, respectively.
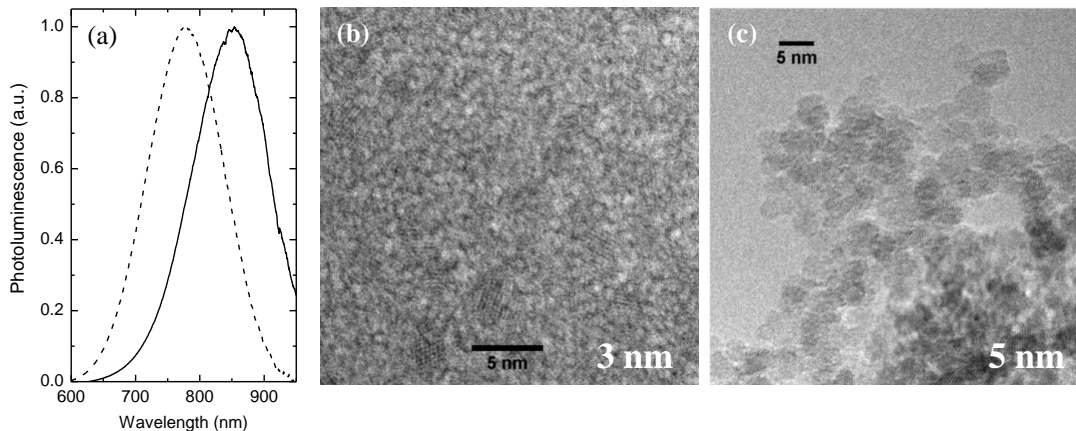
Figure 4.2 Nanocrystal photoluminescence and size. (a) Solution photoluminescence for silicon nanocrystals chemically passivated with ligands of 1-dodecene in the hydrosilylation solution of 1:5 1-dodecene:mesitylene. The diameters of the nanocrystals shown are 5 nm (solid line) and 3 nm (broken line), with peak emission wavelengths of 853 nm and 777 nm, respectively. For both spectra, the excitation wavelength is 395 nm. Transmission electron micrographs of silicon nanocrystals having diameters of (b) 3 nm and (c) 5 nm.
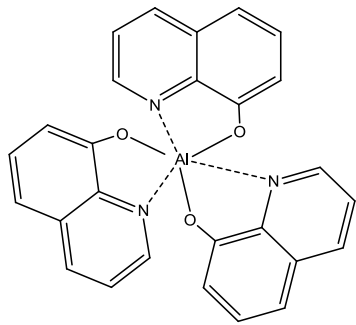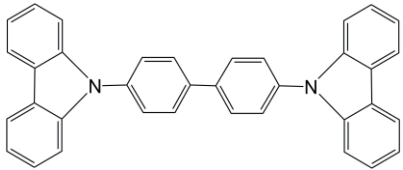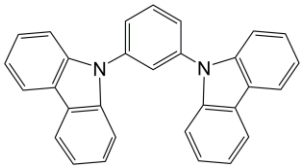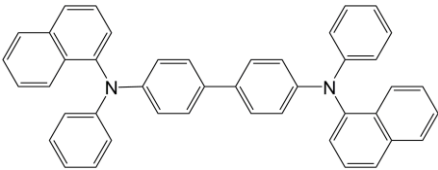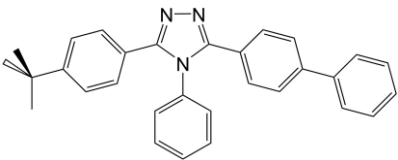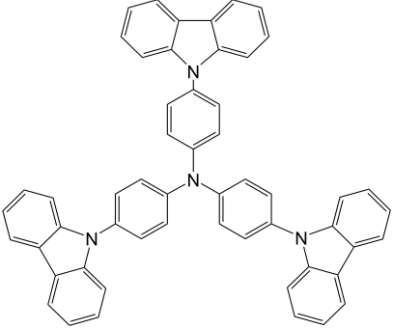
Devices were constructed on glass slides coated with a 150-nm-thick layer of indium-tin-oxide (ITO) which serves as a transparent anode. A 30-nm-thick layer of poly(3,4-ethylenedioxythiophene):poly(styrenesulfonate) (PEDOT:PSS) was spun-cast (3000 rpm, 30 seconds) onto the ITO as a hole-injection layer and was baked at 150°C for 90 minutes. A 25-nm-thick cross-linked poly-TPD layer was followed as a hole-transport layer (HTL). The poly-TPD was dissolved in chloroform (5 mg/mL) and cross-linked after spin-coating (8000 rpm, 90 seconds) by exposure to ultraviolet light (λ=254 nm, 1.7 mW/cm^2) for 80 minutes.[115, 179] The emissive layer consisted of a 53-nm-thick layer of

SiNCs was spun-cast from a solution of chloroform (20 mg/mL, 2000 rpm, 90 seconds) onto poly-TPD and was baked at 64°C for 1 hour. The emissive layer was capped with a 20-nm-thick ETL consisting of tris-(8-hydroxyquinolinato) aluminum (Alq_3), N,N'-dicarbazolyl-4-4'-biphenyl (CBP), or 4,4′,4″-tris-(N-carbazolyl)-triphenlyamine (TCTA) deposited by vacuum thermal sublimation. The device cathode consisted of a 0.5-nm-thick layer of LiF and a 50-nm-thick layer of Al. Devices were characterized in air ambient immediately after fabrication. Table 4.1 and 4.2 summarize all the name, structure and application of the chemicals used in this chapter.

Table 4.1 Summary of the name, structure and application of the organic polymer semiconductors used in this chapter.

Name	Structure	Full name	Application
Poly-TPD		poly(N,N'-bis(4-butylphenyl)-N,N'-bis(phenyl)benzidine	Hole transport layer for SiNCs in hybrid NC-OLEDs
PEDOT: PSS		poly(3,4-ethylenedioxythiophene):poly(styrenesulfonate)	Hole injection layer for hybrid NC-OLEDs

Table 4.2 Summary of the name, structure and application of the organic small-molecule semiconductors used in this chapter.

Name	Structure	Full name	Application
Alq$_3$		Tris-(8-hydroxyquinolinato) aluminum	Electron Transport layer in hybrid NC-OLEDs
CBP		4,4'-Bis(9-carbazolyl)-1,1'-biphenyl	Electron Transport layer in hybrid NC-OLEDs
mCP		1,3-Bis(carbazol-9-yl) benzene	Electron Transport layer in hybrid NC-OLEDs
NPB		N,N'-Bis(naphthalen-1-yl)-N,N'-bis(phenyl)-benzidene	Electron Transport layer in hybrid NC-OLEDs
TAZ		3-(Biphenyl-4-yl)-5-(4-*tert*-butylphenyl)-4-phenyl-4*H*-1,2,4-triazole	Electron Transport layer in hybrid NC-OLEDs
TCTA		Tris(4-carbazoyl-9-ylphenyl) amine	Electron Transport layer in hybrid NC-OLEDs

4.4　High Efficiency Silicon Nanoscrystal Light-Emitting Devices

The EL of devices constructed using both 5 nm and 3 nm diameter SiNCs was collected as a function of applied current density and is shown in Figure 4.3. Emission originating from the SiNCs is clearly observed, with no emission from the adjacent
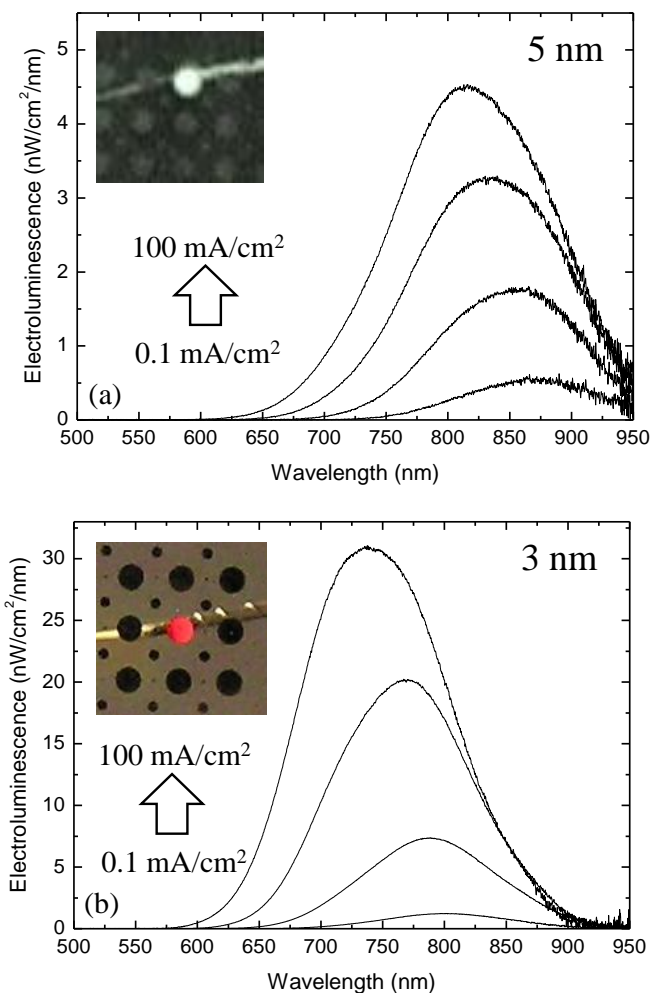
Figure 4.3 Performance of silicon nanocrystal-organic light-emitting devices (NC-OLEDs). Electroluminescence (EL) of NC-OLEDs using nanocrystals with a diameter of (a) 5 nm and (b) 3 nm as a function of increasing applied current density (0.1 mA/cm^2, 1 mA/cm^2, 10 mA/cm^2, 100 mA/cm^2). Photographs are taken through the ITO anode and show an array of devices from which one is energized and exhibiting EL. The applied current density is 100 mA/cm^2 in (a) and 10 mA/cm^2 in (b). A night-vision sensitive camera was used to photograph devices based on the 5 nm silicon nanocrystals.

65

transport layers. The lack of transport layer emission confirms that charge carriers and excitons are well-confined to the emissive layer. The inset of the photographs captured the light emission during the device operation at 100 mA/cm^2 in (a) and 10 mA/cm^2 in (b), conducted by the night-vision sensitive camera (for near infrared emission) and the commercialized camera (for red emission).

Interestingly, as shown in Figure 4.3, a blue-shift of the electroluminescence peak is observed with increasing applied current density. This spectral change is reversible with current density, and may reflect the size dispersion of the SiNCs and the as resulted variation of the charge injection and PL efficiency. As the applied field increases, it is also likely to excite the smaller nanocrystals which have larger energy band gap. Figure 4.4 summarizes the emission peak shift as a function of applied current density and
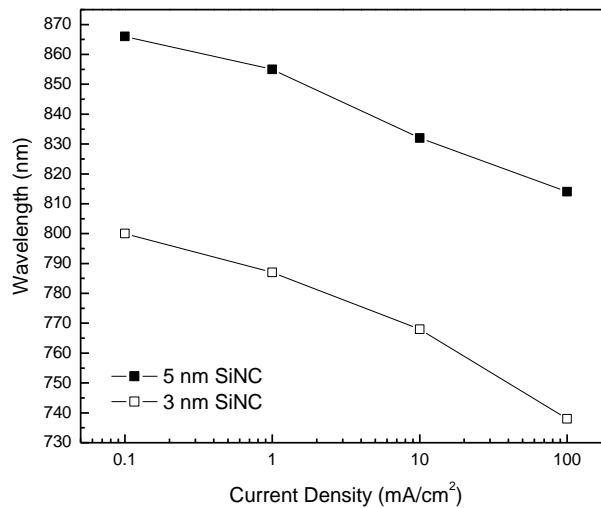
Figure 4.4 Blue shift of peak electroluminescence from SiNC-OLEDs as a function of current density and as a function of different size of SiNCs (5 nm and 3 nm).

Figure 4.5 shows the reversible spectrum during the device operation. Note that in Figure 4.5, the order of the color (black, red, blue, olive, and magenta) represents the sequence

of increased or decreased applied current density. Similar blue shift of the emission peak under increased applied field has also been observed in inorganic light-emitting device systems.[180, 181] The reversible spectrum also suggests that severe SiNC-surface oxidation during device operation is unlikely. If surface oxidation did occur, the size of the nanocrystals would be decreased permanently and the corresponding emission would be no longer reversible.

Figures 4.6 shows the device performance for NC-OLEDs based on SiNCs of varying size and PL efficiency, whose corresponding EL is shown in Figure 4.3. A peak η_{EQE} of 8.6% is realized for devices containing SiNCs that are 5 nm in diameter, and the efficiency remains >4% up to a current density of ~0.2 mA/cm^2. These devices exhibit a turn-on voltage of ~1.55 V, and a peak optical power output of 0.13 mW/cm^2, as shown in Figure 4.7. Here, the turn-on voltage is defined as the voltage leading to an optical power output of ~5 nW/cm^2. Devices constructed using SiNCs that are 3 nm in diameter show a peak η_{EQE} of 6.7%, and the efficiency remains >4% to a current density of 0.3 mA/cm^2. These devices show a turn-on voltage of ~2.30 V, and a peak optical power output of 0.27 mW/cm^2.

4.5   Role of ETL in Device Performance

In previous NC-OLED works, the rule of selecting organic transport materials with highest charge mobility for efficient NC-OLEDs has been proposed.[126] In this work, in order to investigate how the choice of transport layer impacts device efficiency, device performance of NC-OLEDs was examined as a function of ETL material. In order to
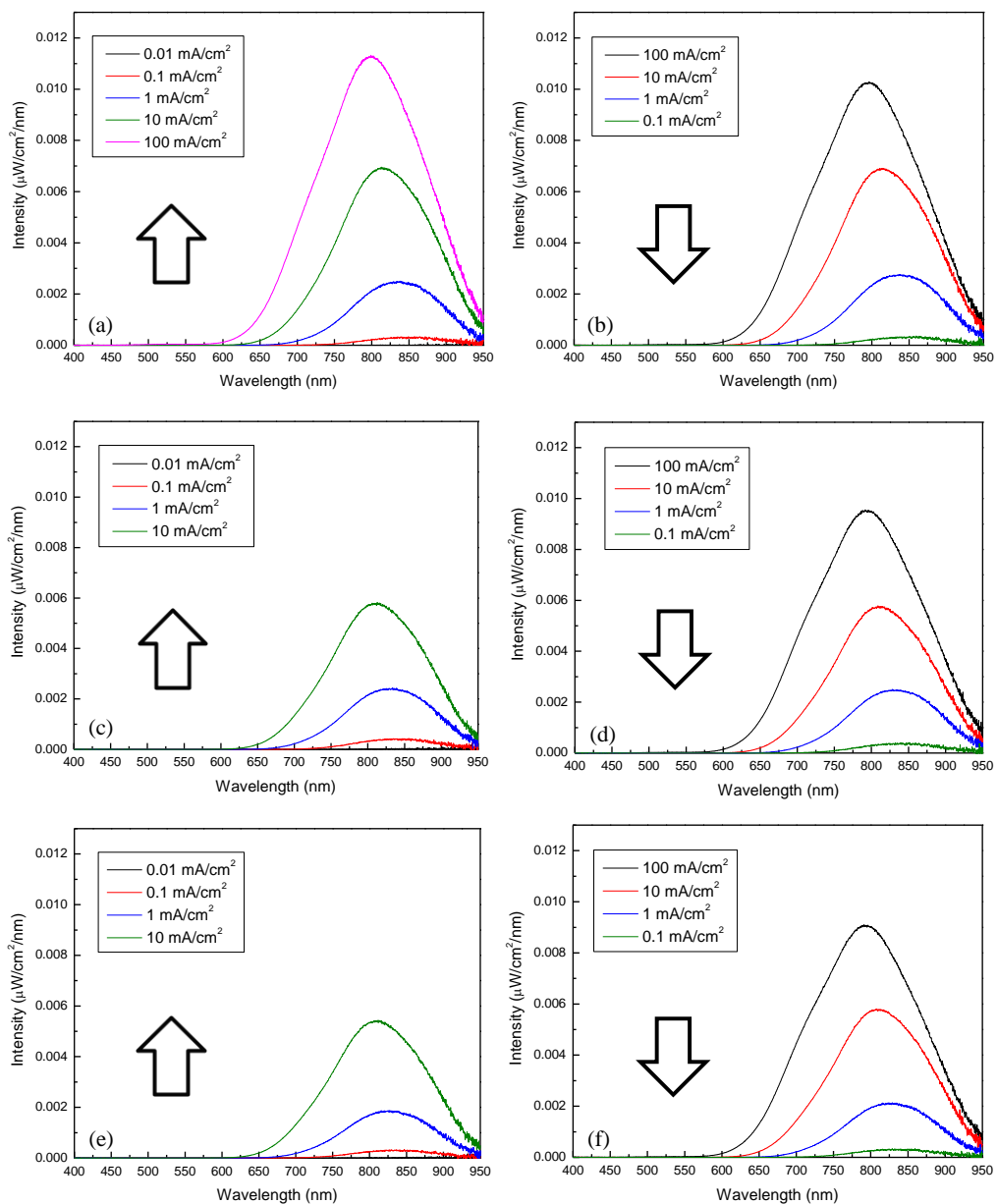
Figure 4.5 (a)-(f) Reversible peak electroluminescence of 5-nm SiNCs under continuous cycled applied current densities. Note that the order of color (black, red, blue, olive, magenta) in the figures represents the sequence of increased or decreased current densities and the direction of the arrows means the sequence of the applied current densities.
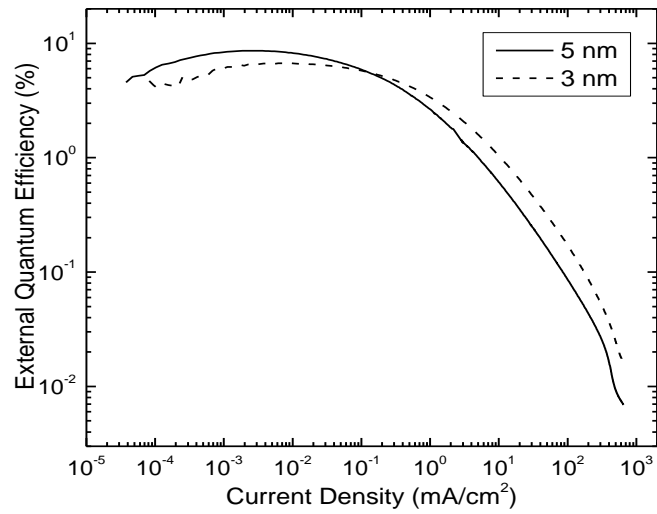
Figure 4.6 External quantum efficiency characteristics for NC-OLEDs using silicon nanocrystals with a diameter of either 5 nm (solid lines) or 3 nm (broken lines).
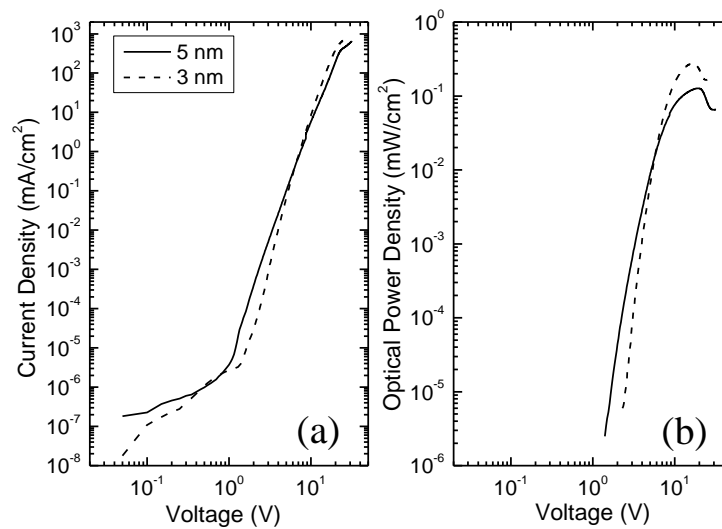
Figure 4.7 Current density-voltage (a) and optical power density-voltage (b) characteristics for NC-OLEDs using silicon nanocrystals with a diameter of either 5 nm (solid lines) or 3 nm (broken lines).

determine the role of the electron mobility in device performance, thermally evaporated layers of either TCTA or CBP were chosen for comparison with Alq3. Typically used as an HTL in organic light-emitting devices, TCTA has a very low electron mobility $<10^{-8}$ cm^2/Vs [179, 182] and hence offers a useful contrast to Alq3 ($\sim10^{-6}$ cm^2/Vs at 0.4 MV/cm).[183] In comparison, CBP has an electron mobility of $\sim3\times10^{-4}$ cm^2/Vs at 0.5 MV/cm, two orders of magnitude larger than that of Alq3.[182, 184] Energy levels for the corresponding device architectures are shown in Figure 4.8 (a). The highest occupied molecular orbital (HOMO) energy levels of the transport layers were taken from literature[172, 185], while the lowest unoccupied molecular orbital (LUMO) energy levels were estimated using the optical absorption edge. The HOMO and LUMO levels of poly-TPD were estimated from cyclic voltammetry measurements.[186] For the SiNC layer, the valence and conduction band energies were estimated by correcting those of bulk silicon for the quantum confinement effect.[173] The large energy gap and deep HOMO level of each ETL material helps to confine excitons and holes to the emissive layer.

Figures 4.8 (b) and (c) compare the performance of 5-nm SiNCs OLED using Alq3, TCTA, or CBP as the ETL material. Surprisingly, replacing Alq3 with TCTA does not substantially reduce the efficiency, with the TCTA device showing a peak efficiency of 7.6%. The dependence of the optical power density on voltage shows a similar brightness level when using both ETL materials, with the TCTA device characterized by a larger turn-on voltage of 2.05 V. A similar dependence is also observed for the dependence of device current on voltage, with the TCTA device again showing a slight reduction in current and a larger driving voltage. The increased voltage observed in devices with

TCTA as an ETL likely reflects its lower electron mobility relative to Alq$_3$. Nevertheless, the ability to realize efficient EL from NC-OLEDs with an ETL consisting of low mobility TCTA suggests that for a 20-nm-thick film, the electron mobility does not predominantly determine the device performance.
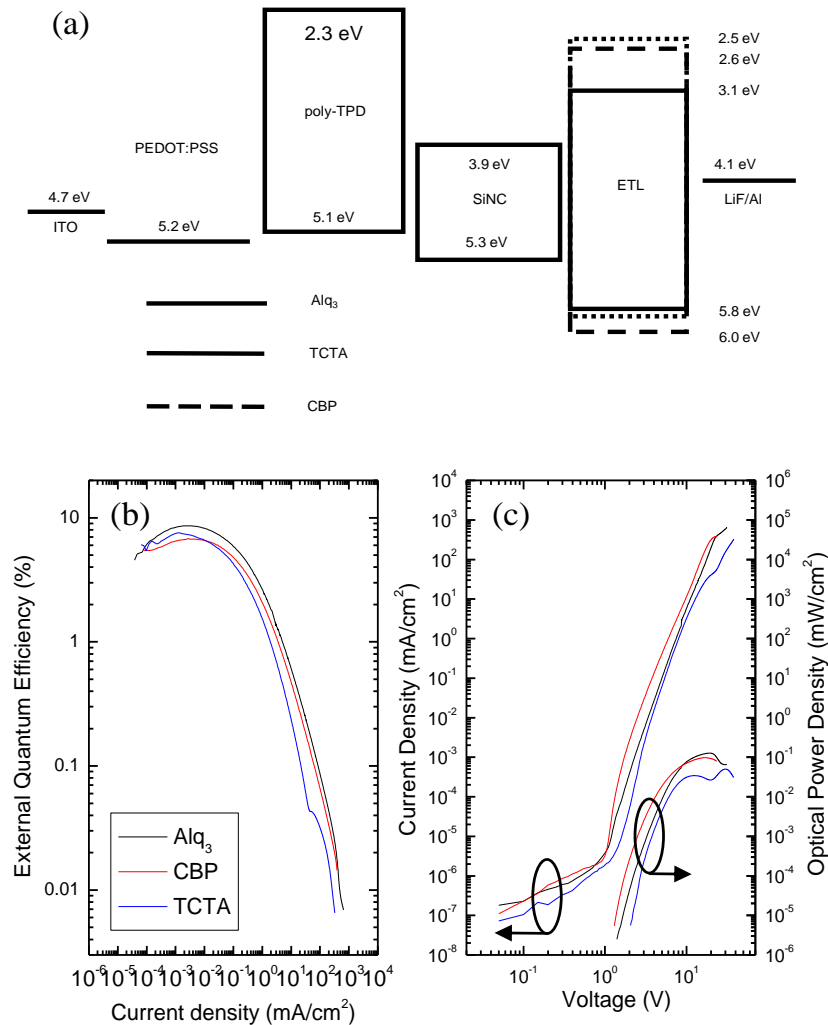
Figure 4.8 Impact of the electron-transporting material: (a) Proposed energy level diagram under zero applied bias for devices containing silicon nanocrystals with a diameter of 5 nm, and an electron-transporting layer consisting of either Alq$_3$, TCTA, or CBP. (b) External quantum efficiency versus current density for devices containing either Alq$_3$ (solid line), TCTA (broken line), or CBP (dotted line). (c) Current density-voltage and optical power density-voltage characteristics for the devices in (b).

When CBP is used as an ETL, good device performance is also observed, with a peak efficiency of 6.8%. The turn-on voltage for CBP-based devices (~1.30 V) is comparable to that of devices with an ETL of Alq_3. Here, the high mobility of CBP permits the realization of low-voltage operation but the device efficiency does not see an increase compared to Alq_3 Similar results are also obtained for a variety of other ETL materials or combination of ETL and HTL, the performance of these additional device architectures and the electron mobility of the applied ETLs are tabulated in Table 4.3.[179, 182-184, 187, 188] The capping layers for efficient SiNC-OLEDs could be 1,3-Bis(carbazol-9-yl) benzene (mCP), 3-(Biphenyl-4-yl)-5-(4-*tert*-butylphenyl)-4-phenyl-4*H*-1,2,4-triazole (TAZ), or the combination of ETL and HTL materials, such as Alq_3 and N,N'-Bis(naphthalen-1-yl)-N,N'-bis(phenyl)-benzidene (NPB). This phenomenon illustrates the flexibility of device design with various capping ETL layer with wide range of bulk electron mobility. Such results suggest that the electron mobility of thin ETL does not have a strong impact on the device efficiency. Instead, the existence of ETL on SiNC layer serves as a hole-confinement layer with a protection function from cathode quenching.

Table 4.3 Summary of the silicon NC-OLEDs with various ETL.

ETL (Thickness)	Electron Mobility (cm^2/Vs)	Peak η_{EQE}
Alq₃ (20 nm) [aluminum tris(8-hydroxyquinolinato)]	$\sim 10^{-6}$ at 0.4 MV/cm	8.6% at 3 $\mu A/cm^2$
CBP (20 nm) [4,4'-Bis(*N*-carbazolyl)-1,1'-biphenyl]	$\sim 3 \times 10^{-4}$ at 0.5 MV/cm	6.8% at 3 $\mu A/cm^2$
mCP (20 nm) [1,3-Bis(carbazol-9-yl) benzene]	$\sim 3 \times 10^{-4}$ at 0.25 MV/cm	5.7% at 3 $\mu A/cm^2$
TAZ (20 nm) [3-(Biphenyl-4-yl)-5-(4-*tert*-butylphenyl)-4-phenyl-4*H*-1,2,4-triazole]	$\sim 10^{-6}$ at 0.49 MV/cm	3.5% at 0.5 $\mu A/cm^2$
TCTA (20 nm) [tris(4-carbazoyl-9-ylphenyl) amine]	$< 10^{-8}$	7.6% at 1 $\mu A/cm^2$
Alq₃/NPB (2 nm/18 nm) Alq₃/[N,N'-Bis(naphthalene-1-yl)-N,N'-bis(phenyl)-benzidene]	-	7.4% at 2 $\mu A/cm^2$

It is interesting that highly efficient devices can be fabricated using materials with electron mobilities of such a wide range. This suggests that what is most crucial to high efficiency is the presence of a wide energy gap blocking layer to confine charges and excitons within the nanocrystal layer and to separate the emissive layer from the quenching metallic cathode. This is further evidenced by the fact that for devices with no ETL as shown in Figure 4.9, the efficiency drops to 4.4%, almost a 50% reduction from what is attainable with appropriate choice of ETL. It is also worth noting that even in an unoptimized device architecture (i.e. no ETL), the SiNCs show performance exceeding that of state-of-the-art NC-OLEDs based on II-VI or IV-VI semiconductor nanocrystals.
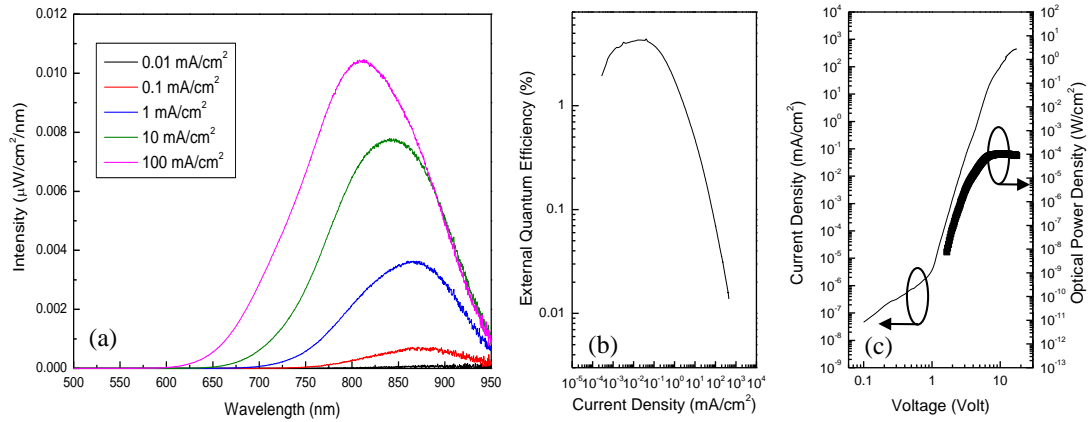
Figure 4.9 Silicon NC-OLEDs with no electron transport layer: (a) electroluminescence, (b) external efficiency, (c) current density-voltage and optical power density characteristics.

While the aforementioned discussion suggests that low electron mobility materials may be used in NC-OLEDs with optimized charge blocking barriers, it does not remove the importance of this parameter. In fact, when the thickness of the ETL is increased to 40 nm, the low electron mobility of TCTA becomes problematic, reducing the efficiency of the NC-OLED by more than one order of magnitude. (Figure 4.10) For NC-OLEDs containing an ETL of Alq_3, no such significant reduction in performance is observed upon increasing the thickness. All device performance is summarized in Figure 4.11. As such, the use of high mobility materials is still preferred as it permits the realization of relatively low voltage and ensures high efficiency especially in NC-OLEDs with thick ETL. The high efficiency obtained with TCTA suggests that low mobility materials may also be utilized if the layer thicknesses are kept thin, and electron-hole confinement in the nanocrystal layer is optimized.
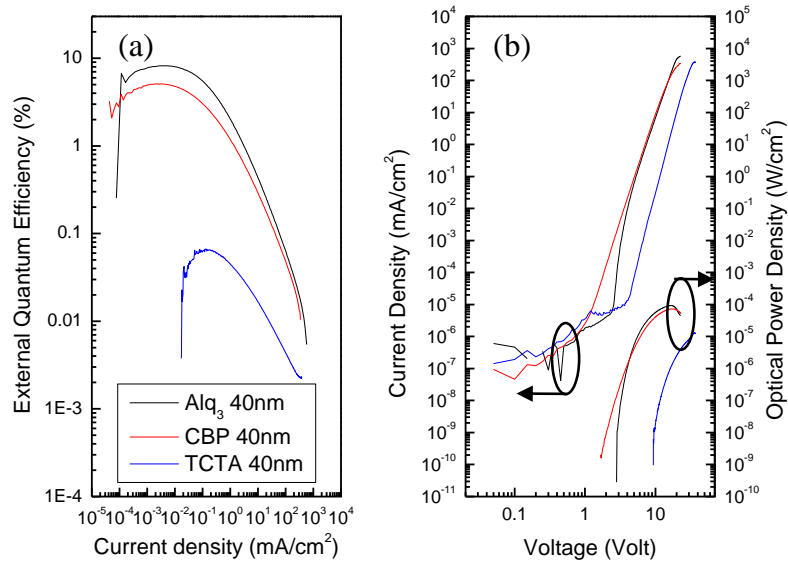
Figure 4.10 Silicon NC-OLED with different 40-nm electron transport layer: (a) external quantum efficiency, (b) current density-voltage and optical power density characteristics.
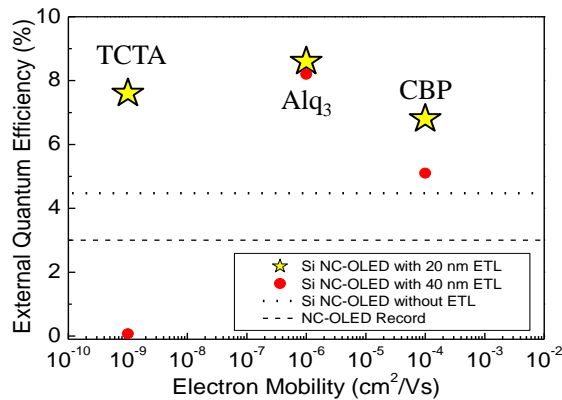
Figure 4.11 Summary of the device efficiency with different electron transport layer as a function of thickness.

4.6 Role of SiNC Thickness

As discussed in Chapter 3, the thickness and coverage of SiNC layer are critical to the effective confinement of excitons and charges within the active materials, i.e., SiNC. The thickness effect of SiNC layer was investigated by fabricating hybrid devices with SiNC

solutions of different concentrations, ranging from 20 mg/mL to 1mg/mL. The thickness

of the SiNC layer in each device was measured by AFM. The concentration of SiNCs

solution and the corresponding average thickness of SiNC layer are summarized in Table

4.4.

Table 4.4 Thickness of SiNC layer as a function of the concentration of SiNC solution used in fabrication process.

Solution Concentration for SiNC layer fabrication (mg/mL)	SiNC Thickness (nm)
20	53
10	28
5	26
1	9

Figure 4.12 demonstrates the electroluminescence from NC-OLEDs as a function of

SiNC solution concentration. In devices with the thickest SiNC layer (53 nm), as shown

in Figure 4.12 (a), no obvious additional organic transport layer emission was observed at

peak wavelength 525 nm or lower. As shown in Figure 4.12 (b), (c) and (d), while the

thickness of spin-coated SiNC layer is reduced with the decrease of SiNC solution

concentration, the electroluminescence of the ETL material (Alq_3) at 525 nm gradually

appears in the spectrum under the same applied current density. This result indicates that

the recombination zone might be shifting from SiNC layer towards the interface between

SiNC and Alq_3. From Chapter 3, incomplete coverage at small thickness of SiNC could

lead to poor charge and exciton confiment within SiNC layer, and lead to emission from

adjacent organic layer due to the carrier leakage through SiNCs. Figure 4.13 (a) suggests
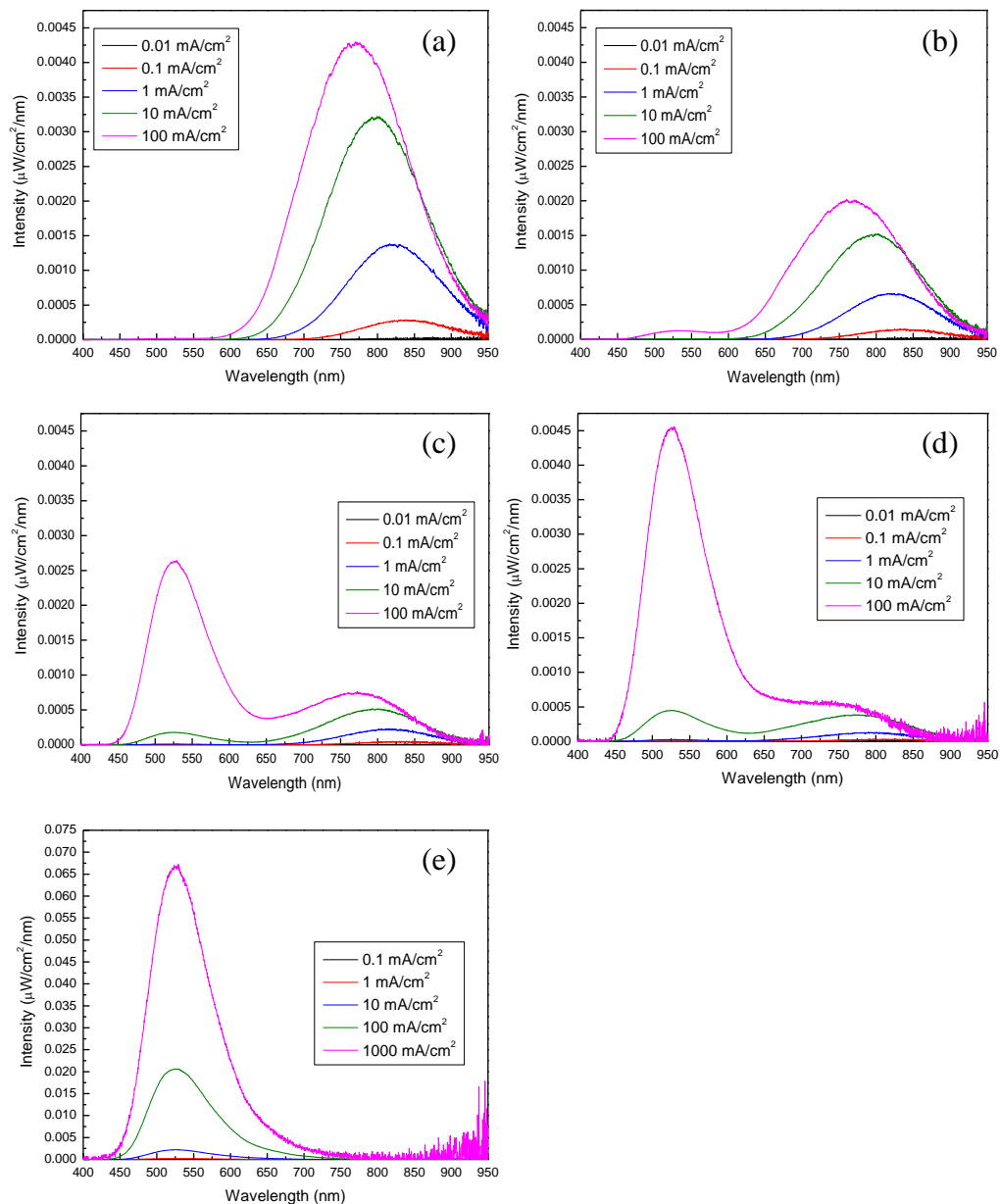
Figure 4.12 Device Electroluminescence as a function of SiNC thickness. (a)-(e) represent the EL from the NC-OLEDs made with 20, 10, 5, 1 mg/mL, and no SiNC. The peak emission at ~525 nm is attributed to the emission from the ETL (Alq$_3$).

that the coverage of SiNCs on poly-TPD is not complete in devices fabricatied with 1 mg/mL of SiNC solution. Such incomplete coverage could provide a direct path for carrier transport from HTL to ETL, leading to exciton formation in Alq$_3$. In addition,

according to the proposed energy level diagram under zero applied bias (Figure 4.8 (a)), the energy barrier for holes (0.5 eV) is smaller than the one for electrons (1.6 eV). Therefore, with sufficient electrical excitation, hole carriers are more likely to overcome the energy barrier and leak through SiNCs. Those hole carriers could enter the ETL to form excitons with electrons, resulting in shift of the exciton recombination region from the SiNC layer to the adjacent ETL. On the contrary, improved coverage (as shown in Figure 4.13 (b)) at increased SiNC thickness (e.g., 53 nm) could suppress emission from Alq3, leading to pure emission from SiNCs.
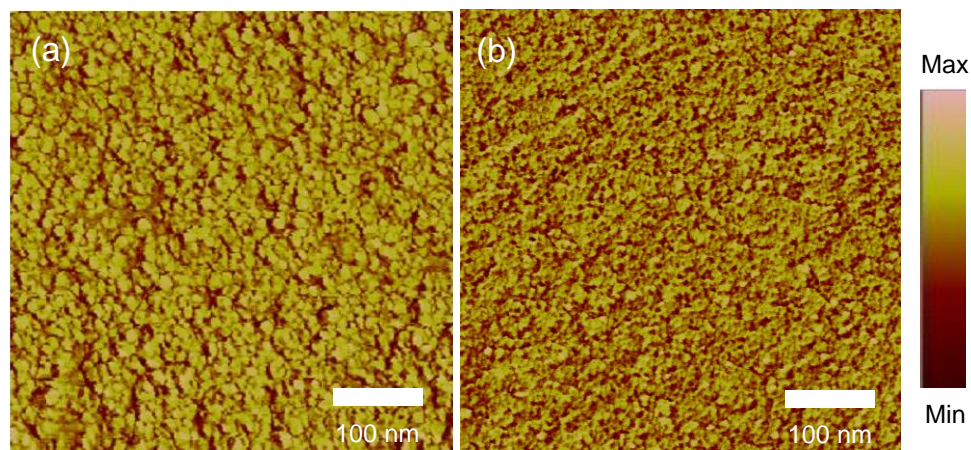
Figure 4.13 Atomic force microscopy (AFM) phase image of silicon-nanocrystal (SiNC) films spun-cast onto poly-TPD from solutions with SiNC concentration of 1 mg/mL (a) and 20 mg/mL (b). The scan size is 500 by 500 nm.

4.7   Emission Mechanism

Previous work in Chapter 3 has suggested that devices based on SiNCs operate via direct charge trapping on the nanocrystals, and not by excitonic energy transfer from an adjacent organic transport layer.[178] For the 20-nm ETLs examined here, this is also expected to be the case since the turn-on voltages for luminescence are much smaller than

the energy gaps of Alq$_3$ (1.55 V vs. 2.7 eV), TCTA (2.05 V vs. 3.3 eV), and CBP (1.30 V vs. 3.4 eV). This, along with the significant barrier for hole-injection into each material and the lack of ETL luminescence, confirms that excitons are not created on the ETL, and that charge carriers are injected directly into the SiNC layer. The direct injection of electrons and holes into the nanocrystals is likely facilitated by the fact that ligands of 1-dodecene only partially cover the nanocrystal surface.[189] The remaining surface sites are hydrogen terminated. In such locations, charge carrier injection into the particle is likely more efficient, and clearly permits the realization of high efficiency with low-voltage operation.

4.8 Discussion for Design Framework

As mentioned in the previous sections, the adjacent wide energy-gap transport materials with sufficient energy barriers for charge confinement could result in high performance of SiNC-OLEDs, provided the cross-linkable HTL material reduces the re-dissolving of HTL into SiNC layer and ETL is kept thin. These design rules can be tested by removing either the ETL or the HTL for comparison of device performance. When the top ETL is removed, the device efficiency is reduced to 4.4% due to the exciton quenching from the metallic cathode. (Figure 4.14(a)) On the contrary, when the bottom HTL is absent, the efficiency of the devices containing 20 nm CBP decreases from 6.8% to 2.9%. (Figure 4.14 (b)) This efficiency reduction could originate from the electron leakage during the device operation, since there is no sufficient energy barrier blocking electrons. However,
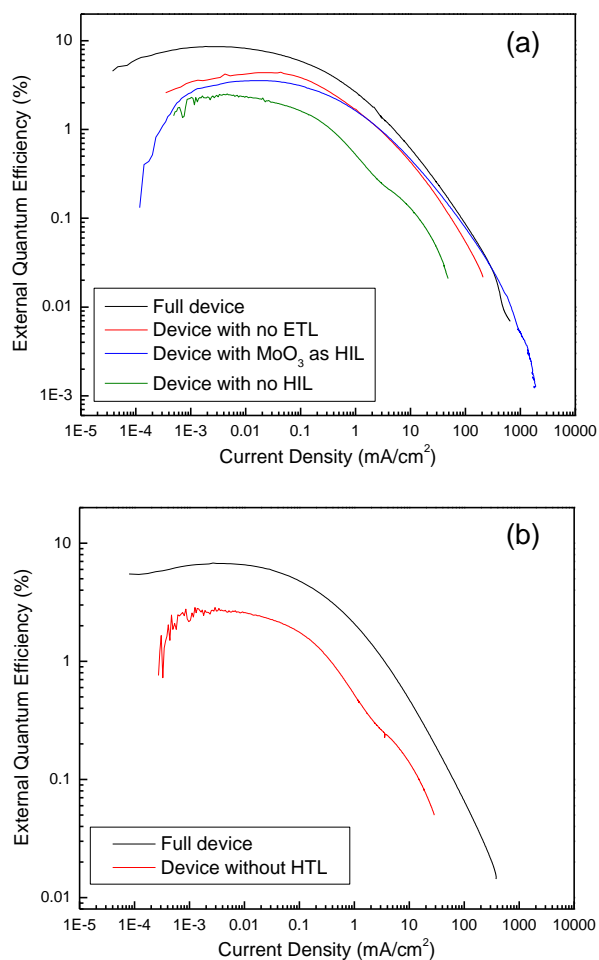
Figure 4.14 (a) Comparison for device efficiency of the full device with 20-nm Alq$_3$ as ETL, device with no ETL, device with no HIL (PEDOT:PSS), and device with MoO$_3$ as a HIL, (b) Comparison for device efficiency of the full device with 20-nm CBP and the same device structure with no HTL (poly-TPD).

the absolute efficiency drop might not be as significant as ~4% considering the contribution from the thinner SiNC layer; the fabrication condition (the speed of spin coating) for SiNC in this case is changed from 2000 to 3000 rpm in order to maintain the uniform coverage on HIL (PEDOT:PSS). These comparisons confirm the importance of the adjacent transport layers for charge confinement in the SiNCs and dictate the

contribution of each layer in the device performance. All the device performance is summarized in Figure 4.15 for clear comparison.

In addition, the importance of hole injection layer (HIL) has also been studied. The HIL could planarize the surface of ITO and potentially enhance the wetting for the incoming spin-coating solution.[190] The preliminary result indicates that the device efficiency could be reduced to ~2.5% if the HIL (PEDOT:PSS, in this work) is absent. Such efficiency reduction could result from the insufficient hole injection and the surface roughness[191], or morphology change due to the different interaction between ITO and HTL (poly-TPD) or between HIL and HTL. The final morphology could be altered due to such interfacial interaction, leading to the change of carrier injection or variation of charge-and-exciton confinement. Interestingly, when replacing PEDOT:PSS with 5-nm MoO_3 (HOMO: 9.7 eV, LUMO: 6.7 eV) as HIL in the device[192], the device efficiency of only 3.6% is achieved. This low efficiency is indeed predictably since the adoption of the thin MoO_3 could potentially lead to incomplete layer and likely cause high roughness for the spin-coated HTL.

4.9 Summary

In this chapter, the silicon NC-OLEDs demonstrated the peak external quantum efficiencies of up to 8.6% for electroluminescence at a wavelength of 853 nm. With a series of investigations in this work, the guidelines for the design framework in fabrication of highly efficient hybrid silicon NC-OLEDs are as follows:

1. Presence of hole injection layer (HIL): HIL planarizes the ITO surface and provide a better spin-coating platform for incoming organic layer fabrication, in which the surface roughness is reduced and the morphology of the top organic layer could be uniform due to the better wetting.

2. Energy barriers for the confinement of charges: wide band-gap organic semiconductors creates significant energy barriers to prevent hole-and-electron leakage.

3. Cross-linkable hole transport layer (HTL): UV-curable polymer creates a surface orthogonal to the incoming solution of SiNCs, effectively preventing the re-dissolving of HTL into SiNC layer during the device fabrication.

4. Optimized thickness of emissive material layer: optimized thickness of the layer efficiently confines charges and excitons within the SiNC layer.

5. Thin electron transport layer (ETL): thin ETL serves as a capping layer for SiNCs, preventing cathode quenching and further direct exposure of SiNCs to the air.

The aforementioned discussion indicates that this device performance is enabled by the optimized confinement of electrons and holes in the nanocrystal layer. High efficiency operation is observed for a variety of ETL materials, suggesting that the EL potential of the silicon nanocrystals is very robust.

Chapter 5 Role of Surface Ligand Passivation in Hybrid Silicon Nanocrystal Organic Light-Emitting Devices

(Contributing Authors: Kai-Yuan Cheng, Rebecca Anothiny, Ting Chen, Uwe R. Kortshagen, and Russell J. Holmes.)

5.1 Overview

As the high device efficiency was demonstrated in the previous chapter, it is important to further understand the effect of SiNC material properties on the device behavior. Therefore, this chapter investigated the relationship between the surface ligand coverage on SiNCs and the corresponding device performance in hybrid SiNC-OLEDs. The device efficiency is observed to vary substantially with the ligand density on SiNC surface, despite the fact that a much smaller variation is observed in the photoluminescence efficiency of the SiNCs. The lack of correspondence between changes in the photo- and electro-luminescence efficiencies suggests that the passivation density strongly impacts the charge injection and exciton formation efficiencies under electrical excitation. Here, we show that the hole transport within the device is related to the ligand coverage. These results suggest the design rules for the optimization of ligand coverage on SiNCs for application in highly efficient SiNC-OLEDs.

5.2 Introduction to Surface Ligands for Silicon Nanocrystals

In collodidal NC systems, surface passivation was introduced after the NC synthesis for the purpose of stabilization of colloidal solution, minimization of NC aggregation,

and reduction of non-radiative recombination.[11] Typically, in II-VI or III-V NC systems, organic molecules trioctylphosphine (TOP) or trioctylphosphine oxide (TOPO) are usually used as surface ligands. In colloidal SiNCs, the nanocrystal surface is usually capped with organic surface ligands.[16, 189, 193] These surfactant-like molecules form an organic shell over the core material, preventing the oxidation and aggregation of individual nanocrystals. Surface functionalization is often realized using alkene hydrosilylation, in which unsaturated carbon-carbon bonds replace an existing surface silicon-hydride group.[160, 194-196] The formation of robust Si-C bonds reduces the density of dangling bonds on surface and prevents oxidation of the nanocrystals, enabling the observation of high PL efficiencies.[147] This ligand-attachment approach can be achieved in either liquid or gas phase after material synthesis, allowing for material dispersion in non-polar solvent systems, permitting the realization of printable or coatable inks that can be used for device fabrication.[197] As already noted in Chapter 3 and 4, hybrid nanocrystal-organic light emitting devices (NC-OLEDs) integrating colloidal SiNCs and organic semiconductor charge transport layers have been used to demonstrate efficient SiNC electroluminescence (EL) over a wide range of electromagnetic spectrum.[198, 199]

Although the role of SiNC surface functionalization has been previously examined in the context of enhanced PL and material solubility, the correlation between surface ligand coverage and the device efficiency in NC-OLEDs has not been well characterized. Previous work in Chapter 3 has suggested that the electrical excitation of the exciton comes via the direct injection of charge into SiNCs.[198, 199] As such, the degree of the ligand grafting is expected to strongly impact both charge injection and confinement in

SiNCs. By quantifying the 1-dodecene ligand density on the SiNC surface, the dependence of device performance on the degree of ligand grafting is studied, providing insight into surface-ligand effects on charge carrier transport in the device.

5.3 Experimental Methods

5.3.1 Silicon Nanocrystal Synthesis and Passivation

Silicon nanocrystals used in this research was synthesized by the nonthermal plasma process using procedures described from the reference.[197] Silane (5% in He) was injected into the reactor tube with an Ar carrier gas at flow rates of 12 sccm and 30 sccm, respectively. The reactant gas was dissociated with 85 W of rf power at reactor pressure of 1.4 torr. The SiNCs were formed from silane fragments in the plasma and collected on a fine steel mesh downstream of the reactor. After the SiNC synthesis, the surface functionalization of SiNCs was performed in N_2 in a hydrosilylation solution with various volume ratios of 1-dodecene to mesitylene. (In this chapter 1:5 and 1:2000 were selected) The stock solution was heated to 215^oC and kept for 2 hours under reflux condition.

5.3.2 Characterization of Silicon Nanocrystal Photoluminescence and Ligands

The photoluminescence of the colloidal SiNC solution and thin film was collected within an integrating sphere coupled with a spectrometer (Ocean optics, Inc. USB2000 and HR4000). The samples were excited by a UV light emitting diode at peak wavelength of 395 nm. The PL efficiency of the SiNC solution was calculated as a ratio

of the integrated area of emission peak and absorption peak under the excitation of UV-LED.[147]

The surface ligand was conducted by using a Fourier Transform Infrared (FTIR) spectrometer with a diffuse reflectance unit (DRIFTS) from Bruker Optics Inc. The samples were prepared by drop-casting the solution of functionalized silicon nanocrystals on a gold-coated silicon wafer. The sample preparation and the data collection were performed within the glovebox in order to reduce the possibility of oxidation.

The Thermogravimetric analysis (TGA) measurement was carried out by using a Diamond TG/DTA (Perkins Elmers Inc.). The colloidal SiNC samples were compressed onto an aluminum pan. The measurement was performed under the nitrogen environment with the heating rate of $10^{o}C/min$. The data points before $110^{o}C$ was disregarded in order to prevent over-estimation from solvent and moisture.

5.3.3   Device Fabrication and Characterization of SiNC-OLEDs

The devices studied in this chapter were constructed on indium-tin oxide (ITO) coated glass slides. Poly(3,4-ethylenedioxythiophene):poly(styrenesulfonate) (PEDOT: PSS) with the thickness of (36±5) nm was spin-coated (spin condition: 3000 rpm for 30 sec) on ITO as a hole injection layer. The layer was baked at $150^{o}C$ for 90 minutes, followed by spin-coating a (28±4) nm layer of poly(N,N'-bis(4-butylphenyl)-N,N'-bis(phenyl)benzidine (poly-TPD) from a 5 mg/mL solution in chloroform (spin condition: 8000 rpm for 90 sec). Further UV-curing of poly-TPD film was performed at wavelength of 254 nm for 80 min.[115, 179, 199] The SiNC layer was spin-coated from 20 mg/mL SiNC

solution in chloroform and baked at 64°C for 1 hour. The SiNC thin films was capped by a 20-nm electron transport layer, tris-(8-hydroxyquinolinato) aluminum (Alq₃), followed by a device cathode containing 0.5 nm LiF and 100 nm Al. The electron transport layer and the device cathode were deposited by thermal evaporation in a vacuum of 5×10^{-7} Torr. The thickness of spin-coated layers was measured by atomic force microscopy (Veeco Nanoscope IIIA atomic force microscope) The EL collection was conducted as described in Chapter 3.

5.4 Optical Properties of Silicon Nanocrystals and Surface Ligand Characterization

In this work, SiNCs with a diameter of 5 nm were synthesized using a non-thermal plasma process, followed by thermal hydrosilylation with organic ligands of 1-dodecene. [147, 197] In order to study the difference in ligand coverage on the SiNC surface, the volume ratio of 1-dodecene to the reaction solvent, mesitylene, is varied in the hydrosilylation solution. The ligand-to-solvent ratio of 1 to 5 and 1 to 2000 were selected in this study, allowing the investigation of how surface ligand density impacts the device efficiency. Here, the samples made from the solutions with dilution ratio of 1:5 and 1:2000 are referred as high-ligand sample (SiNCs with high ligand coverage) and low-ligand sample (SiNCs with low ligand coverage)

It is noted that, the photoluminescence (PL) properties of the SiNC solutions do not vary significantly when changing the ligand coverage on SiNCs. The peak of solution PL for the high-ligand sample is 839 nm with the PL efficiency of (49±3)%, while the one

from low-ligand sample is at 860 nm with the PL efficiency as $(51\pm2)\%$ (Figure 5.1 (a)). The high PL efficiency from the low-ligand sample suggests that very few surface defect states exist, given the fact that the exciton formation under photo-excitation is similar in both materials even when different ligand coverage presents.
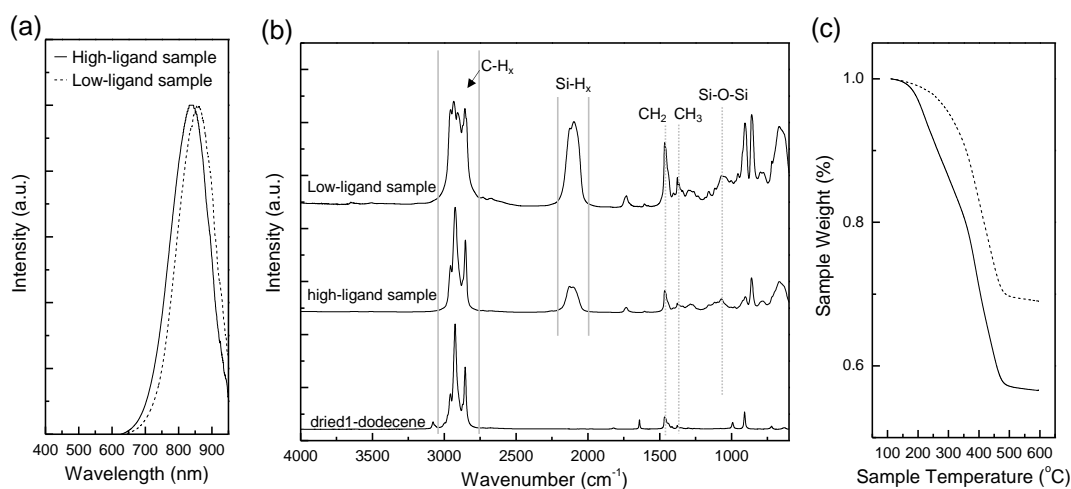
Figure 5.1 Material Characterization of silicon nanocrystals with different surface-ligand coverage: (a) normalized photoluminescence of high-ligand sample (functionalized with the volume ratio of 1-dodecene ligands to mesitylene as 1:5) and low-ligand sample (volume ratio of 1:2000), the spectra are normalized at the peak emission; (b) Fourier transform infrared spectra for low-ligand SiNC sample, high-ligand SiNC sample, and dried 1-dodecene thin films prepared from compressing samples on gold-coated silicon wafers; (c) Thermogravimetric analysis for the corresponding SiNC samples showed in (a) and (b). The mass is normalized at 110 $^{\circ}$C to eliminate the over-estimation of solvent (chloroform) and moisture.

The covalent bonding of ligands on SiNC surface is confirmed by the Fourier Transform Infrared Spectroscopy (FTIR) measurement. All the samples are compressed onto gold-coated silicon wafers as thin films for FTIR measurement. Figure 5.1 (b) shows the FTIR spectra of high-ligand sample, low-ligand sample, and neat film of dried 1-dodecene. The absence of C=C signal in ligand passivated SiNCs at 1640 cm^{-1} confirms that most 1-dodecene chains are chemically bonded to the surface after the reaction. The

FTIR spectra of all the passivated-SiNCs show additional strong peaks at 2800~3000 cm^{-1} corresponding to the -CH$_x$ stretching mode, and peaks at 1380 cm^{-1}, and at 1450 cm^{-1} corresponding to the deformation modes of -CH$_3$ and -CH$_2$, respectively. Each FTIR spectrum is normalized individually to the peak at 2924 cm^{-1} (-CH$_x$ mode) for internal comparison between –CH$_x$ and –SiH peak intensity in each sample. This relative ratio between two-peak intensities would qualitatively reveal the degree of ligand grafting on the SiNC surface. As shown in Figure 5.1 (b), the FTIR peak intensity of –CH$_x$ mode is observed higher than the one of –SiH mode in the high-ligand sample, suggesting the presence of more ligands on SiNC surface. On the contrast, the relatively equivalent signal intensities between –CH$_x$ and –SiH peaks indicate the lower ligand coverage on SiNC surface. However, it is difficult to systematically quantify the amount of ligands on SiNCs by calculating the ratio between the integrated areas of the –CH$_x$ and –SiH peak signals, as the FTIR signal is also sensitive to the film thickness which inevitably varies from one sample to the other.

In order to quantitatively determine the ligand coverage on the SiNC surface, thermogravimetric analysis (TGA) was carried out on the SiNC samples with varied degree of passivation.[196] During the heating process occurred in nitrogen atmosphere, ligands were removed from the SiNC surface by thermal energy and the evaporated organic molecules were further carried away by nitrogen gas, characterized as weight loss of the samples. The total ligand mass on SiNCs could therefore be quantified according to the measured weight loss and ligand density was thus determined by dividing the total ligand mass by the surface area of SiNCs. As shown in Figure 5.1 (b), the TGA data were

normalized at 110°C in order to eliminate the weight loss contributed by any solvent (chloroform) and moisture from the calculation. A clear difference in the weight loss is observed from the TGA data with 43% weight loss for high-ligand sample and 31% for the low-ligand sample, which corresponds to estimated ligand coverage of 5 ligands/nm^2 and 3 lignad/nm^2; respectively. To be noted, the calculation was carried out assuming spherical SiNCs with a diameter of 5 nm and that all the organics were removed at sufficiently high temperature with negligible oxidation during the process.[196] This quantification can serve as a standard index to identify surface ligand density and thus facilitate further study of the corresponding device performance.

5.5 Impact of Surface Ligand Coverage on SiNC-OLED Performance

In order to connect the measured ligand density to device efficiency, the SiNC-OLEDs were fabricated using high-ligand and low-ligand samples. The devices were constructed on indium-tin oxide (ITO) substrate with a ~36-nm hole-injection layer poly(3,4-ethylenedioxythiophene):poly(styrenesulfonate) (PEDOT:PSS), followed by a ~28-nm cross-linked hole transport layer poly(N,N'-bis(4-butylphenyl)-N,N'-bis(phenyl)benzidine (poly-TPD). The SiNC layer was spin-casted on top of the cured poly-TPD layer (2000 rpm, 90sec) and was capped with a 20-nm electron transport layer, tris-(8-hydroxyquinolinato) aluminum (Alq$_3$). The device cathode was consisted of a 0.5-nm LiF and a 100-nm Al layer. The thickness of the SiNC layers in all devices was fixed ~100 nm.

Figure 5.2 (a) shows the performance for NC-OLEDs constructed using nanocrystals from high-ligand sample (5 ligands/nm^2) and low-ligand sample (3 ligands/nm^2), respectively. The current density-voltage character is collected by semiconductor parameter analyzer, while the optical power of the electroluminescence is measured by a large-area photodiode with a diaphragm.[199] The device containing high-ligand sample realized a peak forward-emitted, external quantum efficiency (η_{EQE}) as 7.9% at 1.2 μA/cm^2, while the device containing low-ligand sample shows a significant reduction in device performance with an η_{EQE} of only 1% at 5.4 μA/cm^2. Interestingly, in Figure 5.2 (b), the current density-voltage characteristics of the NC-OLED containing SiNCs with the coverage of 3 ligands/nm^2 has an order of magnitude larger in current density than the identical device using SiNCs with ligand coverage of 5 ligands/nm^2. Despite this difference in current, the measured optical-power-output values from both devices are very similar. (Figure 5.2 (c))

Since both the PL efficiencies of two materials and the maximum optical power capacity of the corresponding devices are similar, the optical behavior of the materials is likely not responsible for the observed reduction in the device external quantum efficiency. Therefore, the observed variation in device efficiency could lie in the change
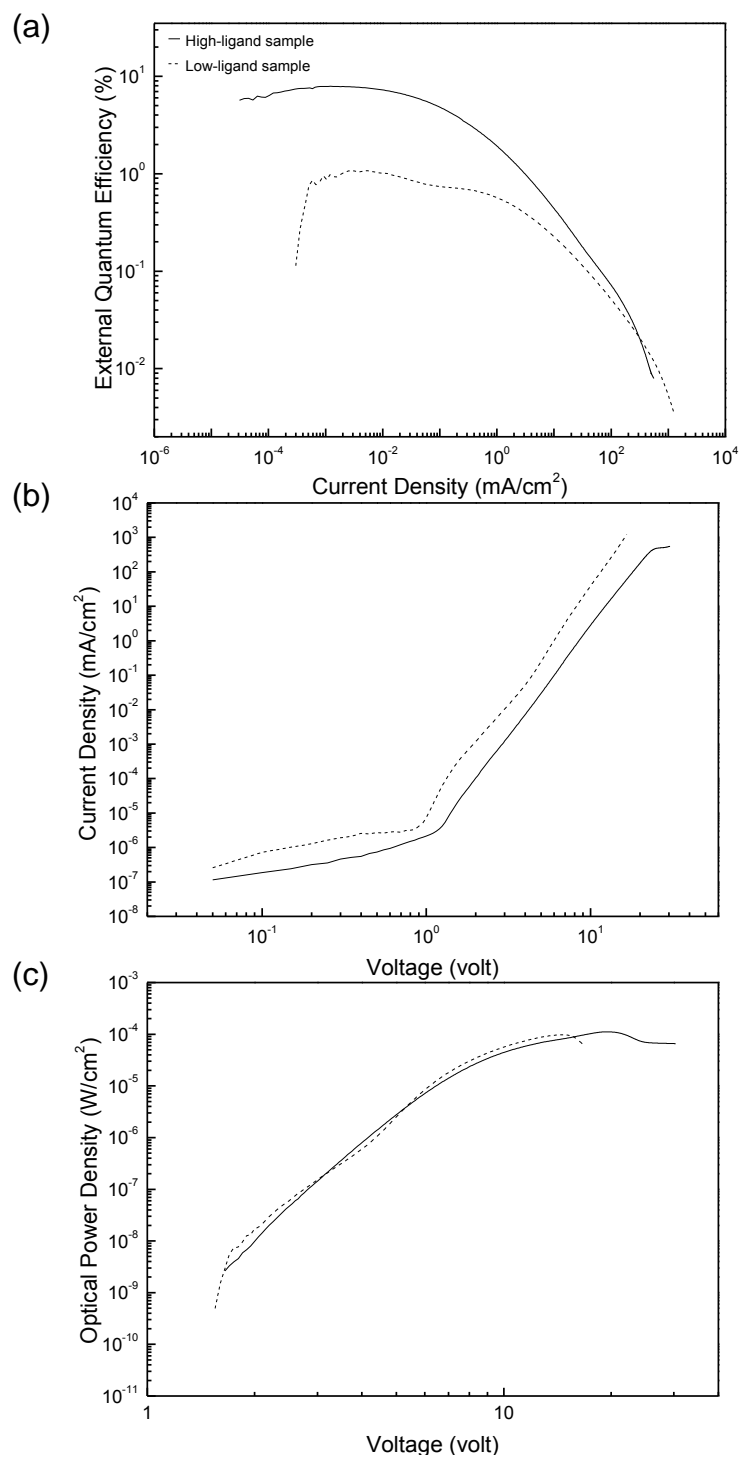
Figure 5.2 Performance of SiNC-OLEDs using nanocrystals from high-ligand and low-ligand samples: (a) External quantum efficiency, (b) current density-voltage response, and (c) optical power density output of SiNC-OLEDs using high-ligand sample (solid line) and low-ligand sample (dash line).

of charge transport, since the current density is by an order of magnitude higher in the device containing low-ligand samples. Such information indicates a substantial leakage of charge carriers through the device without leading to exciton formation. The influence of ligand density on charge injection into the nanocrystals would further affect the balance between the hole and electron population for radiative recombination in SiNCs.

As shown in the normalized electroluminescence collected as a function of applied current density (Figure 5.3), the device containing low-ligand sample presents noticeable
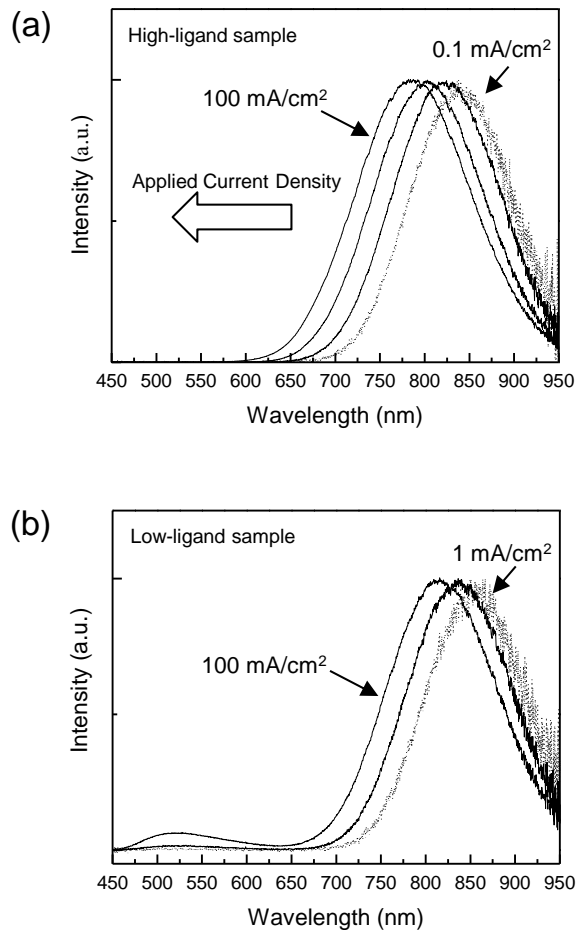
Figure 5.3 Normalized electroluminescence (EL) of silicon nanocrystals as a function of increasing applied current density for (a) hybrid silicon nanocrystal-organic light emitting device (SiNC-OLEDs) with high-ligand sample, and for (b) hybrid SiNC-OLED with low-ligand sample. Each spectrum is normalized at the peak of EL.

emission from the ETL (Alq₃) at the applied current density exceeding 10 mA/cm^2, while no ETL emission is observed in the device consisting high-ligand sample. The plausible explanation for the additional ETL emission is that the device is hole-rich, suggesting that the hole confinement is poor and more sensitive to ligand density than that of electrons, when lower surface-ligand density presents. Imbalanced population between electrons and holes induced by reduced hole confinement within SiNCs is likely to shift the region of exciton formation/recombination toward the interface between SiNCs and Alq₃. The hole-only device fabricated with gold as a device cathode also demonstrated the higher current when using low-ligand samples, supporting the hole-leakage phenomena observed in the corresponding NC-OLED performance. (Figure 5.4) Therefore, controlling the surface ligand density offers an effective approach to manipulating the charge balance and thus improving the device efficiency.
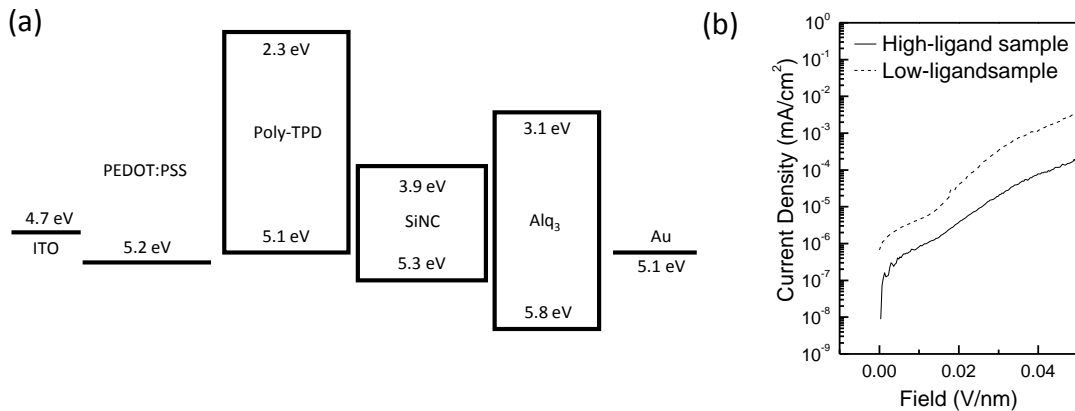
Figure 5.4 Impact of ligand coverage on hole current performance and single-carrier-device behavior. (a) Proposed energy level diagram of hybrid hole-only device with 5 nm SiNCs and a gold cathode for allowing the hole-only current transport. Note that the ligand barrier surrounding SiNCs is not included within the figure; (b) preliminary hole-only current behavior for high-ligand and low-ligand samples in hybrid structure; (c) hole and (d) electron current for single-carrier devices containing high-ligand and low-ligand samples.

5.6 Contribution of Physically Adsorbed Ligands to Device Performance

The contribution of physically and chemically bonded ligands is investigated in this work. During the drying of hydrosilylation solution, the un-reacted 1-dodecene molecules could be physically adsorbed onto the SiNC surface or trapped by other grafted ligands. In order to confirm whether the physically absorbed 1-dodecene molecules would significantly affect the device behavior, devices containing washed and un-washed SiNCs were fabricated for comparison. The SiNC solution was washed with acetonitrile in order to remove the trapped 1-dodecene residue. The acetonitrile could disturb the SiNC dispersion equilibrium in choloroform solution and separate the trapped ligands from the particle surface. The precipitated nanocrystals were further centrifuged at 3500 rpm for 11.5 minutes followed by drying in vacuum. Similar procedure has been developed in the synthesis of II-VI semiconductor nanocrystals to separate the reactant residue.[80] The dried sample was re-dispersed into chloroform for device fabrication. Figure 5.5 shows the comparison of the NC-OLEDs using samples before and after wash. In Figure 5.5 (a), the device made by washed SiNCs presents a slight drop in efficiency but still maintain a peak EQE > 4%, which is not as significant decrease as that observed in the low-ligand density device. Also, similar current-voltage and optical power-voltage characteristics are observed in Figure 5.5 (b), suggesting that the physically adsorbed ligands are not as significantly dominating the device performance as the contribution from the ligand coverage.
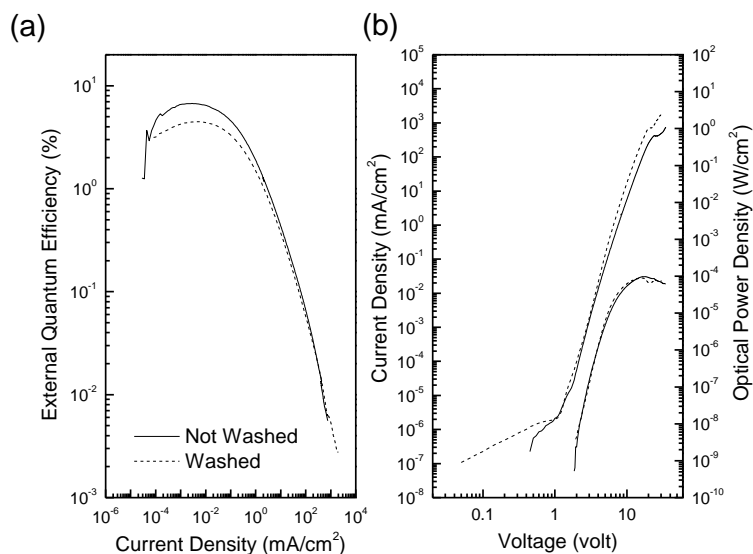
Figure 5.5 Investigation of device performance with SiNCs before and after washing with acetonitrile: (a) External quantum efficiency for the devices containing before (solid) and after (dash) SiNC washing; (b) current-voltage and optical power density characteristics for the devices in (a).

5.7 Correlation between Surface Ligand Density and Device Performance

By varying the ligand density, the impact of ligand coverage on the material photoluminescence and the device efficiency can be summarized in Figure 5.6. Figure 5.6 (a) shows the solution PL efficiency of the SiNC samples as a function of weight loss, which characterizes the ligand density as illustrated in previous discussion. No significant difference in PL is observed across the range of the studied degree of passivation. However, the device efficiency exhibits a significant dependence on weight loss, i.e., ligand coverage on SiNCs. In the region of low weight loss (< 35%), the device efficiency is low and also similar to the one reported in Figure 5.2. As the volume ratio is changed to 1:5, more weight loss from the samples is observed in TGA as mentioned

earlier, indicative of higher ligand density; also higher efficiency is obtained in the corresponding devices. In the high-device-efficiency region, the same volume ratio (1:5) sometimes results in certain degree of change in surface grafting, as indicated by the variation of weight loss from 41 to 52%, leading to some variation in the device efficiency correspondingly. However, all device efficiencies fall into the high device efficiency region, i.e., > 4.5% and no device efficiency as low as 1% is reported in this region. (Figure 5.6 (b))

The ligand coverage could potentially affect the applied field for achieving the same charge injection. A value of ligand density greater than 5 ligands/nm^2 could result in a large difference in applied field. In Figure 5.6 (c), the applied voltage required for current density of 0.1 mA/cm^2 is plotted as a function of estimated ligand density. The required applied voltage to acheive 0.1 mA/cm^2 is much higher when device contains SiNCs with higher ligand density. This could be attributed to either the different ligand configuration on SiNC surface or the larger separation between nanocrystals in solid-state films. Although it may require larger field to inject charges to the highly-passivated SiNCs, the charges could be much better confined within the nanocrystals and thus reflect more efficient exciton formation and recombination. This result suggests that the efficient NC-OLEDs might be achieved with the optimized surface ligand density.
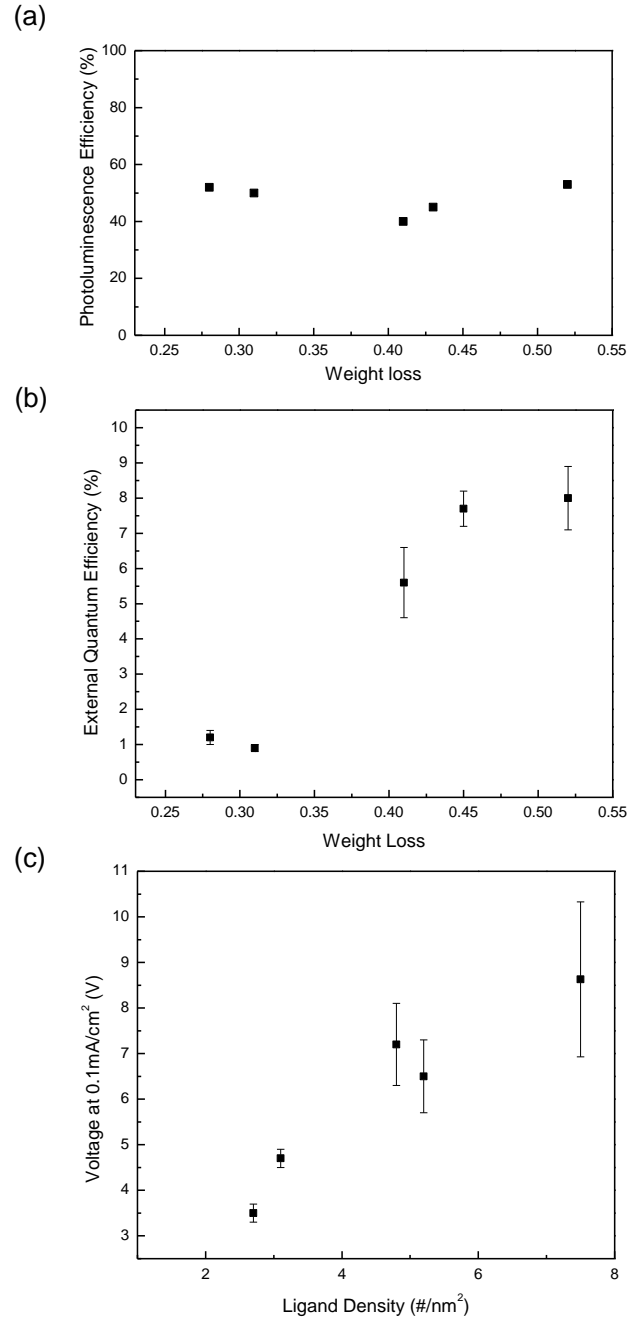
Figure 5.6 Impact of ligand coverage: (a) Solution-photoluminescence efficiency for the SiNC samples with different degree of ligand grafting; (b) External quantum efficiency of devices using the SiNC samples described in (a); (c)Voltage response from the devices in (b) as a function of surface ligand density. The voltage data are selected at current density of 0.1 mA/cm^2.

5.8 Summary and Conclusion

In conclusion, the electroluminescence efficiency of silicon NC-OLEDs is highly sensitive to the ligand density on SiNCs surfaces, while no strong impact of ligands is observed in the corresponding material photoluminescence performance. Decreased ligand density is believed to be associated with less hole confinement. Such influence will cause charge imbalance between holes and electrons and thus results in poor device performance. The work described in this chapter provides an insight for understanding the impact of surface ligand on the device performance, offering guidelines for highly-efficient silicon NC-OLEDs fabrication.

Chapter 6 All-Gas-Phase Approach for Manufacturing Light Emitting Devices

(This work was previously published in: "Anthony, R. J., Cheng, K., Holman, Z. C., Holmes, R. J. & Kortshagen, U. R. An All-Gas-Phase Approach for the Fabrication of Silicon Nanocrystal Light-Emitting Devices. *Nano Lett.* **12**, 2822-2825 (2012)". Copyright 2012 American Chemical Society)

6.1 Overview

Although the multi-layer device design could provide efficient nanocrystal (NC) electroluminescence (EL)[14, 15, 115-117, 122, 123, 125-127, 135, 178, 198, 199], the devices are usually fabricated by solution process. In general, there are serval potential challenges associated with solution processing. First, solution-processable NC/organic materials have to be used, which limited the options for material selection. Second, solvent compatibility between adecent layers has to be carefully considered to prevent re-dissolving issues at the interfaces. Third, minimum energy-and-time waste is required in annealing treatment during the post-processing. These issues will be the obstacles for integrating the device fabrication into the streamline of the traditional semiconductor manufacture for the scalable high-through-put mass production in the future.

An all-gas-phase manufacture of light-emitting device (LEDs) could potentially solve the aforementioned inconvenient difficulties and realize the possibility for next-generation NC-based LED applications. As the number of processing steps is reduced for fabrication in the absence of liquid-phase treatment, it is possible to develop a simple route for dry device fabrication leading to realization of SiNC EL. However, to date, very

few experiments have explored in NC-LEDs using an all-gas-phase method.

In this chapter, an innovative all-gas phase method to make luminescent SiNC thin films is described, allowing the creation of dense films of luminescent nano-materials without adopting any solution process steps. Such method provides the possibility for integration of the device fabrication with conventional capital semiconductor equipment/process, conservative material usage, and possible deposition for different types of nanomaterials which is unsuitable for solution processing. The un-optimized SiNC-LED made with this approach can successfully demonstrate EL from single SiNC layer, with the peak device efficiency ~0.02%.

6.2   All-Gas-Phase Method for Single-Layer SiNC-LED Fabrication

In Chapter 4, the fabrication of highly efficient SiNC-OLEDs was described, and included multiple solution processes, annealing conditions, and careful selection of the compatible material and solvent systems. It would be ideal for the next generation of device fabrication if the thin-film deposition of the emissive layer could be made from the gas phase in absence of adopting liquid phase solution. Such a dry process could potentially eliminate all the steps for introduction and removal of solvents, which could be more suitable for integration of the luminescent thin-film fabrication into the current semiconductor technology. Here, an innovative approach for luminescent thin-film deposition has been proposed.[200] The system integrated the SiNC synthesis, in-flight surface ligand passivation, and luminescent-nanocrystal thin-film deposition within one single streamline fabrication process.

Such a technique was first invented by Holman and Kortshagen, exploiting a non-thermal plasma reactor for a gas-phase impaction process to deposit germanium nanocrystal thin films.[201] The infrastructure includes a flow-through non-thermal plasma reactor with a slit-shape orifice at the downstream of the gas flow, which allows control over the NC gas-phase impaction and patterning parameters (Figure 6.1). In the present work, an additional precursor container is attached to the reactor for afterglow surface passivation before the downstream gas flow into the orifice. This gas-phase plasma-afterglow-initiated reaction could covalently attach the alkene molecules (1-dodecene in this work) to the SiNC surface, which has been demonstrated in the literature.[197] This surface passivation could potentially reduce the surface defect of SiNCs and enhance the solubility of NC in the nonpolar solvents.
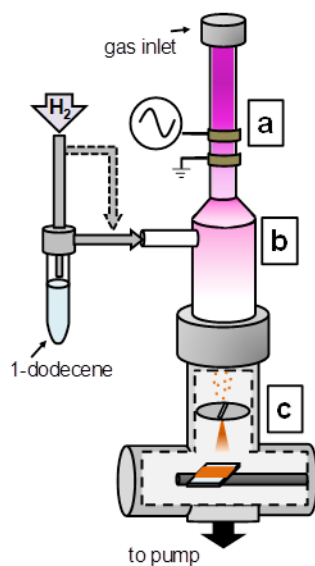
Figure 6.1 Schematics of all-gas-phase SiNC synthesis (a), functionalization (b), and impaction (c) scheme.

plasma reactor at a flow rate of 13 standard cubic centimeters per minute (sccm) with argon gas flow varied from 35 to 100 sccm. The reactor pressure was measured as 180

Pa. A non-thermal plasma zone was excited by a pair of electrode rings attached to the reactor using a radiofrequency 13.56 MHz at a nominal power of 80 W (Figure 6.1 (a)). At the afterglow region of plasma, the precursor vapor of 1-dodecene was introduced with a hydrogen gas flow at 100 sccm (Figure 6.1 (b)). With the sufficient energy in the afterglow zone in the plasma, the surface passivation was initiated within the gas phase after the SiNC synthesis. After the synthesis and surface passivation of SiNCs, the SiNCs pass through a slit-shaped poly-tetrafluoroethylene (PTFE) orifice. (Figure 6.1 (c)) The downstream pressure after the orifice is reduced to ~ 32 Pa, due to the expansion of the gas flow. The substrates were attached to a stainless-steel pushrod and located < 1cm below the orifice opening. The SiNCs were inertially impacted straight to the substrates, such as glasses coated with indium tin oxide as electrode for LEDs, or the ITO substrate coated with aluminum for thickness examination. The thin-film samples after thin-film deposition were sealed in vacuum before removal of the pushrod and immediately transferred into a nitrogen-purged glovebox for further cathode deposition or FTIR analysis. Again, it is very important that, from the SiNC synthesis, surface passivation, thin-film deposition to cathode processing, the overall manufacture of light-emitting device is based on gas-phase processing with no liquid phase involved in any step.

6.3   Thin Film Characterization

The thickness of the SiNC layer was studied by using a sample deposited on a 100-nm aluminum coated ITO substrate and coated with 3-nm platinum for improving the contrast under scanning electron microscopy (SEM). As the SEM cross-section picture

shown in Figure 6.2 (a), a 30-raster passes will provide ~ 425 nm thick SiNC layer. Such a value suggests that each pass forms 2-3 monolayers of SiNCs on the substrates,assuming the average size of the nanocrystal as ~4 nm. Figure 6.2 (b) shows the corresponding top-view of the SiNC thin film in Figure 6.2 (a), indicating the intrinsic nature of the gas-phase deposition process could potentially cause some roughness and random rifts during the film formation.
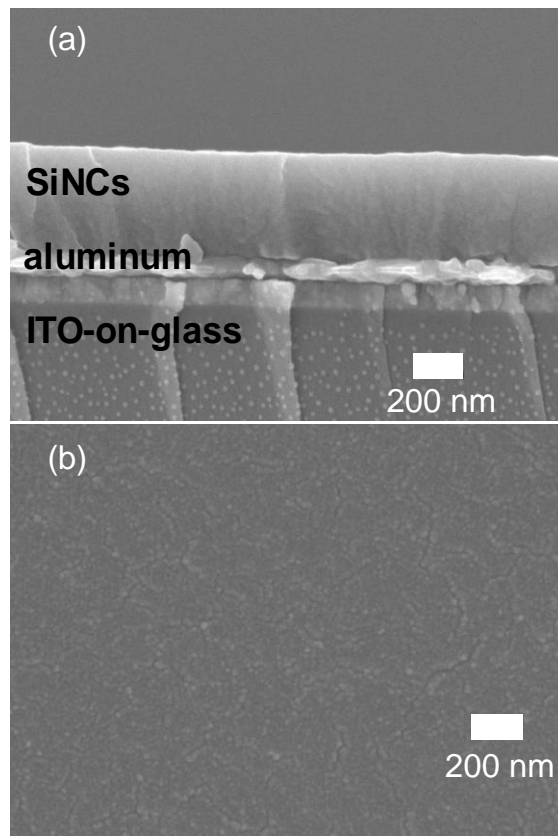
Figure 6.2 SEM images of SiNC films.   (a) Cross-sectional image of a SiNC layer, deposited on aluminum-coated ITO-on-glass, coated with 30 Å of platinum to improve contrast. (b) Top-down view of the same SiNC film, demonstrating layer uniformity.

In order to confirm the chemical attachment of surface ligands, FTIR spectroscopy is employed. The FTIR samples were collected by depositing about 1-2 μm SiNC thin film

on a gold-coated silicon wafer. The FTIR measurement was performed within the nitrogen-purged glovebox using a Bruker Alpha FTIR operated in diffuse reflectance mode (DRIFTS). For comparison, the SiNC thin films were prepared with and without ligand passivation. The FTIR spectra of neat 1-dodecene and the SiNC thin films with and without the ligand passivation are shown in Figure 6.3. The SiNC thin film without passivation demonstrates peaks of Si-H$_x$ at ~ 2100 cm^{-1} and 800-900 cm^{-1}.[197, 202] The same peaks display lower signal in the relative scale to the additional C-H$_x$ stretching vibration peak observed at ~ 2900 cm^{-1}, which is due to the presence of carbon chain in1-dodecene molecules. The absence of the peaks associated with C=C and CH$_2$ (at 1640 cm^{-1} and 3080 cm^{-1}, respectively) confirms the reaction of surface hydrosilylation is accomplished with the ligand chemically bonded to the SiNC surface.[197]

The thin-film photoluminescence (PL) of the gas-phase-passivated SiNCs is measured in an integrating sphere which is fiber-coupled to a spectrometer (Ocean Optics, Inc. USB 2000+). The ~1 μm-thick SiNC film was deposited on a glass substrate and was excited by an ultraviolet LED at wavelength of 395 nm in the integrating sphere. The collected PL spectrum is shown in Figure 6.4 (a), whose full width at half maximum (FWHM) is comparable to the previously reported thin-film PL.[178] The NC size is calculated as ~ 4.4 nm based on the corresponding thin-film XRD data (see Appendix) with Scherrer broadening estimation, accounting the assumption of spherical shape of NCs.
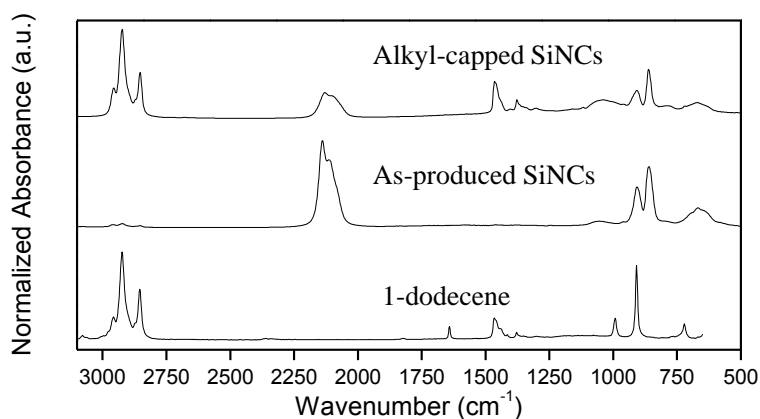
Figure 6.3 FTIR spectra from bare and gas-phase-functionalized SiNC films, with neat 1-dodecene also shown. The sharp peaks from the unsaturated carbon bond near 3080 cm^{-1}, 1640 cm^{-1}, and between 900–1000 cm^{-1} in the neat 1-dodecene spectrum are not present in the functionalized SiNC film, although –CH$_x$ and C-H$_x$ peaks are present. This indicates reaction of the 1-dodecene with the SiNCs in the gas-phase plasma-afterglow-initiated functionalization step.
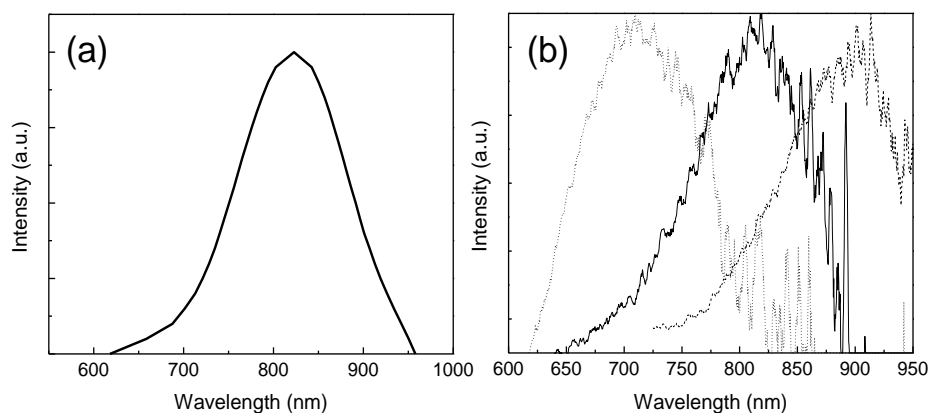
Figure 6.4 (a) PL spectrum with long integration time from a gas-phase-functionalized impacted SiNC film; (d) PL spectra from gas-phase-functionalized impacted films of different SiNC sizes, normalized to emission peak. From right to left, the PL peak wavelengths of these films are 900 nm, 817 nm, and 707 nm, with SiNC diameters of 5.1, 4.1, and 3.1 nm.

To verify the quantum confinement effect on SiNC PL, SiNCs of different size of SiNCs were synthesized by varying the argon flow rate through the non-thermal plasma reactor. Meanwhile, the width of the slit-shape orifice was increased to keep the pressure in the reactor close to 180 Pa, regardless of total gas-flow rate. As shown in Figure 6.4

(b), the PL peak is blue shifted from 900, 817, to 707 nm, as the SiNC size is decreased from 5.1, 4.1, to 3.1 nm. Such blue-shifting in PL confirms the quantum confinement effect in SiNCs, allowing tunable emission wavelength through engineering the SiNC size.

6.4   Device Performance

The single-layer SiNC-LEDs were realized through deposition of an 80-nm-thick layer of SiNCs in between the ITO-coated glass as anode and a capping cathode consisting of 0.5-nm LiF and 50-nm Al. The device shows SiNC EL at a peak wavelength of 836 nm for an applied current density of 100 mA/cm^2 (Figure 6.5). The slight red shift of the EL
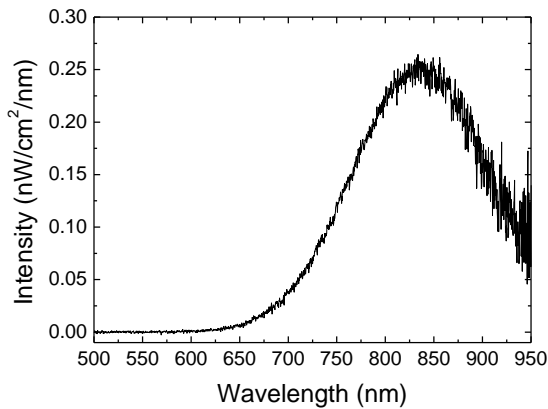
Figure 6.5 Device electroluminescence spectrums at a current density of 100 mA/cm^2.

from the PL shown in Figure 6.4 (a) is likely due to the sample-to-sample variation. A low peak device η_{EQE} of 0.02% is observed in Figure 6.6 (a), which falls below the reported value from the devices using multi-layer heterojunction structures. This reduction in efficiency likely comes due to the absence of adjacent charge blocking

layers, leading to significant carrier leakage (Figure 6.6 (b)). In addition, the surface-ligand passivation in the gas phase might be less efficient than the one processed in the liquid phase.
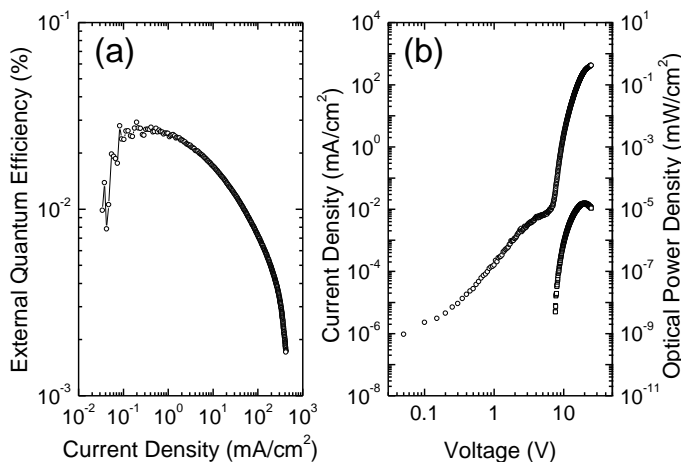
Figure 6.6 Device characteristics for an all-gas-phase SiNC LED. (a) External quantum efficiency and (b) current density and optical power density as a function of voltage.

6.5 Summary and Discussion

In this chapter, an all-gas-phase method for fabrication of NC-LED is proposed. The approach integrates nanocrystal synthesis, surface passivation, and film formation within a streamlined deposition in the absence of liquid phase processes, providing an innovative thin-film deposition scheme for versatile nanomaterials and substrates. The prototype single-layer SiNC-LED fabricated by this method demonstrates the SiNC EL, with device efficiency ~0.02%. Further optimized device efficiency would be possible by adding adjacent organic charge blocking layers into the device design or increasing the efficiency of the surface passivation.

Chapter 7 Conclusions and Future Work

The main focus of this work is to develop novel device architectures for highly efficient hybrid silicon nanocrystal-organic light-emitting devices (SiNC-OLEDs) and to investigate the device physics and engineering for further improvement of the device performance. A design framework has been proposed for high efficiency devices and a promising result has been presented. More investigation are still necessary in the future to understand the origin of high PL and EL efficiency of SiNCs and to elucidate the charge transport mechanism within the materials. A thorough understanding of these key issues will be beneficial to future device engineering and manufacture, and thus advance the pace of NC-OLEDSs towards commercialization. This chapter will summarize the result achieved so far and propose the direction for the future research.

7.1 Conclusions

This dissertation has examined the design, performance, and physics of novel hybrid inorganic NC-OLEDs by exploiting silicon nanocrystals (SiNCs) as the emitting materials. Chapter 3 demonstrates the first efficient electroluminescence (EL) from colloidal SiNCs. The device external quantum efficiency of 0.6% is achieved in the forward emitting direction. Direct charge trapping and exciton formation on SiNCs is suggested as the major excitation mechanism of SiNCs. Additionally, this chapter also investigated the connection between the SiNC EL performance and the corresponding film coverage and thickness. Better charge and exciton confinement is obtained in devices containing thicker SiNC layer completely covered on the conjugated transport

polymer layer.

Chapter 4 concludes the design framework for constructing a highly-efficient hybrid SiNC-OLEDs through engineering the charge and exciton confinement within the emissive layer. By introduction of the cross-linkable hole-transport layer (HTL) into the device design, it not only suppressed the re-dissolving of HTL into SiNCs, but also enhances the electron confinement within SiNCs due to the higher energy barrier for electrons. As a result, high peak device efficiency as 8.6% at wavelength of 853 nm is obtained through this optimized device structure. Such efficiency is, to our knowledge, the highest reported in the studies of hybrid NC-OLEDs to date. High efficiency operation is also observed within devices using various ETLs, suggesting that robust EL is achievable from SiNCs. Additionally, tunable efficient EL is tested by exploiting the SiNCs with smaller diameter (3 nm), offering the potential of realizing visible EL from SiNCs in future.

Chapter 5 investigates the connection between the surface ligand coverage on SiNC and the corresponding SiNC-OLED performance. Ligand coverage analysis shows that the surface ligand density could be changed from 5 to $3/nm^2$ when the volume ratio of ligand to solvent is varied from 1:5 to 1:2000 in the reaction solutions. The device efficiency is reduced when the device contains the SiNCs with less ligand coverage. The corresponding device showed higher current density and EL from the ETL, suggesting that the charge confinement is altered when fewer ligands are present on the SiNC surface. Further hole-only device confirms that hole leakage occurs while the number of ligands at the surface is reduced. As a result, hole leakage would be suppressed when

more ligands are attached to SiNC surface, leading to balanced hole-and-electron charge transport/confinement, and hence higher device efficiency. The results from Chapter 3, 4, to 5 have demonstrated the device engineering for solution processed SiNC-OLEDs, from the macroscopic prospective in the studies of each layer in devices to the microscopic point of view in the investigation of surface ligand coverage on SiNCs. The overall conclusion for the design framework could be summarized as follows:

1. Presence of hole injection layer (HIL): HIL planarizes the ITO surface and provide a better spin-coating platform for incoming organic layer fabrication, in which the surface roughness is reduced and the morphology of the top organic layer could be more uniform due to the better wetting (Chapter 4)

2. Energy barriers for the confinement of charges: wide band-gap organic semiconductors builds the significant energy barriers to prevent hole-and-electron leakage (Chapter 3 and 4)

3. Cross-linkable hole transport layer (HTL): UV-curable polymer creates a surface orthogonal to the incoming solution of SiNC, preventing the re-dissolving of HTL into SiNC layer during the device fabrication (Chapter 4)

4. Full coverage and optimized thickness of emissive material layer: full coverage of SiNCs and optimized thickness of the layer efficiently confine charge and exciton within SiNCs. (Chapter 3 and 4)

5. Thin electron transport layer (ETL): A thin ETL could serve as a capping layer for SiNC, preventing cathode quenching or further direct exposure of SiNCs to the

111

air. The bulk electron mobility would not affect the device performance significantly when the capping ETL remains as thick as 20 nm. (Chapter 4)

6. Sufficient ligand coverage on SiNCs: ligand coverage could affect the hole-carrier confinement within SiNCs, While more ligand present on the SiNCs, the hole leakage will be suppressed, leading to the balanced hole-and-electron charge transport and confinement, and hence the better device efficiency. (Chapter 5)

Device fabrication using all-gas-phase fabrication is introduced in Chapter 6. Such technique integrates the material synthesis, material-surface passivation, and thin film formation in the absence of liquid phase processing, providing potential compatibility with current semiconductor manufacturing technology. Promising SiNC EL is observed from single-layer SiNC-LEDs fabricated through the all-gas-phase method. Further device efficiency improvement by enhancing the ligand attachment efficiency and by adopting the organic charge-blocking layers in order to enhance the PL efficiency of SiNCs and charge/exciton confinement within SiNCs, respectively.

7.2 Future Work

As high efficiency in SiNC-OLEDs is achieved, it is important to further understand the fundamental physics behind the device performance and to rationalize the unique electrical and optical properties in SiNCs. The in-depth exploration of the correlation between the material and device physics will benefit the future design of SiNC-based devices. Therefore, the proposed future direction lies in first finding the origin of the high efficiency and the roll-off in device efficiency under higher electrical excitation. Besides

the device science, the investigation of the charge transport mechanism as a function of surface ligand length and coverage is also necessary, as it provides more information on the electrical properties of SiNCs for the next-generation SiNC material and surface ligand engineering. All of these knowledge is critical for serving as solid guidance for developing future highly efficient SiNC-OLEDs with red, green, blue, and white electroluminescence.

7.2.1 Origin of High Efficiency: Exciton Spin Fraction

The first step of understanding the origin of the high efficiency in SiNC-OLEDs lies in understanding the fraction of the electrical excited exciton states that can radiatively decay. Typically the allowed emitting fraction for fluorescent exciton states in an organic emitter is ~25% from singlet exciton recombination. In phosphorescent materials, due to the spin-orbit interaction, the triplet states (the portion of the rest of 75% excitons) are permitted to radiatively recombine. [203, 204] To date, few studies have been conducted to define and confirm spin statistics of the exciton states in SiNCs.

With the high external quantum efficiency demonstrated in chapter 4 and 5, it is possible that more than 25% of the exciton states could contribute to the SiNC EL. When the electrical excitation of excitons occurs, the general device external quantum efficiency could be a function of spin fraction factor for excitons forming singlets, charge balance factor, material photoluminescence efficiency, and out-coupling efficiency. If the out-coupling efficiency is ~20% in forward emitting direction for devices on planar substrates,[72] and the solid-state PL efficiency is similar to the one of SiNC solution (~

45%), then the upper limit of the product of charge balance and spin fraction for singlets (χ . γ) will be close to one as indicated in Equation 7.1.[205]

$$\chi \times \gamma = \frac{\eta_{EQE}}{\eta_{PL} \times \eta_{OC}},$$

(7.1)

where η_{EQE} is external quantum efficiency, η_{PL} is the photoluminescence efficiency of the emitter material, η_{OC} is the out-coupling efficiency, γ is the charge balance factor, and χ is the spin fraction for the singlet excitons.

According to the high device efficiency close to 9% is reported in Chapter 4 and 5, the product of charge balance and spin fraction for singlets (χ . γ) in SiNC-OLEDs could be estimated by using Equation 7.1, considering the PL efficiency (~45%) and the out-coupling efficiency (~20%). Since the charge confinement is well-established with the optimized device structure, the hole and electron charges are likely balanced while high efficiency is achieved. As such, the spin fraction for allowed radiative decay could be roughly estimated close to 1, suggesting that most of the exciton states in SiNCs (singlets and triplets) contribute to the radiative recombination. Although Calcott et al. proposed that the mixture of singlet nature into the triplet states is weakly allowed due to the spin-orbit interaction within Si nano-materials[206], it is more surprising that the device performance demonstrated such a high efficiency, proving more than 25% of exciton radiative emission. Therefore, the mixed states of singlet and triplet excitons could be responsible for the radiative recombination upon excitation and it relies on more investigation on the fundamental study in the future.

M. Segal et al. developed a method for probing the upper limit of the excitonic singlet-

triplet statistics by measuring the reversed-bias PL from the fluorescent OLEDs containing small organic molecule or polymer.[207, 208] Such value could provide the information of the available radiative exciton states. The system is summarized in Figure 7.1. A laser is employed to excite the device PL. The lens is adopted to focus the laser onto 1-mm-diameter area and is aligned with the device cathode. The excited PL is collected by a silicon photodiode through a second lens with the excitation laser filtered out by a 550-nm optical filter. By measuring the differential PL power and photocurrent, the system allows the determination of the "out-coupled PL efficiency" as indicated in Equation 7.2 and hence the estimation of the product of charge balance factor and the spin fraction factor. (see the derivation in Appendix)

$$\eta_{PL} \times \eta_{OC} = \frac{-q}{h\nu}\frac{\Delta P_{PL}}{I_{ph}}$$

(7.2)
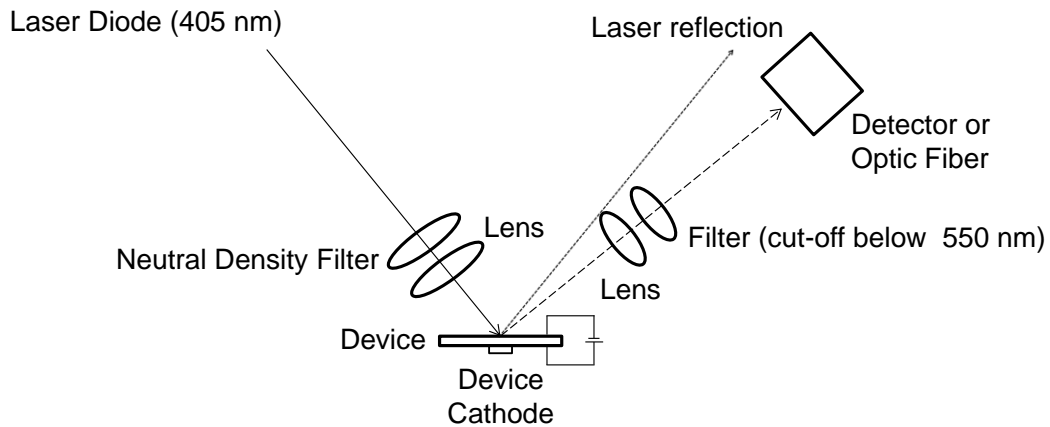
Figure 7.1 The experimental setup of the reversed-bias PL measurement (continuous wave): PL from device is excited with a laser diode at wavelength 405 nm and is collected with a silicon photodiode. An optical filter is used to eliminate any reflection of laser into the photodiode. A reversed-bias is applied during the measurement in order to obtain the photocurrent.

, where q is the electronic charge, h is Planck's constant, ν is the frequency of the radiated photons, Δ P_{PL} is differential photoluminescence power, and I_{ph} is the

115

photocurrent detected from the photodiode.

In order to efficiently excite the SiNC PL and to minimize the organic emission, the laser wavelength is picked at ~405 nm. The corresponding device design is modified due to the absorption at the excitation wavelength of 405 nm for materials of Poly-TPD and Alq$_3$ (Figure 7.2). The modified device, as shown in Figure 7.3, demonstrated a device efficiency of ~3%, which could serve as an initial device condition for testing the reversed-bias PL. Figure 7.4 plots the differential photoluminescence power as a function of the reversed bias. The slope of the differential PL power as a function of photo-current is changed around 4.5 V (~ 0.5μA) under reversed bias, which could be attributed to the leakage current.[207] Therefore, the slope fitted for the experimental data is taken before 0.5 μA. The corresponding upper limit of $\chi \cdot \gamma$ is estimated to be 36-56% due to the device-to-device variation, and the poor harvesting of the EL power. Table 7.1 summarizes the key results of coupled PL efficiency and external quantum efficiency obtained from the initial trial.
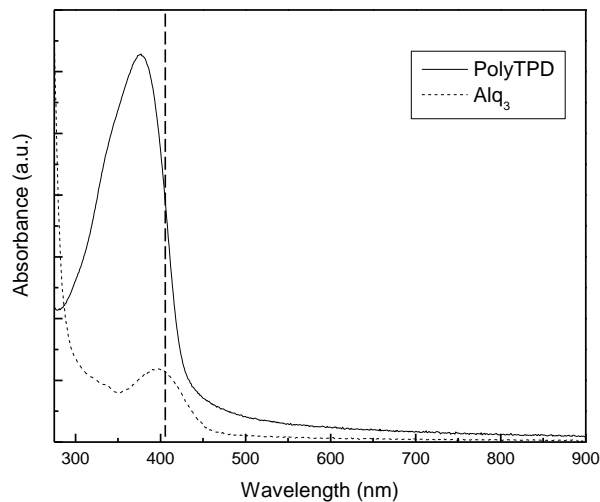
Figure 7.2 Absorbance of thin-film PolyTPD and Alq$_3$ on glass substrates. The vertical dash line indicates that both materials absorb at the excitation wavelength of laser diode (405 nm).
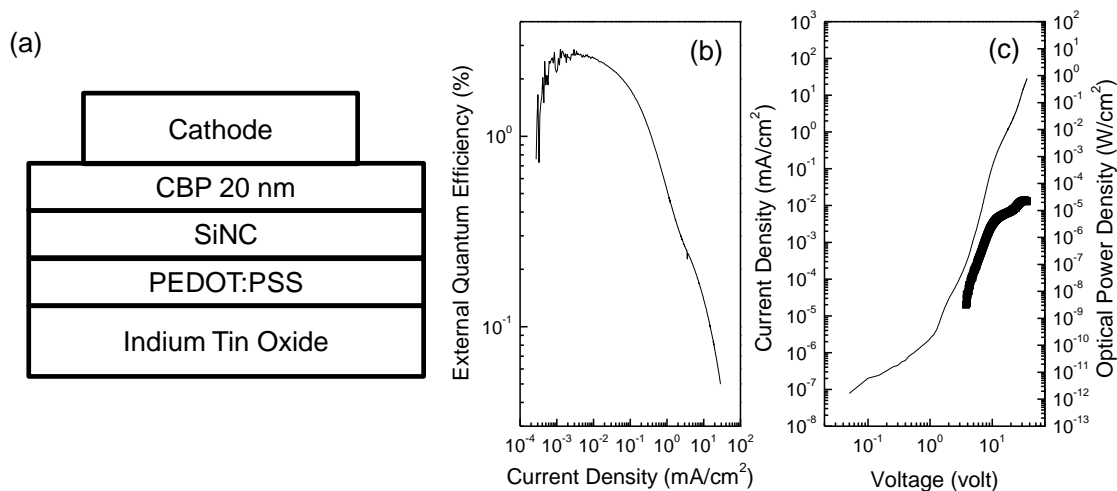
Figure 7.3 (a) Modified device for reversed-bias PL measurement, (b) external quantum efficiency and (c) current density-voltage and optical power density characteristics of the device in (a).
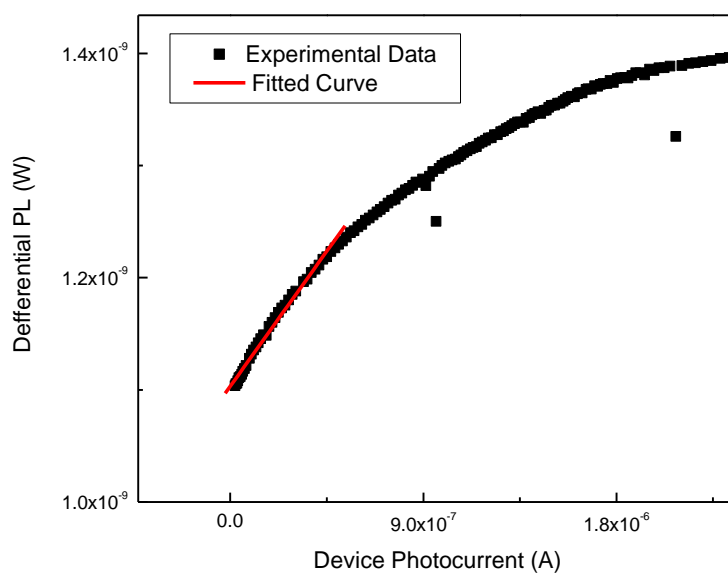
Figure 7.4 Preliminary result for the relationship between differential PL power and device photocurrent collected under the reversed bias. The slope of the fitted curve could potentially give out the value of out-coupled efficiency.

117

Table 7.1 Preliminary results for measuring the upper limit of the product between charge balance factor and the spin fraction factor for the available radiative exciton states. Note that the η_{EQE} is measured based on the same vertical geometry as shown in **Figure 7.1**.

External quantum efficiency in vertical setup	Out-coupled PL efficiency	Upper limit of $\chi \cdot \gamma$
0.0065%	0.018%	35%
0.01%	0.018%	56%

Although the preliminary estimation of $\chi \cdot \gamma$ is lower than the expected value (~1), the results remain interesting and indicate that more than 25% of the excitons would be allowed for radiative decay. This is promising for explaining the origin of the high efficiency of the SiNC-OLEDs, since not only the singlet but also the triplet excitons could undergo radiative recombination. Such emission mechanism is similar to the phosphorescent-OLED operation.[203, 204] However, the presented values of $\chi \cdot \gamma$ are still considerably low and it could originate from poor electron confinement (poor charge balance, $\gamma < 1$) in SiNCs since there is no electron-blocking layer to prevent electron leakage through the hole injection layer. Therefore, the next steps for precisely confirming $\chi \cdot \gamma$ relies on the following experimental improvement: first, to improve the optics for better light collection and consistent device power detection. Improved light harvesting could increase the signal intensity for accurate measurements. Second, find a wide-band-gap electron-blocking layer which is not absorbing at the laser excitation wavelength (405 nm). This additional layer could potentially confine the electrons within SiNCs and improve the device efficiency. As such, the charge balance factor would be closer to 1, revealing the true value of the spin statistics for the SiNC excitons. In addition, the preliminary results were measured with continuous wave illumination. The

discontinuity in slope of differential power-photocurrent due to leakage current is observed in dc PL measurement, which increases the noise in the photocurrent detection. In order to reduce the uncertainty and inconsistency of the measurements, lock-in amplifiers are required for monitoring the photocurrent and eliminating the noise signal in the collection of synchronous differential PL power and photocurrent.[207, 208]

The mechanism of the non-radiative exciton recombination in SiNC thin films is also the other key to understand the origin of the high-efficiency in SiNC-OLEDs. It is reported that SiNCs, in general, have longer PL lifetime[142, 209-212] (at the scale of tens of μs) than the typical direct band-gap semiconductor NCs[213] (at the scale of ns). Such long-lived excitons could have more opportunity to undergo the radiative recombination. However, the rates of radiative and non-radiative decay of excitons in ligand-passivated-SiNC thin films are still not well studied. The non-radiative recombination is usually associated and sensitive to the temperature change. More experiments in thin-film PL lifetime as a function of temperatures are required to understand the non-radiative recombination mechanisms.

7.2.2 Efficiency Roll-off in SiNCs

Although the high efficiency performance is observed in hybrid SiNC-OLEDs, the next-generation SiNC-OLEDs require high efficiency at higher applied current density in order to fulfill the high-power operation. In Figure 4.11, the device efficiency exhibits a decrease under the higher electrical excitation. To date, the origin of reduction still remains unknown. Further understanding of the mechanisms in the efficiency reduction is

very important for future material and device design of SiNC-OLEDs.

The first step is to identify whether the efficiency roll-off originates from the nature of the SiNCs. Interestingly, from Figure 7.5, the comparison of device efficiency among the full multi-layer device, device without ETL, and single-layer device (see Appendix) shows similar efficiency roll-off trend (slope) at higher applied current density. Such a result might suggest that efficiency roll-off has a weak dependence on the device structures. Therefore, the hypothesis could be made that the efficiency reduction stems from the intrinsic nature of SiNCs under high electrical excitation.
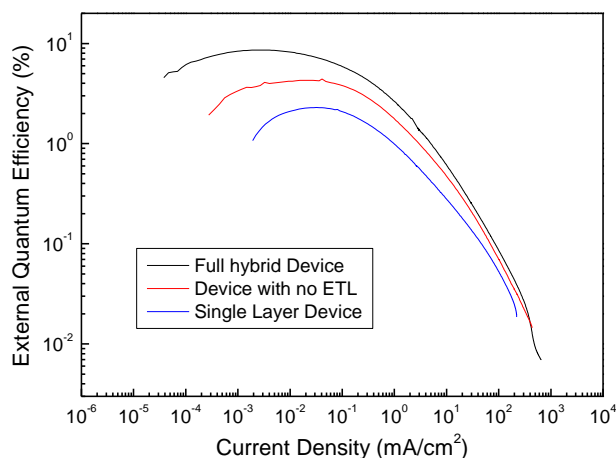
Figure 7.5 External quantum efficiency for the full structure hybrid SiNC-OLEDs, the device without ETL, and single-layer SiNC-LED.

Reineke et al. reported that the triplet-triplet annihilation (TTA), triplet-polaron quenching (TPQ), or field-induced triplet-exciton quenching could contribute to the efficiency decay process of phosphorescent OLEDs.[39, 214213] In the previous section, the preliminary result of reversed-bias PL demonstrates the possibility of triplet contribution to radiative recombination process. In addition, according to previous works, the lifetime of SiNCs has been reported in the time scale of micro-seconds. [142, 209-212] Such long-lived

excitons is similar to the triplet character and potentially possess similar annihilation processes as phosphorescent materials, leading to the efficiency roll-off during the SiNC-OLED operation. Therefore, the time-resolved measurement will be necessary for further investigation of TTA mechanism. According to the theory[39, 214], under the short-pulse laser excitation, the triplet exciton population could be expressed as a function of time:

$$L(t) = \frac{L(0)}{\{1 + [n_{ex}(0)]k_{TT}\tau/2\}e^{t/\tau} - [n_{ex}(0)]k_{TT}\tau/2} \tag{8.2}$$

, where L(t) is the luminescent intensity at time t, k_{TT} is the rate constant for TTA, t is the phosphorescent lifetime, $n_{ex}(0)$ is the concentration of the excited states. By measuring the different luminescent intensities as a function of time and knowing the initial exciton states, the TTA rate constant and the radiative lifetime could be determined from the experimental data.

On the contrary, the study of TPQ requires the information of charge-carrier density, trap states, and transport mechanisms for the construction of exciton rate equation.[39, 214] More investigation and experimental designs are required for understanding the charge transport within the SiNCs/device in order to confirm the validibility of TPQ study. As for the field-induced triplet quenching, the transient reversed-bias PL and transient EL measurements coupled with an oscilloscope are required for further realizing the behavior of the luminescence decay under the effect of electrical field.[39] Note that such transient EL is excited with the forward-bias pulse followed by a negative value while measuring the exciton decay under the applied electrical field. Figure 7.6 demonstrates the preliminary result of the transient EL measurement with hybrid SiNC-LEDs. The forward-bias pulse remains for 50 ns at 6.6 V and was switched to a reversed-bias at 1 V.

The decay lifetime is fitted as ~ 20 μsec with the single exponential decay model. However, more work is required to explore the field dependence of EL decay process, such as variation of the applied field during the decay process, and the adjustment of experimental setting to increase the signal-to-noise ratio and thus the measurement accuracy. Additional measurements of the temperature dependence will also be necessary for characterization of the kinetics as a function of temperature in all the exciton decay mechanisms.[215, 216]
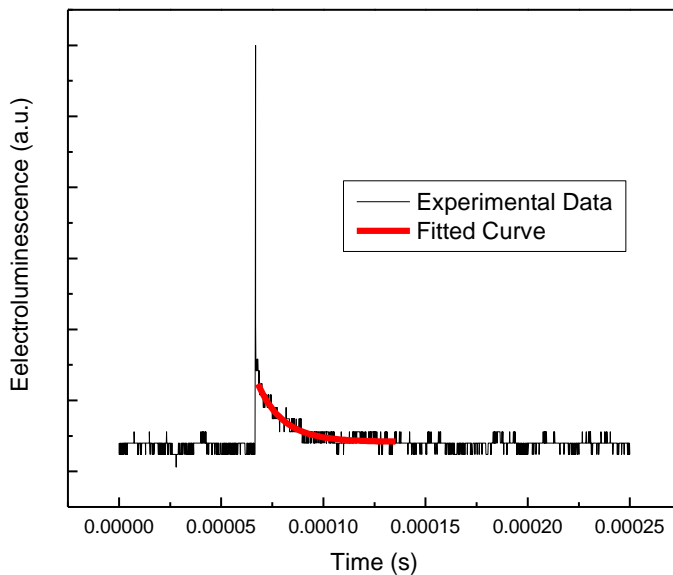
Figure 7.6 Preliminary result of the transient electroluminescence for the hybrid SiNC-OLEDs. The EL was excited by a forward-bias pulse at 6.6 V for 50 ns, followed by a reversed-bias voltage at -1 V during the decay process.

7.2.3 Device Performance Study through Surface Engineering of SiNCs: Ligand length and the Corresponding Coverage on SiNCs

Chapter 5 indicates the surface-ligand coverage plays an important role in the enhancement of charge confinement and hence the device performance. It is also

essential to study the device performance with the SiNCs containing different types of surface ligands. It is proposed that using conjugated ligands for II-VI NC passivation may increase the charge transport due to better electron coupling between NCs.[217, 218] As for SiNC passivation, conjugated ligand molecule has been proposed for improving the conductivity of SiNC thin films.[219, 220] However, if the conduction would likely occur only along the ligands, the charge injection into NCs or the charge confinement within NCs would be in questions, likely leading to poor device performance. In addition, careful ligand molecule selection is necessary to prevent any emission from the ligand molecules.

In the present work, alkene passivation with different lengths is proposed due to the well-developed surface hydrosilylation method developed by D. Jurberg et al.[147] and L. Mangolini et al.[220] Non-conjugated alkyl systems provide a simple route to control the charge transport mechanism as a function of the particle-to-particle distance. The analysis could allow the focus on charge transport in NCs. It is believed that the charge transport in the NC thin film is related to the distance between two particles. Therefore, switching the ligands from 1-dodecene to shorter alkyl chains might lower the barrier for charges to reach the SiNC surface, leading more charge carrier injection into the emitting materials. From the previous work, Bakueva et al. reported the improvement of EL efficiency by reducing the length from C_{18} ligands to C_8 ligands.[135] Table 7.2 summarizes the preliminary results of peak device efficiency from the SiNC-OLEDs containing ligands of 1-hexene, 1-dodecene, or 1-octadecene. (See Appendix) The longer ligands might separate the SiNCs for approx. >2nm away from each other, leading to insufficient

charge injection into SiNCs and inefficient charge transport which therefore result in poor device performance. It is expected that the charge injection would be improved by attaching the shorter ligands (approximately ~0.7 nm) on SiNCs. Surprisingly, from our preliminary attempt, the device performance was not enhanced by the usage of shorter ligands. Such poor device performance could originate from the lower PL efficiency of SiNCs. (Table 7.2) It is possible that the incomplete surface ligand coverage on SiNCs would lead to the surface defects and results in the reduction of the SiNC PL efficiency.[147, 200] Since similar reaction temperature in 1-dodecene surface reaction was adopted for 1-hexene hydrosilylation, it is likely that the low-boiling-point 1-hexene (b.p. ~ 64°C) escaped through the reactor during the high temperature process (~ 200-215°C). As such, excess 1-hexene in the reaction solution is required in order to obtain high reaction yield, or consecutive double-phase passivation (gas phase and liquid phase) is necessary to increase the degree of passivation of 1-hexene ligands. In addition, more device studies and TGA measurements should be coupled with the reaction study in order to optimize the surface ligand coverage for high device efficiency. Therefore, by

Table 7.2 Summary of the preliminary performance for the device using SiNC with different surface ligands.

Ligand Name	Structure	Solution PL efficiency	Preliminary Device Efficiency
1-hexene	H_3C-$(CH_2)_3$-$CH=CH_2$	12%*	1.5%
1-dodecene	H_3C-$(CH_2)_9$-$CH=CH_2$	45%	8.6%
1-octadecene	H_3C-$(CH_2)_{15}$-$CH=CH_2$	35%	0.3%

* Through gas-phase passivation with post-annealing in mestylene.

systematically varying the ligand length, a thorough understanding of charge transport as a function of ligand length could be obtained, which would be benefical for futher device performance optimization.

7.2.4 Charge Transport Mechanisms in SiNCs

In the previous studies[221], it has been proposed that the space charge limited current and tunneling mechanism were responsible for the charge conduction among the SiNCs prepared by the pulsed laser ablation. To date, very few studies have been reported to elucidate the impact of ligands on the transport in thin films made from colloidal SiNCs.[222] As discussed in Chapter 5, the surface ligand plays a significant role in determining the electrical transport within SiNCs and thus the device performance. The device current and performance has a strong dependence on the surface ligand coverage on SiNCs. In addition, from the previous section, different type of ligands on SiNCs could also lead to different device performance. As such, it is very likely that the ligand coverage and ligand length would significantly affect the charge injection due to the distance between particles and the energy barrier created by the ligands.[217, 218] Therefore, systematic study on the effect of ligand coverage and length on charge transport has important implications for understanding the transport mechanism within SiNC thin films, and thus provides effective ways to formulate strategies for device optimization. The proposed future research direction will lie in the investigation of conductivity and mobility as a function of surface ligand coverage and ligand length. Such study relies on the temperature dependence measurements on the single-carrier devices with different

ligand design. Furthermore, it has been reported that the size of the NCs could also affect the aforementioned charge transport properties in CdSe and PbSe thin films.[223, 224] Similarly, recent theoretical study[225] and experimental research[226] demonstrated that charge injection and transport in SiNCs possess a size dependence relationship. The investigation of the size dependence of charge injection and transport would also provide additional dimension for understanding the fundamental physics in electrical-operation mechanism in SiNC thin films.

7.2.5 Visible Electroluminescence from SiNC-OLEDs and Device Lifetime

This work has demonstrated the highly-efficient SiNC-OLEDs with near infrared (IR) and red emission. The ultimate goal of this work is to realize the full-color EL emission and to increase the device lifetime. Recent works have already realized the full-spectrum PL emission from colloidal SiNCs. Those particles contain surface ligands with high solubility in either organic or aqueous solvents, providing more flexibility for solution processing in device fabrication. The reported PL and the corresponding particle size are summarized in Table 7.3.[147, 211, 227-239] Since different emission wavelength can be produced by controlling the size of the nanocrysals, it is possible to realize the high efficiency SiNC-OLEDs in red, green, blue or white color through the careful device design and selection of organic transport materials for charge/exciton confinement.

Although the robust EL from SiNCs has already been demonstrated in this work, more investigation is still required for understanding the device lifetime under a different emission wavelength (particle size). Longer operational hours are necessary for realizing

126

the ultimate application of SiNC-OLED in future displays and lighting. Therefore, selecting multiple testing conditions including various temperatures and applied current densities, and setting up the suitable testing equipment are essential for device lifetime study.

Table 7.3 Summary of recent research in colloidal SiNCs with tunable emission as a function of nanocrystal size.

Wavelength (nm)	Ligand	Solution PL Efficiency	Size (nm)	Year
283	Alkyl Group	13-22%	1.6	2008
310	Alkyl Group	-	1	2006
313	Alkyl Group	20%	1.8	2010
335	Alkyl Group	-	1.8	2005
340-350	Alkyl Group	-	2-5	1999
360	Alkyl Group	11%	2-4	2010
455	Bare in DSMO	-	2-5	2012
456	Alkyl Group	-	2	2009
570	Alkyl Group	20%	2-3	2010
650	Alkyl Group	-	5	2005
665	Alkyl Group	7-19%	2.6	2008
718	Alkyl Group	8%	2.7	2012
760	Allylbenzene	43%	2-5	2012
789	Alkyl Group	60%	3	2006
860	Alkyl Group	45%	5	2009

7.2.6 Afterword

Hybrid inorganic nanocrystal-organic light-emitting devices integrate the advantages

127

of both inorganic and organic materials, allowing simple material synthesis route to obtain different wavelengthes and low-cost solution processes for device manufacture. A close look at the evolution of device external quantum efficiency over the past decade reveals a significant breakthrough from 0.001%[11, 13, 15, 16, 115, 125, 240] to 8.6%[199] to date (Figure 7.7 (a)). In this work, by exploring SiNC-based NC-OLEDs, a deeper understanding of device physics is obtained, which enables the realization of robust devices with the highest EQE to date as shown in Figure 7.7 (b).[11, 15, 16, 125, 178, 199, 240] Such novel device architectures exploiting the novel Si-based emitter could open another opportunity for the next-generation LED and display technology. More research is needed to be done to better understand the fundamental SiNC photo physics and the charge transport mechanism, and to realize of long-lifetime device performance for future commercialization of full-color-emission optoelectronics.
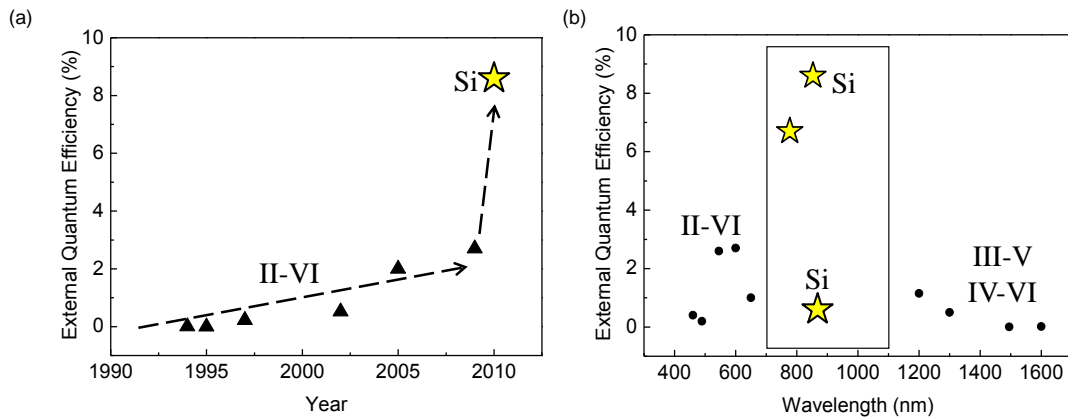

Figure 7.7 (a) Evolution of NC-OLED efficiency over the past decade, (b) Comparison of device efficiency as a function of wavelength. The close box indicates the near infrared region where fewer studies of NC-OLEDs were performed.

References

1. U.S. Department of Energy. Energy Efficiency of White LEDs. (2009).

2. Johnson, J. The end of the light bulb. *Chem. Eng. News* **85**, 46-51 (2007).

3. So, F., Kido, J. & Burrows, P. Organic light-emitting devices for solid-state lighting. *MRS Bull.* **33**, 663-669 (2008).

4. Round, H. J. A note on carborundum. *Electr. World* **49**, 308 (1907).

5. Schubert, E. F. in *Light-Emitting Diodes* 432 (Cambridge University Press, New York, 2006).

6. Taniyasu, Y., Kasu, M. & Makimoto, T. An aluminium nitride light-emitting diode with a wavelength of 210 nanometres. *Nature* **441**, 325-328 (2006).

7. Joray, R., Stanley, R. P. & Ilegems, M. High efficiency planar MCLEDs. *Phys. Status Solidi B-Basic Solid State Phys.* **242**, 2315-2325 (2005).

8. Tang, C. W. & Vanslyke, S. A. Organic Electroluminescent Diodes. *Appl. Phys. Lett.* **51**, 913-915 (1987).

9. Baldo, M. *et al*. Highly efficient phosphorescent emission from organic electroluminescent devices. *Nature* **395**, 151-154 (1998).

10. Adachi, C., Baldo, M., Thompson, M. & Forrest, S. Nearly 100% internal phosphorescence efficiency in an organic light-emitting device. *J. Appl. Phys.* **90**, 5048-5051 (2001).

11. Talapin, D. V., Lee, J., Kovalenko, M. V. & Shevchenko, E. V. Prospects of Colloidal Nanocrystals for Electronic and Optoelectronic Applications. *Chem. Rev.* **110**, 389-458 (2010).

12. Wood, V. & Bulovic, V. Colloidal quantum dot light-emitting devices. *Nano Rev.* **1**, 5202 (2010).

13. Colvin, V. L., Schlamp, M. C. & Alivisatos, A. P. Light-emitting-diodes made from cadmium selenide nanocrystals and a semiconducting polymer. *Nature* **370**, 354-357 (1994).

14. Coe, S., Woo, W. K., Bawendi, M. & Bulovic, V. Electroluminescence from single monolayers of nanocrystals in molecular organic devices. *Nature* **420**, 800-803 (2002).

15. Anikeeva, P. O., Halpert, J. E., Bawendi, M. G. & Bulovic, V. Quantum Dot Light-Emitting Devices with Electroluminescence Tunable over the Entire Visible Spectrum. *Nano Lett.* **9**, 2532-2536 (2009).

16. Steckel, J. S., Coe-Sullivan, S., Bulovic, V. & Bawendi, M. G. 1.3 μm to 1.55 μm Tunable Electroluminescence from PbSe Quantum Dots Embedded within an Organic Device. *Adv. Mater.* **15**, 1862-1866 (2003).

17. Hiemenz, P. C. & Rajagopalan, R. in *Principles of Colloid and Surface Chemistry, 3rd ed.* (CRC, New York, 1997).

18. Silinsh, E. A. & Capek, V. in *Organic Molecular Crystals: Interaction, Localization, and Transport Phenomena* (American Institute of Physics, New York, 1994).

19. Zumdahl, S. S. in *Chemical Principles* (Houghton Mifflin Company, New York, 1998).

20. Hufner, S. in *Photoelectron Spectroscopy, 3rd ed.* (Springer, Berlin, 2003).

21. Ishii, H., Sugiyama, K., Ito, E. & Seki, K. Energy level alignment and interfacial electronic structures at organic metal and organic organic interfaces. *Adv. Mater.* **11**, 605-625 (1999).

22. Hung, L. S. & Chen, C. H. Recent progress of molecular organic electroluminescent materials and devices. *Mater. Sci. Eng. R-Rep.* **39**, 143-222 (2002).

23. Liu, Y., Liu, M. & Jen, A. Synthesis and characterization of a novel and highly efficient light-emitting polymer. *Acta Polym.* **50**, 105-108 (1999).

24. Pope, M. & Swenberg, C. E. Electronic Process in Organic Crystals And Polymers. (1999).

25. Knupfer, M. Exciton binding energies in organic semiconductors. *Appl. Phys. A-Mater. Sci. Process.* **77**, 623-626 (2003).

26. Sze, S. M. in *Physics of Semiconductor Devices, 2nd ed.* (Wiley Inter-Science, New York, 1981).

27. Scholes, G. D. & Rumbles, G. Excitons in nanoscale systems. *Nat. Mater.* **5**, 683-696 (2006).

28. Kohler, A., Wilson, J. & Friend, R. Fluorescence and phosphorescence in organic materials. *Adv. Mater.* **14**, 701-707 (2002).

29. Wohlgenannt, M. & Vardeny, Z. Spin-dependent exciton formation rates in pi-conjugated materials. *J. Phys. -Condes. Matter.* **15**, R83-R107 (2003).

30. Kohler, A. & Wilson, J. Phosphorescence and spin-dependent exciton formation in conjugated polymers. *Org. Electron.* **4**, 179-189 (2003).

31. Baldo, M., O'Brien, D., Thompson, M. & Forrest, S. Excitonic singlet-triplet ratio in a semiconducting organic thin film. *Phys. Rev. B* **60**, 14422-14428 (1999).

32. Segal, M., Baldo, M., Holmes, R., Forrest, S. & Soos, Z. Excitonic singlet-triplet ratios in molecular and polymeric organic materials. *Phys. Rev. B* **68**, 075211 (2003).

33. Wilson, J. *et al*. Spin-dependent exciton formation in pi-conjugated compounds. *Nature* **413**, 828-831 (2001).

34. Reufer, M. *et al*. Spin-conserving carrier recombination in conjugated polymers. *Nat. Mater.* **4**, 340-346 (2005).

35. Turro, N. J. in *Modern Molecular Photochemistry* (University Science Books, Sausalito, 1991).

36. Patel, N. K., Cina, S. & Burroughes, J. H. High-efficiency organic light-emitting diodes. *IEEE J. Sel. Top. Quantum Electron.* **8**, 346-361 (2002).

37. Lakowicz, J. R. in *Principles of Fluorescence Spectroscopy* (Plenum Press, New York, 1983).

38. Klan, P. & Wirz, J. in *Photochemistry of Organic Compounds: From Concepts to Practice* (John Wiley & Sons Ltd., Chichester, United Kingdom, 2009).

39. Reineke, S., Walzer, K. & Leo, K. Triplet-exciton quenching in organic phosphorescent light-emitting diodes with Ir-based emitters. *Phys. Rev. B* **75**, 125328 (2007).

40. Lamansky, S. *et al*. Highly phosphorescent bis-cyclometalated iridium complexes: Synthesis, photophysical characterization, and use in organic light emitting diodes. *J. Am. Chem. Soc.* **123**, 4304-4312 (2001).

41. Wong, W. & Ho, C. Heavy metal organometallic electrophosphors derived from multi-component chromophores. *Coord. Chem. Rev.* **253**, 1709-1758 (2009).

42. Baldo, M., Thompson, M. & Forrest, S. High-efficiency fluorescent organic light-emitting devices using a phosphorescent sensitizer. *Nature* **403**, 750-753 (2000).

43. Főrster, T. 10th Spiers Memorial Lecture. Transfer mechanisms of electronic excitation. **27**, 7 (1959).

44. Kao, K. C. & Hwang, W. in *Electrical Transport in Solids with Particular Reference to Organic Semiconductors* (Pergamon Press, New York, 1981).

45. Dexter, D. L. A Theory of Sensitized Luminescence in Solids. *J. Chem. Phys.* **21**, 836 (1953).

46. Pierret, R. F. in *Advanced Semiconductor Fundamentals, 2nd ed.* (Pearson Education, iNC., Upper Saddle River, New Jersey, 2003).

47. Kepler, R. G. Charge Carrier Production and Mobility in Anthracene Crystals. *Phys. Rev.* **119**, 1226-1229 (1960).

48. Chen, B. *et al*. Improved time-of-flight technique for measuring carrier mobility in thin films of organic electroluminescent materials. *Jpn. J. Appl. Phys. Part 1 - Regul. Pap. Short Notes Rev. Pap.* **39**, 1190-1192 (2000).

49. Coropceanu, V. *et al*. Charge transport in organic semiconductors. *Chem. Rev.* **107**, 926-952 (2007).

50. Tiwari, S. & Greenham, N. C. Charge mobility measurement techniques in organic semiconductors. *Opt. Quant. Electron.* **41**, 69-89 (2009).

51. Ye, J., Chen, H., Shi, M. & Wang, M. Recent development of organic electron transport materials. *Prog. Nat. Sci.* **13**, 81-87 (2003).

52. Pinotti, E., Sassella, A., Borghesi, A. & Tubino, R. Electrical characterization of organic semiconductors by transient current methods. *Synth. Met.* **122**, 169-171 (2001).

53. Horowitz, G. Organic field-effect transistors. *Adv. Mater.* **10**, 365-377 (1998).

54. DODABALAPUR, A., TORSI, L. & KATZ, H. Organic Transistors - 2-Dimensional Transport and Improved Electrical Characteristics. *Science* **268**, 270-271 (1995).

55. Horowitz, G. Organic thin film transistors: From theory to real devices. *J. Mater. Res.* **19**, 1946-1962 (2004).

56. P, N. M. Theory of space-charge-limited current enhanced by Frenkel effect. *J. Phys. D* **3**, 151 (1970).

57. Frenkel, J. On Pre-Breakdown Phenomena in Insulators and Electronic Semi-Conductors. *Phys. Rev.* **54**, 647-648 (1938).

58. Shirota, Y. Organic materials for electronic and optoelectronic devices. *J. Mater. Chem.* **10**, 1-25 (2000).

59. Kulkarni, A., Tonzola, C., Babel, A. & Jenekhe, S. Electron transport materials for organic light-emitting diodes. *Chem. Mat.* **16**, 4556-4573 (2004).

60. Menard, E. *et al*. High-performance n- and p-type single-crystal organic transistors with free-space gate dielectrics. *Adv. Mater.* **16**, 2097-2101 (2004).

61. Kittel, C. in *Introduction to Solid State Physics 8th ed.* (John Wiley & Sons, Inc., Hoboken, New Jersey, 2005).

62. Pope, M., Kallmann, H. & Magnante, P. Electroluminescence in Organic Crystals. *J. Chem. Phys.* **38**, 2042 (1963).

63. Helfrich, W. & Schneidere, W. G. Recombination Radiation in Anthracene Crystals. *Phys. Rev. Lett.* **14**, 229 (1965).

64. Williams, D. F. & Schadt, M. dc and Pulsed Electroluminescence in Anthracene and Doped Anthracene Crystals. *J. Chem. Phys.* **53**, 3480 (1970).

65. Vincett, P. S., Barlow, W. A., Hann, R. A. & Roberts, G. G. Electrical-Conduction and Low-Voltage Blue Electro-Luminescence in Vacuum-Deposited Organic Films. *Thin Solid Films* **94**, 171-183 (1982).

66. Kampas, F. J. & Gouterman, M. Porphyrin Films - Electroluminescence of Octaethylporphin. *Chem. Phys. Lett.* **48**, 233-236 (1977).

67. Kalinowski, J., Godlewski, J. & Dreger, Z. High-Field Recombination Electroluminescence in Vacuum-Deposited Anthracene and Doped Anthracene Films. *Appl. Phys. A-Mater. Sci. Process.* **37**, 179-186 (1985).

68. Burroughes, J. H. *et al*. Light-Emitting-Diodes Based on Conjugated Polymers. *Nature* **347**, 539-541 (1990).

69. Tang, C. W., Vanslyke, S. A. & Chen, C. H. Electroluminescence of Doped Organic Thin-Films. *J. Appl. Phys.* **65**, 3610-3616 (1989).

70. Hung, L. & Chen, C. Recent progress of molecular organic electroluminescent materials and devices. *Mater. Sci. Eng. R-Rep.* **39**, 143-222 (2002).

71. Tsutsui, T. Progress in electroluminescent devices using molecular thin films. *MRS Bull.* **22**, 39-45 (1997).

72. Greenham, N. C., Friend, R. H. & Bradley, D. D. C. Angular Dependence of the Emission from a Conjugated Polymer Light-Emitting Diode: Implications for Efficiency Calculations. *Adv. Mater.* **6**, 491-494 (1994).

73. Erickson, N. C. & Holmes, R. J. Highly efficient, single-layer organic light-emitting devices based on a graded-composition emissive layer. *Appl. Phys. Lett.* **97**, 083308 (2010).

74. Erickson, N. C. & Holmes, R. J. Relating charge transport and performance in single-layer graded-composition organic light-emitting devices. *J. Appl. Phys.* **110**, 084515 (2011).

75. Wu, H., Ying, L., Yang, W. & Cao, Y. Progress and perspective of polymer white light-emitting devices and materials. *Chem. Soc. Rev.* **38**, 3391-3400 (2009).

76. Kido, J., Kimura, M. & Nagai, K. Multilayer White Light-Emitting Organic Electroluminescent Device. *Science* **267**, 1332-1334 (1995).

77. D'Andrade, B. & Forrest, S. White organic light-emitting devices for solid-state lighting. *Adv. Mater.* **16**, 1585-1595 (2004).

78. Misra, A., Kumar, P., Kamalasanan, M. N. & Chandra, S. White organic LEDs and their recent advancements. *Semiconductor Sci. Technol.* **21**, R35-R47 (2006).

79. Yin, Y. *et al*. High-efficiency and low-efficiency-roll-off single-layer white organic light-emitting devices with a bipolar transport host. *Appl. Phys. Lett.* **101**, 063306 (2012).

80. Murray, C. B., Norris, D. J. & Bawendi, M. G. Synthesis and characterization of nearly monodisperse CdE (E = sulfur, selenium, tellurium) semiconductor nanocrystallites. *J. Am. Chem. Soc.* **115**, 8706-8715 (1993).

81. Dabbousi, B. O. *et al*. (CdSe)ZnS Core-Shell Quantum Dots: Synthesis and Characterization of a Size Series of Highly Luminescent Nanocrystallites. *J. Phys. Chem. B* **101**, 9463-9475 (1997).

82. Nature Phtonics Editorial. The rise of colloidal quantum dots. *Nat. Photon.* **3**, 305-305 (2009).

83. Graham-Rowe, D. From dots to devices. *Nat. Photon.* **3**, 307-309 (2009).

84. Coe-Sullivan, S. Optoelectronics: Quantum dot developments. *Nat. Photon.* **3**, 315-316 (2009).

85. Tessler, N., Medvedev, V., Kazes, M., Kan, S. H. & Banin, U. Efficient near-infrared polymer nanocrystat light-emitting diodes. *Science* **295**, 1506-1508 (2002).

86. McDonald, S. A. *et al*. Solution-processed PbS quantum dot infrared photodetectors and photovoltaics. *Nat. Mater.* **4**, 138-U14 (2005).

87. Robel, I., Subramanian, V., Kuno, M. & Kamat, P. V. Quantum dot solar cells. Harvesting light energy with CdSe nanocrystals molecularly linked to mesoscopic TiO2 films. *J. Am. Chem. Soc.* **128**, 2385-2393 (2006).

88. Kamat, P. V. Quantum Dot Solar Cells. Semiconductor Nanocrystals as Light Harvesters. *J. Phys. Chem. C* **112**, 18737-18753 (2008).

89. Jamieson, T. *et al*. Biological applications of quantum dots. *Biomaterials* **28**, 4717-4732 (2007).

90. Chan, W. C. W. & Nie, S. M. Quantum dot bioconjugates for ultrasensitive nonisotopic detection. *Science* **281**, 2016-2018 (1998).

91. Weissleder, R. A clearer vision for in vivo imaging. *Nat. Biotechnol.* **19**, 316-317 (2001).

92. Kim, S. *et al*. Near-infrared fluorescent type II quantum dots for sentinel lymph node mapping. *Nat. Biotechnol.* **22**, 93-97 (2004).

93. Michalet, X. *et al*. Quantum dots for live cells, in vivo imaging, and diagnostics. *Science* **307**, 538-544 (2005).

94. Lim, Y. T. *et al*. Selection of quantum dot wavelengths for biomedical assays and imaging. *Molecular imaging* **2**, 50-64 (2003).

95. Smith, A. M., Gao, X. H. & Nie, S. M. Quantum dot nanocrystals for in vivo molecular and cellular imaging. *Photochem. Photobiol.* **80**, 377-385 (2004).

96. Norris, D. J. in *Semiconductor and Metal Nanocrystals* (ed Klimov, V. I.,) (Marcel Dekker Inc., New York, 2004).

97. Yoffe, A. D. Low-dimensional systems: quantum size effects and electronic properties of semiconductor microcrystallites (zero-dimensional systems) and some quasi-two-dimensional systems. *Adv. Phys.* **51**, 799-890 (2002).

98. Beard, M. C. *et al*. Multiple exciton generation in colloidal silicon nanocrystals. *Nano Lett.* **7**, 2506-2512 (2007).

99. Alivisatos, A. P. Perspectives on the physical chemistry of semiconductor nanocrystals. *J. Phys. Chem.* **100**, 13226-13239 (1996).

100. Kippeny, T., Swafford, L. A. & Rosenthal, S. J. Semiconductor nanocrystals: A powerful visual aid for introducing the particle in a box. *J. Chem. Educ.* **79**, 1094-1100 (2002).

101. Brus, L. E. A Simple-Model for the Ionization-Potential, Electron-Affinity, and Aqueous Redox Potentials of Small Semiconductor Crystallites. *J. Chem. Phys.* **79**, 5566-5571 (1983).

102. Brus, L. E. Electron Electron and Electron-Hole Interactions in Small Semiconductor Crystallites - the Size Dependence of the Lowest Excited Electronic State. *J. Chem. Phys.* **80**, 4403-4409 (1984).

103. Bawendi, M. G., Steigerwald, M. L. & Brus, L. E. The Quantum-Mechanics of Larger Semiconductor Clusters (Quantum Dots). *Annu. Rev. Phys. Chem.* **41**, 477-496 (1990).

104. Baskoutas, S. & Terzis, A. F. Size-dependent band gap of colloidal quantum dots. *J. Appl. Phys.* **99**, 013708 (2006).

105. Iyer, S. S. & Xie, Y. H. Light-Emission from Silicon. *Science* **260**, 40-46 (1993).

106. Gorokhov, E. B. *et al*. Effect of quantum confinement on optical properties of Ge nanocrystals in GeO2 films. *Semiconductors* **39**, 1168-1175 (2005).

107. Brus, L. Luminescence of Silicon Materials - Chains, Sheets, Nanocrystals, Nanowires, Microcrystals, and Porous Silicon. *J. Phys. Chem.* **98**, 3575-3581 (1994).

108. Takagahara, T. & Takeda, K. Theory of the Quantum Confinement Effect on Excitons in Quantum Dots of Indirect-Gap Materials. *Phys. Rev. B* **46**, 15578-15581 (1992).

109. Kershaw, S. V., Harrison, M. T. & Burt, M. G. Putting nanocrystals to work: from solutions to devices. *Philos. Trans. R. Soc. Lond. Ser. A-Math. Phys. Eng. Sci.* **361**, 331-340 (2003).

110. Talapin, D. V. *et al*. CdSe/CdS/ZnS and CdSe/ZnSe/ZnS core-shell-shell nanocrystals. *J. Phys. Chem. B* **108**, 18826-18831 (2004).

111. Holmes, R. J. *et al*. Blue organic electrophosphorescence using exothermic host-guest energy transfer. *Appl. Phys. Lett.* **82**, 2422-2424 (2003).

112. Holmes, R. J. *et al*. Efficient, deep-blue organic electrophosphorescence by guest charge trapping. *Appl. Phys. Lett.* **83**, 3818-3820 (2003).

113. Ren, X. F. *et al*. Ultrahigh energy gap hosts in deep blue organic electrophosphorescent devices. *Chem. Mat.* **16**, 4743-4747 (2004).

114. Panzer, M. J., Wood, V., Geyer, S. M., Bawendi, M. G. & Bulovic, V. Tunable Infrared Emission From Printed Colloidal Quantum Dot/Polymer Composite Films on Flexible Substrates. *J. Disp. Technol.* **6**, 90-93 (2010).

115. Haverinen, H. M., Myllyla, R. A. & Jabbour, G. E. Inkjet printing of light emitting quantum dots. *Appl. Phys. Lett.* **94**, 073108 (2009).

116. Wood, V. *et al*. Inkjet-Printed Quantum Dot-Polymer Composites for Full-Color AC-Driven Displays. *Adv. Mater.* **21**, 2151-2155 (2009).

117. Cho, K. *et al*. High-performance crosslinked colloidal quantum-dot light-emitting diodes. *Nat. Photon.* **3**, 341-345 (2009).

118. Qian, L., Zheng, Y., Xue, J. & Holloway, P. H. Stable and efficient quantum-dot light-emitting diodes based on solution-processed multilayer structures. *Nat. Photon.* **5**, 543-548 (2011).

119. Kwak, J. *et al*. Bright and Efficient Full-Color Colloidal Quantum Dot Light-Emitting Diodes Using an Inverted Device Structure. *Nano Lett.* **12**, 2362-2366 (2012).

120. Ma, X., Xu, F., Benavides, J. & Cloutier, S. G. High performance hybrid near-infrared LEDs using benzenedithiol cross-linked PbS colloidal nanocrystals. *Org. Electron.* **13**, 525-531 (2012).

121. Sun, L. *et al*. Bright infrared quantum-dot light-emitting diodes through inter-dot spacing control. *Nat. Nanotechnol.* **7**, 369-373 (2012).

122. Dabbousi, B. O., Bawendi, M. G., Onitsuka, O. & Rubner, M. F. Electroluminescence from CdSe quantum-dot/polymer composites. *Appl. Phys. Lett.* **66**, 1316-1318 (1995).

123. Konstantatos, G., Huang, C. J., Levina, L., Lu, Z. H. & Sargent, E. H. Efficient Infrared Electroluminescent Devices Using Solution-Processed Colloidal Quantum Dots. *Adv. Func. Mat.* **15**, 1865-1869 (2005).

124. Zhao, J. L. *et al*. Efficient CdSe/CdS Quantum Dot Light-Emitting Diodes Using a Thermally Polymerized Hole Transport Layer. *Nano Lett.* **6**, 463-467 (2006).

125. Anikeeva, P. O., Halpert, J. E., Bawendi, M. G. & Bulovic, V. Electroluminescence from a Mixed Red-Green-Blue Colloidal Quantum Dot Monolayer. *Nano Lett.* **7**, 2196-2200 (2007).

126. Sun, Q. *et al*. Bright, multicoloured light-emitting diodes based on quantum dots. *Nat. Photon.* **1**, 717-722 (2007).

127. Bourdakos, K. N., Dissanayake, D. M. N. M., Lutz, T., Silva, S. R. P. & Curry, R. J. Highly efficient near-infrared hybrid organic-inorganic nanocrystal electroluminescence device. *Appl. Phys. Lett.* **92**, 153311 (2008).

128. Coe-Sullivan, S., Steckel, J. S., Woo, W. K., Bawendi, M. G. & Bulovic, V. Large-area ordered quantum-dot monolayers via phase separation during spin-casting. *Adv. Funct. Mater.* **15**, 1117-1124 (2005).

129. Li, Y. Q. *et al*. White organic light-emitting devices with CdSe/ZnS quantum dots as a red emitter. *J. Appl. Phys.* **97**, 113501 (2005).

130. Caruge, J., Halpert, J. E., Bulovic, V. & Bawendi, M. G. NiO as an inorganic hole-transporting layer in quantum-dot light-emitting devices. *Nano Lett.* **6**, 2991-2994 (2006).

131. Caruge, J. M., Halpert, J. E., Wood, V., Bulovic, V. & Bawendi, M. G. Colloidal quantum-dot light-emitting diodes with metal-oxide charge transport layers. *Nat. Photon.* **2**, 247-250 (2008).

132. Wood, V. *et al*. Selection of Metal Oxide Charge Transport Layers for Colloidal Quantum Dot LEDs. *ACS Nano* **3**, 3581-3586 (2009).

133. Wood, V., Halpert, J. E., Panzer, M. J., Bawendi, M. G. & Bulovic, V. Alternating Current Driven Electroluminescence from ZnSe/ZnS:Mn/ZnS Nanocrystals. *Nano Lett.* **9**, 2367-2371 (2009).

134. Wood, V. *et al*. Air-Stable Operation of Transparent, Colloidal Quantum Dot Based LEDs with a Unipolar Device Architecture. *Nano Lett.* **10**, 24-29 (2010).

135. Bakueva, L. *et al*. Size-tunable infrared (1000-1600 nm) electroluminescence from PbS quantum-dot nanocrystals in a semiconducting polymer. *Appl. Phys. Lett.* **82**, 2895-2897 (2003).

136. Solomeshch, O. *et al*. Optoelectronic properties of polymer-nanocrystal composites active at near-infrared wavelengths. *J. Appl. Phys.* **98**, 074310 (2005).

137. Sargent, E. H. Infrared quantum dots. *Adv. Mater.* **17**, 515-522 (2005).

138. Rogach, A. L., Eychmuller, A., Hickey, S. G. & Kershaw, S. V. Infrared-emitting colloidal nanocrystals: Synthesis, assembly, spectroscopy, and applications. *Small* **3**, 536-557 (2007).

139. Nirmal, M. & Brus, L. Luminescence photophysics in semiconductor nanocrystals. *Acc. Chem. Res.* **32**, 407-414 (1999).

140. Canham, L. T. Silicon Quantum Wire Array Fabrication by Electrochemical and Chemical Dissolution of Wafers. *Appl. Phys. Lett.* **57**, 1046-1048 (1990).

141. Canham, L. Gaining light from silicon. *Nature* **408**, 411-412 (2000).

142. Wilson, W. L., Szajowski, P. F. & Brus, L. E. Quantum Confinement in Size-Selected, Surface-Oxidized Silicon Nanocrystals. *Science* **262**, 1242-1244 (1993).

143. Littau, K. A., Szajowski, P. J., Muller, A. J., Kortan, A. R. & Brus, L. E. A Luminescent Silicon Nanocrystal Colloid Via a High-Temperature Aerosol Reaction. *J. Phys. Chem.* **97**, 1224-1230 (1993).

144. Hirschman, K. D., Tsybeskov, L., Duttagupta, S. P. & Fauchet, P. M. Silicon-based visible light-emitting devices integrated into microelectronic circuits. *Nature* **384**, 338-341 (1996).

145. Wilcoxon, J. P. & Samara, G. A. Tailorable, visible light emission from silicon nanocrystals. *Appl. Phys. Lett.* **74**, 3164-3166 (1999).

146. Wilcoxon, J. P., Samara, G. A. & Provencio, P. N. Optical and electronic properties of Si nanoclusters synthesized in inverse micelles. *Phys. Rev. B* **60**, 2704-2714 (1999).

147. Jurbergs, D., Rogojina, E., Mangolini, L. & Kortshagen, U. Silicon nanocrystals with ensemble quantum yields exceeding 60%. *Appl. Phys. Lett.* **88**, 233116 (2006).

148. Heinrich, J. L., Curtis, C. L., Credo, G. M., Kavanagh, K. L. & Sailor, M. J. Luminescent Colloidal Silicon Suspensions from Porous Silicon. *Science* **255**, 66-68 (1992).

149. Nayfeh, O. M., Antoniadis, D. A., Mantey, K. & Nayfeh, M. H. Uniform delivery of silicon nanoparticles on device quality substrates using spin coating from isopropyl alcohol colloids. *Appl. Phys. Lett.* **94**, 043112 (2009).

150. Hai, N. H., Grigoriants, I. & Gedanken, A. Converting Stober Silica and Mediterranean Sand to High Surface Area Silicon by a Reaction under Autogenic Pressure at Elevated Temperatures. *J. Phys. Chem. C* **113**, 10521-10526 (2009).

151. Sato, K., Tsuji, H., Hirakuri, K., Fukata, N. & Yamauchi, Y. Controlled chemical etching for silicon nanocrystals with wavelength-tunable photoluminescence. *Chem. Commun.*, 3759-3761 (2009).

152. Heath, J. R. A Liquid-Solution-Phase Synthesis of Crystalline Silicon. *Science* **258**, 1131-1133 (1992).

153. Bley, R. A. & Kauzlarich, S. M. A low-temperature solution phase route for the synthesis of silicon nanoclusters. *J. Am. Chem. Soc.* **118**, 12461-12462 (1996).

154. Ledoux, G., Gong, J. & Huisken, F. Effect of passivation and aging on the photoluminescence of silicon nanocrystals. *Appl. Phys. Lett.* **79**, 4028-4030 (2001).

155. Li, X. G., He, Y. Q., Talukdar, S. S. & Swihart, M. T. Process for preparing macroscopic quantities of brightly photoluminescent silicon nanoparticles with emission spanning the visible spectrum. *Langmuir* **19**, 8490-8496 (2003).

156. Liu, S. M., Yang, Y., Sato, S. & Kimura, K. Enhanced photoluminescence from Si nano-organosols by functionalization with alkenes and their size evolution. *Chemistry of Materials* **18**, 637-642 (2006).

157. Hua, F. J., Erogbogbo, F., Swihart, M. T. & Ruckenstein, E. Organically capped silicon nanoparticles with blue photoluminescence prepared by hydrosilylation followed by oxidation. *Langmuir* **22**, 4363-4370 (2006).

158. Svrcek, V., Mariotti, D. & Kondo, M. Microplasma-induced surface engineering of silicon nanocrystals in colloidal dispersion. *Appl. Phys. Lett.* **97**, 161502 (2010).

159. Shirahata, N. Colloidal Si nanocrystals: a controlled organic-inorganic interface and its implications of color-tuning and chemical design toward sophisticated architectures. *Phys. Chem. Chem. Phys.* **13**, 7284-7294 (2011).

160. Buriak, J. M. Organometallic chemistry on silicon and germanium surfaces. *Chem. Rev.* **102**, 1271-1308 (2002).

161. Kortshagen, U., Mangolini, L. & Bapat, A. Plasma synthesis of semiconductor nanocrystals for nanoelectronics and luminescence applications. *J. Nanoparticle Res.* **9**, 39-52 (2007).

162. Murray, C. B., Kagan, C. R. & Bawendi, M. G. Synthesis and characterization of monodisperse nanocrystals and close-packed nanocrystal assemblies. *Annu. Rev. Mater. Sci.* **30**, 545-610 (2000).

163. Ligman, R. K., Mangolini, L., Kortshagen, U. R. & Campbell, S. A. Electroluminescence from surface oxidized silicon nanoparticles dispersed within a polymer matrix. *Appl. Phys. Lett.* **90**, 061116 (2007).

164. Mangolini, L., Thimsen, E. & Kortshagen, U. High-Yield Plasma Synthesis of Luminescent Silicon Nanocrystals. *Nano Lett.* **5**, 655-659 (2005).

165. Chin, P. T. K., Hikmet, R. A. M. & Janssen, R. A. J. Energy transfer in hybrid quantum dot light-emitting diodes. *J. Appl. Phys.* **104**, 013108 (2008).

166. Wang, L. W. & Zunger, A. Electronic-Structure Pseudopotential Calculations of Large (Approximate-To-1000 Atoms) Si Quantum Dots. *J. Phys. Chem.* **98**, 2158-2165 (1994).

167. Anikeeva, P. O., Madigan, C. F., Halpert, J. E., Bawendi, M. G. & Bulovic, V. Electronic and excitonic processes in light-emitting devices based on organic materials and colloidal quantum dots. *Phys. Rev. B* **78**, 085434 (2008).

168. Anikeeva, P. O. *et al*. Photoluminescence of CdSe/ZnS core/shell quantum dots enhanced by energy transfer from a phosphorescent donor. *Chem. Phys. Lett.* **424**, 120-125 (2006).

169. Forrest, S. R., Bradley, D. D. C. & Thompson, M. E. Measuring the efficiency of organic light-emitting devices. *Adv. Mater.* **15**, 1043-1048 (2003).

170. Brown, T. M. *et al*. Built-in field electroabsorption spectroscopy of polymer light-emitting diodes incorporating a doped poly(3,4-ethylene dioxythiophene) hole injection layer. *Appl. Phys. Lett.* **75**, 1679-1681 (1999).

171. Parker, I. D. Carrier Tunneling and Device Characteristics in Polymer Light-Emitting-Diodes. *J. Appl. Phys.* **75**, 1656-1666 (1994).

172. Hill, I. G. & Kahn, A. Organic semiconductor heterointerfaces containing bathocuproine. *J. Appl. Phys.* **86**, 4515-4519 (1999).

173. van Buuren, T., Dinh, L. N., Chase, L. L., Siekhaus, W. J. & Terminello, L. J. Changes in the Electronic Properties of Si Nanocrystals as a Function of Particle Size. *Phys. Rev. Lett.* **80**, 3803-3806 (1998).

174. Coe-Sullivan, S., Woo, W., Steckel, J., Bawendi, M. & Bulovic, V. Tuning the performance of hybrid organic/inorganic quantum dot light-emitting devices. *Org. Electron.* **4**, 123-130 (2003).

175. Liu, J., Guo, T. F. & Yang, Y. Effects of thermal annealing on the performance of polymer light emitting diodes. *J. Appl. Phys.* **91**, 1595-1600 (2002).

176. Shi, Y., Liu, J. & Yang, Y. Device performance and polymer morphology in polymer light emitting diodes: The control of thin film morphology and device quantum efficiency. *J. Appl. Phys.* **87**, 4254-4263 (2000).

177. Nanoworld AG, Model: Arrow NCR.

178. Cheng, K., Anthony, R., Kortshagen, U. R. & Holmes, R. J. Hybrid Silicon Nanocrystal-Organic Light-Emitting Devices for Infrared Electroluminescence. *Nano Lett.* **10**, 1154-1157 (2010).

179. Tischler, J. R., Bradley, M. S., Bulovic, V., Song, J. H. & Nurmikko, A. Strong Coupling in a Microcavity LED. *Phys. Rev. Lett.* **95**, 036401 (2005).

180. Photopoulos, P. & Nassiopoulou, A. Room- and low-temperature voltage tunable electroluminescence from a single layer of silicon quantum dots in between two thin SiO2 layers. *Appl. Phys. Lett.* **77**, 1816-1818 (2000).

181. Ioannou-Sougleridis, V., Nassiopoulou, A., Ouisse, T., Bassani, F. & d'Avitaya, F. Electroluminescence from silicon nanocrystals in Si/CaF2 superlattices. *Appl. Phys. Lett.* **79**, 2076-2078 (2001).

182. Kang, J. *et al*. Low roll-off of efficiency at high current density in phosphorescent organic light emitting diodes. *Appl. Phys. Lett.* **90**, 223508 (2007).

183. Kepler, R. G. *et al*. Electron and hole mobility in tris(8-hydroxyquinolinolato-N1,O8) aluminum. *Appl. Phys. Lett.* **66**, 3618-3620 (1995).

184. Matsusue, N., Suzuki, Y. & Naito, H. Charge Carrier Transport in Red Electrophosphorescent Emitting Layer. *Jpn. J. Appl. Phys.* **45**, 5966-5969 (2006).

185. Meyer, J. *et al*. Charge generation layers comprising transition metal-oxide/organic interfaces: Electronic structure and charge generation mechanism. *Appl. Phys. Lett.* **96**, 193302 (2010).

186. Sun, Q. J. *et al*. White light from polymer light-emitting diodes: Utilization of fluorenone defects and exciplex. *Appl. Phys. Lett.* **88**, 163510 (2006).

187. Sasabe, H. *et al*. Wide-Energy-Gap Electron-Transport Materials Containing 3,5-Dipyridylphenyl Moieties for an Ultra High Efficiency Blue Organic Light-Emitting Device. *Chem. Mater.* **20**, 5951-5953 (2008).

188. Hsiao, C., Liu, S., Chen, C. & Lee, J. Emitting layer thickness dependence of color stability in phosphorescent organic light-emitting devices. *Org. Electron.* **11**, 1500-1506 (2010).

189. Mangolini, L., Jurbergs, D., Rogojina, E. & Kortshagen, U. Plasma synthesis and liquid-phase surface passivation of brightly luminescent Si nanocrystals. *J. Lumin* **121**, 327-334 (2006).

190. Kirchmeyer, S. & Reuter, K. Scientific importance, properties and growing applications of poly(3,4-ethylenedioxythiophene). *J. Mater. Chem.* **15**, 2077-2088 (2005).

191. Elschner, A. *et al*. PEDT/PSS for efficient hole-injection in hybrid organic light-emitting diodes. *Synth. Met.* **111**, 139-143 (2000).

192. Kroeger, M. *et al*. Role of the deep-lying electronic states of MoO3 in the enhancement of hole-injection in organic thin films. *Appl. Phys. Lett.* **95**, 123301 (2009).

193. Holmes, J. *et al*. Highly luminescent silicon nanocrystals with discrete optical transitions. *J. Am. Chem. Soc.* **123**, 3743-3748 (2001).

194. Rosso-Vasic, M., Spruijt, E., van Lagen, B., De Cola, L. & Zuilhof, H. Alkyl-Functionalized Oxide-Free Silicon Nanoparticles: Synthesis and Optical Properties. *Small* **4**, 1835-1841 (2008).

195. Yang, C., Bley, R., Kauzlarich, S., Lee, H. & Delgado, G. Synthesis of alkyl-terminated silicon nanoclusters by a solution route. *J. Am. Chem. Soc.* **121**, 5191-5195 (1999).

196. Hua, F. J., Swihart, M. T. & Ruckenstein, E. Efficient surface grafting of luminescent silicon quantum dots by photoinitiated hydrosilylation. *Langmuir* **21**, 6054-6062 (2005).

197. Mangolini, L. & Kortshagen, U. Plasma-assisted synthesis of silicon nanocrystal inks. *Adv. Mater.* **19**, 2513 (2007).

198. Puzzo, D. P. *et al*. Visible Colloidal Nanocrystal Silicon Light-Emitting Diode. *Nano Lett.* **11**, 1585-1590 (2011).

199. Cheng, K., Anthony, R., Kortshagen, U. R. & Holmes, R. J. High-Efficiency Silicon Nanocrystal Light-Emitting Devices. *Nano Lett.* **11**, 1952-1956 (2011).

200. Anthony, R. J., Cheng, K., Holman, Z. C., Holmes, R. J. & Kortshagen, U. R. An All-Gas-Phase Approach for the Fabrication of Silicon Nanocrystal Light-Emitting Devices. *Nano Lett.* **12**, 2822-2825 (2012).

201. Holman, Z. C. & Kortshagen, U. R. A flexible method for depositing dense nanocrystal thin films: impaction of germanium nanocrystals. *Nanotechnology* **21**, 335302 (2010).

202. Marra, D., Edelberg, E., Naone, R. & Aydil, E. Silicon hydride composition of plasma-deposited hydrogenated amorphous and nanocrystalline silicon films and surfaces. *J. Vac. Sci. Technol. A-Vac. Surf. Films* **16**, 3199-3210 (1998).

203. Adachi, C., Baldo, M. A., Thompson, M. E. & Forrest, S. R. Nearly 100% internal phosphorescence efficiency in an organic light-emitting device. *J. Appl. Phys.* **90**, 5048-5051 (2001).

204. Baldo, M. A. *et al*. Highly efficient phosphorescent emission from organic electroluminescent devices. *Nature* **395**, 151-154 (1998).

205. Rothberg, L. & Lovinger, A. Status of and prospects for organic electroluminescence. *J. Mater. Res.* **11**, 3174-3187 (1996).

206. CALCOTT, P., NASH, K., CANHAM, L., KANE, M. & BRUMHEAD, D. Identification of Radiative Transitions in Highly Porous Silicon. *J. Phys. -Condes. Matter* **5**, L91-L98 (1993).

207. Segal, M., Baldo, M. A., Holmes, R. J., Forrest, S. R. & Soos, Z. G. Excitonic singlet-triplet ratios in molecular and polymeric organic materials. *Phys. Rev. B* **68**, 075211 (2003).

208. Segal, M. & Baldo, M. Reverse bias measurements of the photoluminescent efficiency of semiconducting organic thin films. *Org. Electron.* **4**, 191-197 (2003).

209. Garcia, C. *et al*. Size dependence of lifetime and absorption cross section of Si nanocrystals embedded in SiO2. *Appl. Phys. Lett.* **82**, 1595-1597 (2003).

210. Pi, X. D. *et al*. Air-stable full-visible-spectrum emission from silicon nanocrystals synthesized by an all-gas-phase plasma approach. *Nanotechnology* **19**, 245603 (2008).

211. Mastronardi, M. L. *et al*. Size-Dependent Absolute Quantum Yields for Size-Separated Colloidally-Stable Silicon Nanocrystals. *Nano Lett.* **12**, 337-342 (2012).

212. de Boer, W. D. A. M. *et al*. Red spectral shift and enhanced quantum efficiency in phonon-free photoluminescence from silicon nanocrystals. *Nat. Nanotechnol.* **5**, 878-884 (2010).

213. Henry, C. H. & Nassau, K. Lifetimes of Bound Excitons in CdS. *Phys. Rev. B* **1**, 1628-1634 (1970).

214. Baldo, M., Adachi, C. & Forrest, S. Transient analysis of organic electrophosphorescence. II. Transient analysis of triplet-triplet annihilation. *Phys. Rev. B* **62**, 10967-10977 (2000).

215. Ribierre, J. C., Ruseckas, A., Samuel, I. D. W., Staton, S. V. & Burn, P. L. Temperature dependence of the triplet diffusion and quenching rates in films of an Ir(ppy)(3)-cored dendrimer. *Phys. Rev. B* **77**, 085211 (2008).

216. Dhoot, A., Ginger, D., Beljonne, D., Shuai, Z. & Greenham, N. Triplet formation and decay in conjugated polymer devices. *Chem. Phys. Lett.* **360**, 195-201 (2002).

217. Yu, D., Wang, C. & Guyot-Sionnest, P. n-type conducting CdSe nanocrystal solids. *Science* **300**, 1277-1280 (2003).

218. Talapin, D. & Murray, C. PbSe nanocrystal solids for n- and p-channel thin film field-effect transistors. *Science* **310**, 86-89 (2005).

219. Mastronardi, M. L. *et al*. Silicon Nanocrystal OLEDs: Effect of Organic Capping Group on Performance. *Small* **8**, 3647-54 (2012).

220. Mangolini, L., Thimsen, E. & Kortshagen, U. High-Yield Plasma Synthesis of Luminescent Silicon Nanocrystals. *Nano Lett.* **5**, 655-659 (2005).

221. Burr, T., Seraphin, A., Werwa, E. & Kolenbrander, K. Carrier transport in thin films of silicon nanoparticles. *Phys. Rev. B* **56**, 4818-4824 (1997).

222. Nelles, J., Sendor, D., Petrat, F. & Simon, U. Electrical properties of surface functionalized silicon nanoparticles. *J. Nanopart. Res.* **12**, 1367-1375 (2010).

223. Liu, Y. *et al*. Dependence of Carrier Mobility on Nanocrystal Size and Ligand Length in PbSe Nanocrystal Solids. *Nano Lett.* **10**, 1960-1969 (2010).

224. Kang, M. S., Sahu, A., Norris, D. J. & Frisbie, C. D. Size-Dependent Electrical Transport in CdSe Nanocrystal Thin Films. *Nano Lett.* **10**, 3727-3732 (2010).

225. Lepage, H., Kaminski-Cachopo, A., Poncet, A. & le Carval, G. Simulation of Electronic Transport in Silicon Nanocrystal Solids. *J. Phys. Chem. C* **116**, 10873-10880 (2012).

226. Rafiq, M. *et al*. Charge injection and trapping in silicon nanocrystals. *Appl. Phys. Lett.* **87**, 182101 (2005).

227. Rosso-Vasic, M., Spruijt, E., van Lagen, B., De Cola, L. & Zuilhof, H. Alkyl-Functionalized Oxide-Free Silicon Nanoparticles: Synthesis and Optical Properties. *Small* **4**, 1835-1841 (2008).

228. Rogozhina, E., Eckhoff, D., Gratton, E. & Braun, P. Carboxyl functionalization of ultrasmall luminescent silicon nanoparticles through thermal hydrosilylation. *J. Mater. Chem.* **16**, 1421-1430 (2006).

229. Shirahata, N., Hasegawa, T., Sakka, Y. & Tsuruoka, T. Size-Tunable UV-Luminescent Silicon Nanocrystals. *Small* **6**, 915-921 (2010).

230. Tilley, R., Warner, J., Yamamoto, K., Matsui, I. & Fujimori, H. Micro-emulsion synthesis of monodisperse surface stabilized silicon nanocrystals. *Chem. Commun.*, 1833-1835 (2005).

231. Yang, C., Bley, R., Kauzlarich, S., Lee, H. & Delgado, G. Synthesis of alkyl-terminated silicon nanoclusters by a solution route. *J. Am. Chem. Soc.* **121**, 5191-5195 (1999).

232. Shirahata, N., Hirakawa, D. & Sakka, Y. Interfacial-related color tuning of colloidal Si nanocrystals. *Green Chem.* **12**, 2139-2141 (2010).

233. Mansour, N., Momeni, A., Karimzadeh, R. & Amini, M. Blue-green luminescent silicon nanocrystals fabricated by nanosecond pulsed laser ablation in dimethyl sulfoxide. *Opt. Mater. Express* **2**, 740-748 (2012).

234. Gupta, A., Swihart, M. T. & Wiggers, H. Luminescent Colloidal Dispersion of Silicon Quantum Dots from Microwave Plasma Synthesis: Exploring the Photoluminescence Behavior Across the Visible Spectrum. *Adv. Funct. Mater.* **19**, 696-703 (2009).

235. Kusova, K. *et al*. Brightly Luminescent Organically Capped Silicon Nanocrystals Fabricated at Room Temperature and Atmospheric Pressure. *ACS Nano* **4**, 4495-4504 (2010).

236. Hua, F., Swihart, M. & Ruckenstein, E. Efficient surface grafting of luminescent silicon quantum dots by photoinitiated hydrosilylation. *Langmuir* **21**, 6054-6062 (2005).

237. Dickinson, F. M. *et al*. Dispersions of alkyl-capped silicon nanocrystals in aqueous media: photoluminescence and ageing. *Analyst* **133**, 1573-1580 (2008).

238. Hessel, C. M. *et al*. Synthesis of Ligand-Stabilized Silicon Nanocrystals with Size-Dependent Photoluminescence Spanning Visible to Near-Infrared Wavelengths. *Chem. Mat.* **24**, 393-401 (2012).

239. Anthony, R. & Kortshagen, U. Photoluminescence quantum yields of amorphous and crystalline silicon nanoparticles. *Phys. Rev. B* **80**, 115407 (2009).

240. Tessler, N., Medvedev, V., Kazes, M., Kan, S. H. & Banin, U. Efficient Near-Infrared Polymer Nanocrystal Light-Emitting Diodes. *Science* **295**, 1506-1508 (2002).

241. Natter, H., Krajewski, T. & Hempelmann, R. Nanocrystalline palladium by pulsed electrodeposition. *Ber. Bunsen-Ges. Phys. Chem. Chem. Phys.* **100**, 55-64 (1996).

242. Krill, C. & Birringer, R. Estimating grain-size distributions in nanocrystalline materials from X-ray diffraction profile analysis. *Philos. Mag. A-Phys. Condens. Matter Struct. Defect Mech. Prop.* **77**, 621-640 (1998).

243. Borchert, H. *et al*. Determination of nanocrystal sizes: A comparison of TEM, SAXS, and XRD studies of highly monodisperse COPt3 particles. *Langmuir* **21**, 1931-1936 (2005).

Appendix

A.1 X-ray Diffraction Data (XRD) for SiNC thin film reported in

Chapter 6

The NC size is calculated as ~4.4 nm based on the corresponding thin-film XRD data indicated in Figure A.1. The sample is prepared by gas-phase deposition on glass substrate for XRD measurement. The size of the SiNCs was Scherrer broadening estimation, accounting the assumption of spherical shape of NCs.[241-243] The estimation is expressed as Equation A.1

$$d = \frac{4}{3} \frac{(0.9\lambda)}{(\omega\cos(\theta))},$$ (A.1)
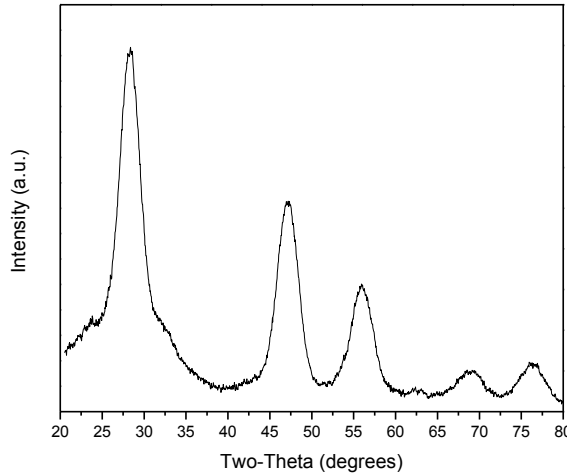
Figure A.1 X-ray diffraction pattern for the SiNC thin film deposited on the glass substrate.

, where d is the grain size (SiNC size); λ is the wavelength of the radiation (0.154 nm for Cu K-alpha x-rays, Bruker-AXS Microdiffractometer with 2.2 kW Sealed Cu-Xray Source); ω is the width on a 2θ angle (full width at half maximum of the strongest (1 1 1) peak in this work); and θ is the angle of considered Bragg reflection.

148

A.2 Derivation in the Reversed Bias Measurement of PL intensities

This derivation is aiming to find the maximum value of $\chi_S\gamma$ by measuring $\eta_C\eta_{PL}$ through experiment parameters, which is indicated in Equation (1.7) :

$$\eta_{EL} = \chi_S\gamma\eta_C\eta_{PL} \qquad (A.2)$$

where χ_S is the spin fraction of singlets; γ is the charge balance factor; η_C is the out-coupling efficiency; and η_{PL} is the photoluminescence efficiency of the emitting materials. The product of $\eta_C\eta_{PL}$ can be determined by the photocurrent under reversed bias, when exciting the luminescent thin film within the OLED devices. The reversed electric field will dissociate the excitons into charges and reduce the intensity of the material PL. As such, the ratio of the change in PL intensity to the collected photocurrent will give $\eta_C\eta_{PL}$. Theoretically, the PL power emitted by the optically excited thin film can be expressed as

$$P_{PL} = \eta_C h\nu \frac{k_R}{k_R + k_{NR} + k_Q}\phi, \qquad (A.3)$$

where h is Plank's constant; ν is the frequency of the radiated photons; k_R is the radiative exciton recombination rate; k_{NR} is the non-radiative decay rate; k_Q is the rate of electric field-induced quenching. For weak field-induced quenching, k_Q is far smaller than k_R+k_{NR}, the decrease in PL power could be expressed as Equation A.4, when the PL efficiency is under no applied-field, (i.e. $\eta_{PL} = k_R/(k_R+k_{NR})$).

$$\Delta P_{PL} = P_{PL}(k_Q) - P_{PL}(k_Q = 0) \approx -h\nu\eta_C\eta_{PL}\frac{k_Q}{k_R + k_{NR}}\phi \qquad (A.4)$$

In addition, the photocurrent from the field-induced dissociation of excitons can be expressed as:

$$I_{ph} = q \frac{k_R}{k_R + k_{NR} + k_Q} \phi \qquad (A.5)$$

where q is the electronic charge. If the condition that k_Q is far smaller than $k_R + k_{NR}$ is valid, then Equation (A.4) and (A.5) could give

$$\eta_C \eta_{PL} = -\frac{q}{h\nu} \frac{\Delta P_{PL}}{I_{ph}} \phi \qquad (A.6)$$

From the definition of external quantum efficiency, the η_{PL} can be obtained as

$$\eta_{PL} = \frac{1}{q I_{inj} h\nu \eta_{EL}} \qquad (A.7)$$

where I_{inj} is the current injected into device (device current). Therefore, by using (A.2), the product of spin statistic factor and charge balance factor can be written as

$$\chi_S \gamma = \frac{\eta_{EL}}{\eta_C \eta_{PL}} = \frac{\dfrac{P_{EL}}{I_{inj}}}{\dfrac{-\Delta P_{PL}}{I_{ph}}} \qquad (A.8)$$

Therefore, the spin statistics can be obtained from η_{EL} and the ratio of differential PL power to photocurrent I_{ph}.

A.3 Single Layer SiNC-LED

A.3.1 Device Fabrication of Single layer SiNC-LEDs

This solution processed single-layer device is aimed to reduce the fabrication steps in order to simplify the device structure and to understand the behavior of the SiNCs under

the electrical excitation without any influence by organic semiconductors. In this case, the true performance of SiNCs could be studied by isolating the SiNC from the other materials, allowing explorations of efficiency and charge-transport comparison between different type of SiNCs or among different design of device structures.

The single layer SiNC-LEDs were fabricated on indium-tin-oxide (ITO) coated glass substrates with a sheet resistance of 15 $\Omega/\square$. Substrates were degreased with solvents, followed by exposure to UV-ozone ambient. The SiNC layer was spin-coated by exploiting the 20 mg/mL SiNC in chloroform. (2000 rpm for 90sec), followed by thermal annealing at 150°C for 1 hour in nitrogen environment. (Oxygen <0.1 ppm, and Moisure < 0.1ppm) The thickness of SiNC layer is ~ 100 nm for SiNCs, confirmed by AFM. Finally, the SiNC layer was capped by 0.5 nm LiF/ 50 nm Al as device cathode. Devices were immediately tested in the ambient environment after the fabrication.

A.3.2 Device Characterization of Single-layer SiNC-LEDs

The single-layer SiNC-LED demonstrates the EL from the SiNC, as shown in Figure A.2 (a). The similar peak EL blue shift is also observed as the applied current density increased. However, the EL intensity under higher current starts to decay, which could be due to the charge imbalance or the decay of the thin device under high electrical field. Surprisingly, the preliminary data show that the peak efficiency can be achieved as 2.3% at 0.03 mA/cm^2. (Figure A.2 (b)) Such un-optimized device structure could be obtained as > 2% in device efficiency, even without the assistance of the organic charge blocking layers. This could, again, suggests the robust luminescence property of SiNCs. The

corresponding turn-on voltage is ~ 2.9 V as shown in Figure A.2 (c), which could originate from the higher resistance of thicker layer of SiNCs. Therefore, further device optimization with higher device efficiency and low turn-on voltage could be achieved by reducing the SiNC thickness.
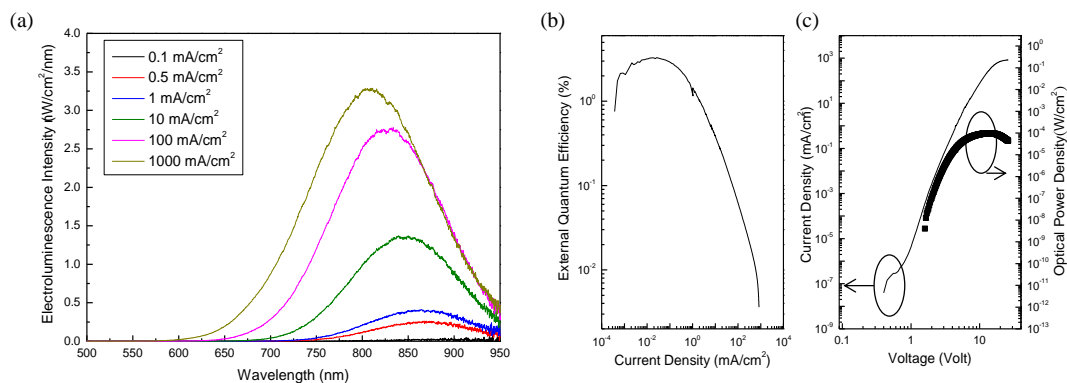
Figure A.2 Device Characteristics for single-layer SiNC-LED (a) Electroluminescence as a function of applied current density; (b) current density and (c) power density as a function of voltage.

A.4 Ligand Length Dependence of Device Performance

The devices with different ligand length were fabricated with the same conditions as the ones addressed in Chapter 4, where the concentration of SiNC solution (20 mg/mL), spin coating speed, and annealing time were maintained the same. The preliminary results of the devices for the ligand length dependence were summarized in Figure A.3, in which the efficiency performance was generally lower. Note that the performance of the devices made with SiNCs containing 1-hexene or 1-octadacene ligands were not fully optimized in terms of photoluminescence efficiency (in 1-hexene case) and thickness (in 1-octadecene case). More device studies are required in order to achieve thorough study with higher device efficiencies.
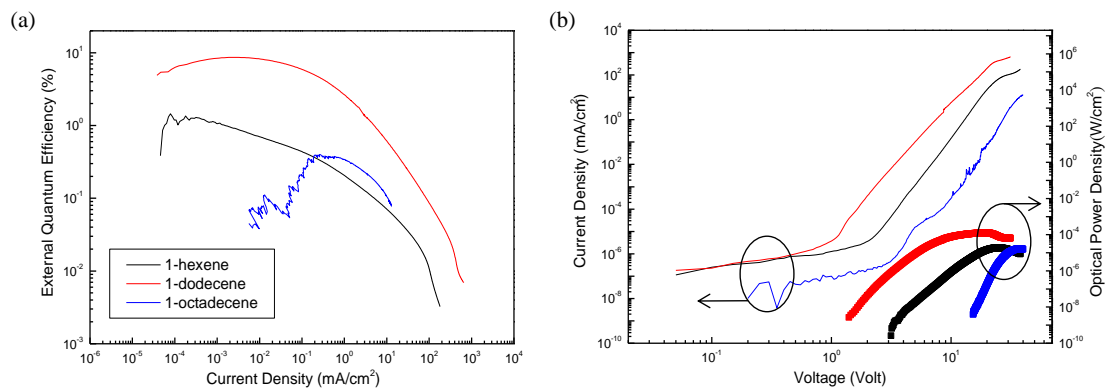
Figure A.3 Summary of Device Performance containing different ligand length. (a) External quantum efficiency of the devices containing 1-hexene (black), 1-dodecene (red), and 1-octadecene (blue); (b) Current-density and (c) power density of the corresponding devices in (a).

A.5 Copyright Permission

Chapter 2

Figure 2.1 (a)

Title: Synthesis and characterization of nearly monodisperse CdE (E = sulfur, selenium, tellurium) semiconductor nanocrystallites

Author: C. B. Murray, D. J. Norris, and M. G. Bawendi

Publication: Journal of the American Chemical Society

Publisher: American Chemical Society

Date: Sep 1, 1993

Copyright © 1993, American Chemical Society

PERMISSION/LICENSE IS GRANTED FOR YOUR ORDER AT NO CHARGE

This type of permission/license, instead of the standard Terms & Conditions, is sent to you because no fee is being charged for your order. Please note the following:

Permission is granted for your request in both print and electronic formats, and translations. If figures and/or tables were requested, they may be adapted or used in part.

Please print this page for your records and send a copy of it to your publisher/graduate school.

Appropriate credit for the requested material should be given as follows: "Reprinted (adapted) with permission from (COMPLETE REFERENCE CITATION). Copyright (YEAR) American Chemical Society."Insert appropriate information in place of the capitalized words.

One-time permission is granted only for the use specified in your request. No additional uses are granted (such as derivative works or other editions). For any other uses, please submit a new request.

If credit is given to another source for the material you requested, permission must be obtained from that source.

Copyright © 2012 Copyright Clearance Center, Inc. All Rights Reserved. Privacy statement.

Chapter 2

Figure 2.1 (b)

Title: CdSe/ZnS Core−Shell Quantum Dots: Synthesis and Characterization of a Size Series of Highly Luminescent Nanocrystallites

Author: B. O. Dabbousi et al.

Publication: The Journal of Physical Chemistry B

Publisher: American Chemical Society

Date: Nov 1, 1997

Copyright © 1997, American Chemical Society

Chapter 2

Figure 2.4 (a)

AMERICAN INSTITUTE OF PHYSICS LICENSE TERMS AND CONDITIONS

Nov 04, 2012

All payments must be made in full to CCC. For payment instructions, please see information listed at the bottom of this form.

License Number: 3022021313767
Order Date: Nov 04, 2012
Publisher: American Institute of Physics
Publication: Journal of Chemical Physics

Article Title: Electron–electron and electron-hole interactions in small semiconductor crystallites: The size

dependence of the lowest excited electronic state
Author: L. E. Brus
Online Publication Date: May 1, 1984
Volume number: 80
Issue number: 9
Type of Use: Thesis/Dissertation
Requestor type: Student
Format: Print and electronic
Portion: Figure/Table
Number of figures/tables: 1
Title of your thesis/dissertation: Realizing Efficient Electroluminescence from Silicon Nanocrystals
Expected completion date: Sept. 2013
Estimated size (number of pages): 180
Total: 0.00 USD

4. The foregoing license shall not take effect unless and until AIP or its agent, Copyright Clearance Center, receives the Payment in accordance with Copyright Clearance Center Billing and Payment Terms and Conditions, which are incorporated herein by reference.

5. AIP or the Copyright Clearance Center may, within two business days of granting this license, revoke the license for any reason whatsoever, with a full refund payable to you. Should you violate the terms of this license at any time, AIP, American Institute of Physics, or Copyright Clearance Center may revoke the license with no refund to you. Notice of such revocation will be made using the contact information provided by you. Failure to receive such notice will not nullify the revocation.

6. AIP makes no representations or warranties with respect to the Material. You agree to indemnify and hold harmless AIP, American Institute of Physics, and their officers, directors, employees or agents from and against any and all claims arising out of your use of the Material other than as specifically authorized herein.

7. The permission granted herein is personal to you and is not transferable or assignable without the prior written permission of AIP. This license may not be amended except in a writing signed by the party to be charged.

8. If purchase orders, acknowledgments or check endorsements are issued on any forms containing terms and conditions which are inconsistent with these provisions, such inconsistent terms and conditions shall be of no force and effect.

This document, including the CCC Billing and Payment Terms and Conditions, shall be the entire agreement between the parties relating to the subject matter hereof.
This Agreement shall be governed by and construed in accordance with the laws of the State of New York. Both parties hereby submit to the jurisdiction of the courts of New York County for purposes of resolving any disputes that may arise hereunder.

If you would like to pay for this license now, please remit this license along with your payment made payable to "COPYRIGHT CLEARANCE CENTER" otherwise you will be invoiced within 48 hours of the license date. Payment should be in the form of a check or money order referencing your account number and this invoice number RLNK500890134. Once you receive your invoice for this order, you may pay your invoice by credit card. Please follow instructions provided at that time.
Make Payment To: Copyright Clearance Center Dept 001 P.O. Box 843006 Boston, MA 02284-3006
For suggestions or comments regarding this order, contact RightsLink Customer Support: customercare@copyright.com or +1-877-622-5543 (toll free in the US) or +1-978-646-2777.
Gratis licenses (referencing $0 in the Total field) are free. Please retain this printable license for your reference. No payment is required.

Editor of portion(s): N/A

Author of portion(s): Bawendi, M. G., Steigerwald, M. L. & Brus, L. E

Volume of serial or monograph: 41

Issue, if republishing an article from a serial: N/A

Page range of portion: 485

Publication date of portion: 1990

Note: This item was invoiced separately through our RightsLink service. $ 0.00

Rights: Main product

Chapter 3

Title: Hybrid Silicon Nanocrystal−Organic Light-Emitting Devices for Infrared Electroluminescence

Author: Kai-Yuan Cheng, Rebecca Anthony, Uwe R. Kortshagen, and Russell J. Holmes

Publication: Nano Letters

Publisher: American Chemical Society

Date: Apr 1, 2010

Logged in as: Kai-Yuan Cheng

Chapter 4

Title: High-Efficiency Silicon Nanocrystal Light-Emitting Devices

Author: Kai-Yuan Cheng, Rebecca Anthony, Uwe R. Kortshagen, and Russell J. Holmes

Publication: Nano Letters

Publisher: American Chemical Society

Date: May 1, 2011

Chapter 6

Ttile: An All-Gas-Phase Approach for the Fabrication of Silicon Nanocrystal Light-Emitting Devices

Author: Rebecca J. Anthony, Kai-Yuan Cheng, Zachary C. Holman, Russell J. Holmes, and Uwe R. Kortshagen

Publication: Nano Letters

Publisher: American Chemical Society

Date: Jun 1, 2012

Copyright © 2012, American Chemical Society

PERMISSION/LICENSE IS GRANTED FOR YOUR ORDER AT NO CHARGE